Optimal Design of Auxetic Core Airfoil for Wing Morphing Applications

A thesis submitted in partial fulfillment of the requirements
for the award of the degree of

Master of Engineering

in

Thermal Engineering

by

Amanpreet Singh Whan

Roll No.: 802283001

Under the Supervision of

Dr. Rajnish Mallick

Dr. Rajesh Kumar Shukla

Department of Mechanical Engineering

Thapar Institute of Engineering & Technology, Patiala-147004, India

(Deemed to be University)

August, 2024

Certificate

This is to certify that the dissertation entitled **"Optimal Design of Auxetic Core Airfoil for Wing Morphing Applications"**, submitted by **Amanpreet Singh Whan** to the Thapar Institute of Engineering & Technology, for the award of the degree of ME Thermal Engineering, represents original and bonafide research work carried out by him under our mentorship. The dissertation meets the standards and fulfills the requirements as stipulated by the regulations governing the award of the degree.

To the best of our knowledge, the research findings presented in this dissertation have not been previously submitted, either in whole or in part, to any other university or institute for the award of any degree or diploma.

.....

Dr. Rajnish Mallick
Assistant Professor,
Department of Mechanical Engineering,
TIET.

.....

Dr. Rajesh Kumar Shukla
Assistant Professor,
Department of Mechanical Engineering,

Declaration

I hereby declare that this dissertation is a product of my own work and reflects my original ideas. Where I have incorporated the ideas and words of others, I have duly cited and referenced the original sources. I affirm that I have adhered to the principles of academic honesty and integrity, and have not misrepresented, fabricated, or falsified any ideas, data, facts, or sources in this submission. I understand that any breach of the above may result in disciplinary action by the Institute and could also lead to legal consequences if proper citation or permission has not been obtained where required.

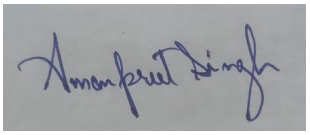

.....

Amanpreet Singh Whan
Roll No.: 802283001
Dept.: Mechanical Engineering Department
TIET, Patiala

Abstract

Bird wings demonstrate phenomenal adaptation and aerodynamic performance across varied flight conditions. In contrast, conventional aircraft wings are designed for specific scenarios, limiting their adaptability. Therefore, the integration of smart structures into morphing airfoils is crucial for furthering aircraft development. One intriguing approach is the utilization of cellular auxetic configurations, which exhibit an inverse (negative) Poisson's ratio, popularly recognized as auxetic behavior. This particular trait can bring substantial advantages to the morphing process. Morphing airfoils containing a cellular auxetic core offer various benefits, including greater deformability, ease of control, variable stiffness, and improved stress tolerance. This research provides a novel approach by discovering the optimal reentrant unit cell and extending its key advantage within the aerospace sector, focusing on achieving maximal wing trailing edge deflection. This research compares the morphing performance of the Eppler 420 airfoil incorporating different cellular auxetic cores, including hexagonal honeycomb, chiral honeycomb, and reentrant honeycomb configurations. A parametric investigation explores the in-plane characteristics of a 2D reentrant honeycomb configuration and evaluates the consequences of parameter changes on the structure's negative Poisson ratio and elastic modulus. Through multi-objective optimization employing a genetic algorithm, the study achieves a remarkable 54.65% enhancement in Poisson's ratio and a substantial 37.5% rise in the relative elastic modulus, as evaluated analytically. The Finite Element Analysis (FEA) of the Eppler 420 airfoil revealed that integration of the reentrant honeycomb configuration outperforms the other two configurations to achieve maximum trailing edge deflection or morphing. Furthermore, the incorporation of optimized reentrant configuration within the airfoil core leads to a significant augmentation of 21 % in trailing edge deflection compared to standard reentrant configuration. decoupled fluid structural analysis of the Eppler 420 airfoil showed that maximum morphing occurs at an 8° angle of attack with Mach 0.25 and a 6° angle with Mach 0.45. The optimized reentrant honeycomb configuration improved trailing edge deflection by 17.3% compared to the standard reentrant honeycomb core. This research emphasizes the potential of adopting optimized reentrant structures to boost the performance and adaptability of aircraft wings.

Acknowledgement

I sincerely express my profound gratitude to my supervisor, Dr. Rajnish Mallick, for his unwavering support, encouragement, and guidance throughout this project. I would also like to express my deep appreciation to my co-supervisor, Professor Dr. Rajesh Kumar Shukla, for his continuous support and invaluable input over the past few months, which enabled me to complete this research on time. My heartfelt thanks go to Professor Dr. J.S. Saini for his continuous support and guidance during my master's studies.

Lastly, I am immensely grateful to my parents for their support and motivation, which played a crucial role in driving me to excel throughout this project and my academic journey.

Publications

1. Whan, A.S., Singh, H., Malik, N., Mallick, R., Sharma, A., & Sahni, M., "Optimizing the Design of Auxetic Core Airfoil for Wing Morphing Applications". 4th International Conference on Mathematical Modeling, Computational Intelligence Techniques and Renewable Energy, 29-31 May 2024, Jaipur, India

2. Whan, A.S., Singh, H., Malik, N., Balayan, A., Dwivedi, S., Mallick, R., Sharma, A., & Sahni, M., "Optimizing the Design of Auxetic Core Airfoil for Wing Morphing Applications, Structural Integrity and Life (SIL) Journal." (under review)

3. Design Optimization of Auxetic Core Airfoils for Wing Morphing Applications: An FEA and CFD Study (in preparation stage).

4. CFD Analysis of Optimal Design of Auxetic Airfoil Core for Wing Morphing Applications (in preparation stage).

Contents

List of Figures

List of Tables

Abbreviations

CFD	Computational Fluid Dynamics
FEA	Finite Element Analysis
CAD	Computer-Aided Design
SMA	Shape Memory Alloys
ACTE	Adaptive Compliant Trailing Edge
CFRP	Carbon Fiber Reinforced Polymer
STOL	Short Take-off and Landing
RANS	Reynolds-Averaged Navier–Stokes Equations
PLA	Polylactic Acid
FBD	Free Body Diagram
AoA	Angle of Attack
MDOF	Multi-Degree of Freedom
LUSM	Linear Ultrasonic Motor
FishBAC	Fish Bone Active Camber
AM	Additive Manufacturing
NPR	Negative Poisson's Ratio
UAV	Unmanned Aerial Vehicle
MOGA	Multi- Objective Genetic Algorithm

Symbols

Q_i	External Forces
q_i	Degree of Freedom
k_{ij}	Elements of Stiffness Matrix
F	Force applied
W	Horizontal dimension of a unit cell
H	Vertical dimension of a unit cell
θ	Angle between vertical and horizontal struts
l	Dimension of inclined strut
A	Area of a unit cell
E_s	Material Young's Modulus
σ_{yt}	Yield Strength of material
σ_{ut}	Ultimate Strength of material
I	Moment of Inertia
σ_x	Stress in x-axis
σ_y	Stress in y-axis
ν_{xy}	Poisson' ratio in xy-plane
ν_{yx}	Poisson' ratio in yx-plane
ρ	Density of fluid
u, v, w	velocity components

P	Pressure
μ	Dynamic viscosity
T	Temperature
τ_{ij}	Stress Tensor
G_k	Turbulence kinetic energy generation
G_w	Turbulence kinetic energy generation of ω
Γ_k	Effective diffusivity of k
Γ_ω	Effective diffusivity of ω
Y_k	Turbulence-induced dissipation k
Y_ω	Turbulence-induced dissipation ω
S_k, S_ω	User-defined source terms
C_d	Drag Coefficient
C_l	Lift Coefficient

Chapter 1

Introduction

1.1 Background

The core purpose of any engineering domain is to improve the present system's efficacy or build innovative ones with superior efficacies. In the field of aerospace engineering, this pertains to optimizing the thermodynamic, aerodynamic, and structural layout of aircraft. Conventional aircrafts use discrete flight control surfaces such as elevators, rudders and ailerons for managing and controlling flight dynamics. Consequently, these discrete control surfaces generate spanwise gaps, discontinuities, and sharp corners. This leads to several limitations for aircraft operating in complex environments and compromised performance under suboptimal conditions, such as changes in loads, flight attitudes, or mission objectives.[1, 2].

Aviators have consistently drawn their inspiration from flying creatures such as birds to address flight control and aerodynamic challenges [3, 4, 5]. Figure 1.1 demonstrates how the shape of a bird's wings and tail adjust when transitioning from high-speed cruising to rapid maneuvers and subsequently to stable landings, enabling the efficient and effective performance of various flight tasks [6]. Inspired by this behavior, the "morphing

aircraft" concept was proposed as a meaningful alternative to performing multiple tasks during a single flight while maintaining optimal performance. This approach has garnered significant research attention and has emerged as a central development area in future aircraft design.

FIGURE 1.1: Bird demonstrating different flight postures during (a) cruising, (b) diving, and (c) landing [6].

The term "Morphing" refers to the continuous alteration of a shape, wherein different components maintain stationary positions relative to each other and deform collectively upon actuation. From Figure 1.2, in the case of aircraft wings, this means replacing complex assembly consisting of ailerons, flaps, slats, and spoilers with a monolithic structure capable of modulating its surface area and assembly seamlessly, disregarding the opening of gaps within itself and the main wing. The abrupt changes in the wing's shape get minimized, resulting in a significant decrease in aerodynamic losses, vibration, and noisy operation in the aircraft's structure [7].

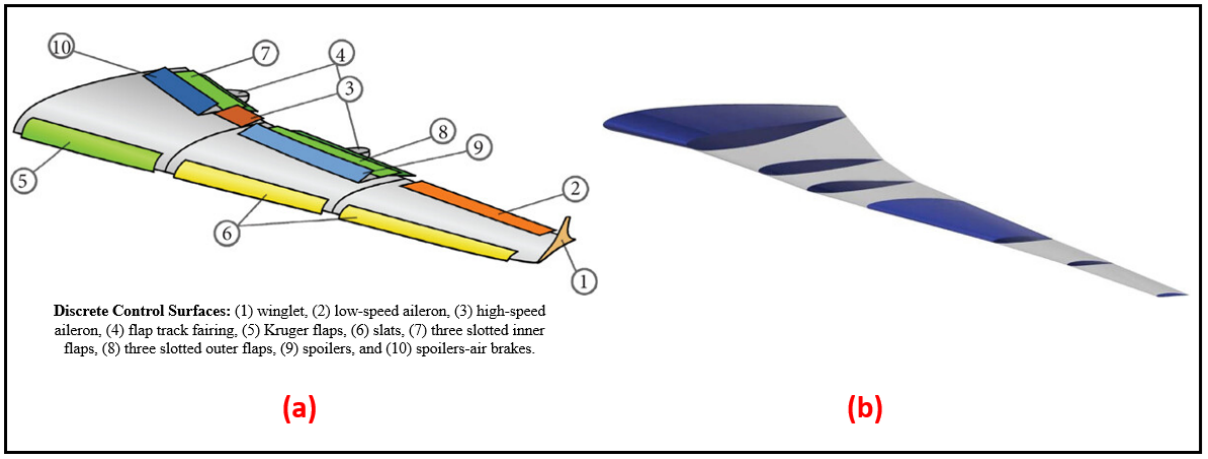

FIGURE 1.2: (a) A conventional wing designed with separate control mechanisms [7] (b) a morphing wing featuring adaptable and bendable ribs [8].

The morphing aircraft structure represents a morphing aircraft as a versatile platform designed to adjust its shape in response to environmental variations, enabling it to perform multiple roles [8]. As it is known that the majority of lift comes from aircraft wings, altering wing parameters, including size, span, and airfoil shape, can majorly impact the aircraft's performance. Consequently, designers and researchers primarily concentrate on the wings, with limited attention to designs incorporating morphing tails or fuselages [9].

1.2 Motivation

To address the ever growing demands for cleaner, robust, efficient, and affordable aircraft designs, it is proposed that conventional aircraft design approaches must be reconsidered in favor of innovative "morphing" technologies and methods. Morphing generally focuses on adaptive geometry structures and mechanisms to enhance aircraft performance. Nonetheless, the morphing designs that have emerged over the last few decades still face structural problems.[9].

In aerospace applications, particularly in wing morphing, a crucial requirement is its ability to undergo shape alterations in at least one of two ways: shifts in camber (for

instance, ailerons, slats, flaps, or winglets on aircraft wings) and modifications in surface area (for example, flaps and slats on aircraft wings) [10]. Generally, morphing wings must necessitate a flexible structure capable of producing controlled, compliant deformations while maintaining sufficient stiffness to withstand aerodynamic loads [11]. Integrating smart structures and adaptable technology into aircraft has opened up significant opportunities for adopting innovative concepts for structural morphing [12]. Smart structures use external actuators, integrated actuators, or inherent self-actuating properties to facilitate shape changes. These characteristics allow them to detect different external stimuli (such as changes in velocity, pressure, etc.), process information, and deliver a regulated real time response (ibid).

Cellular structures are identified for their enhanced mechanical properties and multifunctional capabilities, making them suitable for superior structural component designs. The topology controls the auxetic features, implying that these traits are governed by the geometry and shape of the particular cell that forms the structure. The geometry, shape, and associated features can be modified to fulfill specific application requirements or to obtain various functionality [13]. In prior literature, the potential advantages of chiral lattice structures in the context of passive wing morphing have been recognized; however, direct comparisons with other cellular structures to determine their relative effectiveness have yet to be conducted. To address the research gaps, this thesis investigates the morphing performance of various cellular structures by comparing their ability to achieve maximum trailing edge deflection.

1.3 Aims and Objectives

The primary motivation for this study was to explore different cellular structures and understand their impact on the morphing performance of a wing. The project aims to design and develop a novel cellular configuration with optimized negative Poisson's ratio

and elastic modulus to achieve maximum trailing edge deflection. The aims of the project will be achieved by fulfilling the following objectives:

- Conduct a literature review to understand the methodologies for passive morphing wing application using cellular auxetic metamaterials and identify any potential gaps in knowledge or research.
- Conduct a detailed examination of the in-plane mechanical properties, including Poisson's ratio and elastic moduli for reentrant honeycomb configuration.
- Study how different parameters affect these properties, and identify the optimal parameters combination to design a novel structure with an optimal elastic modulus and a negative Poisson's ratio.
- Carry out a steady-state structural analysis using Ansys Mechanical software under aerostatic loading on a 3D airfoil incorporating different cellular (auxetic) structures to identify the configuration that exhibits the maximum trailing edge deflection.
- Perform 2D Computational Fluid Dynamics (CFD) simulations using Ansys Fluent to validate and assess the impact on aerodynamic coefficients at various AoA for NACA 0012 and NACA 2412 airfoils across different Reynolds numbers.
- Extend and apply the same physics to perform a decoupled fluid structural analysis of the Eppler 420 airfoil integrating cellular core to determine aerodynamic coefficients and maximum trailing edge deflection at different Reynolds numbers.

1.4 Thesis Organization

The thesis comprises a total of five chapters, with the present Chapter 1 introducing the research topic. This chapter also clarifies the background, motivation, aims, and objectives of this research and provides a brief thesis outline.

Following this introduction, Chapter 2 presents a detailed literature review that focuses on previous research related to morphing aircraft concepts, with a particular emphasis on camber-based morphing airfoils. This chapter also delves into the exploration of different cellular structures and their applications in airfoil morphing as studied by researchers in the past.

Chapter 3 presents the fundamental theoretical principles of CFD, turbulence modeling, and the practical application of the N-S equations to boundary layer theory. For methodology, the chapter also lays out an overview of the construction of CAD designs, meshing to setting boundary constraints to perform simulations utilizing commercial software such as Ansys Fluent.

Chapter 4 presents and discusses the static structural and CFD results of airfoils integrating cellular cores. This chapter also includes a parametric analysis and optimization of the auxetic unit cell that will be incorporated into the airfoil to determine trailing edge deflection.

Chapter 5 details the main findings and contributions to the field and provides recommendations for future work based on the study's results.

Chapter 2

Literature Review

2.1 Introduction

With advancement in smart materials, sensors, and actuators, there has been a significant surge of interest among aviators and researchers in morphing air vehicles. Although the field is relatively new, the concept of morphing applications has been around for several years. Sections 2.2, 2.3 and 2.4 of this chapter begin by presenting historical accomplishments in the field of wing morphing, followed by recent advancements in camber-change morphing utilizing cellular structures or auxetic metamaterials. Sections 2.5 and 2.6 provide an overview of various cellular structures and identify potential research gaps in the literature.

2.2 Morphing Aircraft History

The evolution of aircraft morphing based on wing deformation forms can be categorized into three parts. First, the concept of adjustable structures originates from the Wright Flyer, the pioneering airplane designed by the Wright Brothers. The designed aircraft

featured flexible wings, allowing the wings to perform bird-like twisting, as shown in Figure 2.1 [14]. Despite issues with carrying capacity and stability due to its wooden structure, this led to the creation of all-metal aircraft, which improved cruising speeds and payload capacities [15]. Over time, flexible structures capable of morphing and adapting evolved, leading to the development of hybrid wing designs incorporating rigid control mechanisms such as flaps, ailerons, and slats. These elements have become commonplace in contemporary fixed-wing aircraft designs. [16]. To summarise, the initial section covers the beginning of morphing aircraft, highlighting early models incorporating slight wing shape modifications.

FIGURE 2.1: Photograph of the designed aircraft by Wright Flyer from 1903 [14].

Second, the variable-configuration structure construction began in the 1930s [17]. Researchers worked on creating wide-ranging morphing aircraft capable of altering their wing configuration mid-flight, improving their versatility for various missions [18]. Conventional wings have limited overall performance due to their compromised design, as slow-cruising air vehicles require high aspect-ratio wings for efficiency, while

high-speed, especially supersonic, aircraft need low aspect-ratio wings with high sweep angles for stability and maneuverability [19, 20]. As a result, new techniques have been proposed to significantly alter aerodynamics, which are classified based on morphing degrees of freedom: planform, airfoil, and out-of-plane morphing. Table 2.1 highlights the advantages of these different morphing degrees of freedom [21]. These inflexible and mechanical mechanisms for morphing have also been used in the construction of fuselages, engines, and air intakes [22, 23].

TABLE 2.1: Types and Advantages of Wing Morphing [6].

Types	**Methods**	**Advantages**	**Examples**
Planform	Sweep	Increased critical Mach number; decreased high-speed drag	F-14, F-111, Mig-23, Su-24, B-1A
	Span	Increased L/D, cruise time, and distance; decreased engine requirements	MAK-10, MAK-123, FS-20
	Chord	Increased low-speed performance	LIG-7
Airfoil	Camber	Increased range and wing efficiency	AFTI/F-111, Gulfstream III
	Thickness	Increased low-speed/high-speed performance	Adaptive laminar wing
Out-of-plane	Twist	Increased range and wing efficiency	AFTI/F-111, Gulfstream III
	Dihedral	Increased lateral stability and rolling capacity; increased maximum speed	XB-70, F/A-18, Gull-wing morphing aircraft
	Spanwise Bending	Increased lateral-directional stability; decreased wing-root bending	Morphing hyper-elliptic cambered span wing

The last aspect pertains to the designing of smart adaptive structures that emerged with the appearance of advanced materials in the 1980s [24].These advanced (smart) materials are characterized by their ability to adapt, sense, and repair themselves when exposed to different external conditions [25]. A variety of these materials, including

shape memory alloys (SMAs), piezoelectric substances, and magnetostrictive components, have been employed in the development of morphing aircraft by aviation engineers [26, 27]. These smart structures have led research into lightweight, flexible, intelligent, and optimally designed aircraft. Such structures contribute to improved lift and reduced drag, thereby lowering fuel consumption, noise levels, and emissions [28]. The development of these advanced structures and materials can be further enhanced by utilizing techniques in topology optimization, additive manufacturing (AM), and composite materials [29]. Even though the three stages of aircraft morphing were initiated at different times, no single approach has been discontinued and deemed superior. However, flexible morphing conceptual designs gained popularity, as evidenced in Figure 2.2, proposed by leading research institutions [30, 31, 32].

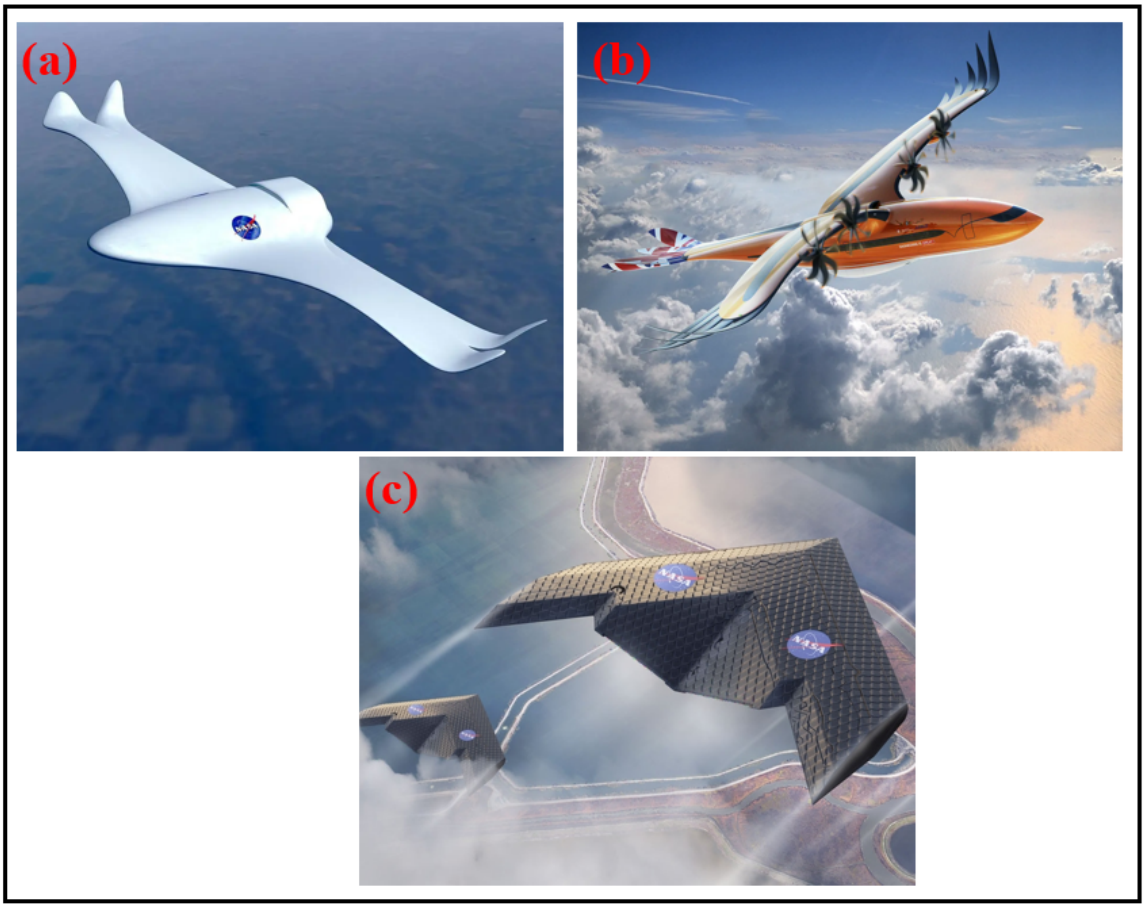

FIGURE 2.2: Conceptual Advances in Next-Generation Aviation: (a) NASA's aerospace vision for the 21st century [30], (b) Airbus's cutting-edge conceptual aircraft design [31], and (c) innovative airplane wing technology from MIT and NASA [32].

While morphing aircraft design offers significant benefits, they also encounter significant challenges arising from both operational conditions and increasing demands for cost-effectiveness and performance. Therefore, this field inherently requires advanced multidisciplinary research encompassing material mechanics, aero-structural engineering, aerodynamics, control systems, and optimization techniques [33].

2.3 Conventional Aircraft Morphing

Conventional aircraft mechanically change or morph their configuration during flight, a mechanism primarily developed during and after World War II for fighter aircraft as a result of the arms race [2]. The variable span wings are the simplest form of morphing wings, which integrates the benefits of both the low and high-aspect ratio wings, enhancing performance and multitasking adaptability across different environmental conditions [34, 35]. Tarabi *et al.* prepared a span-wise morphing wing featuring a movable fixed-wing segment. Wind tunnel experiments revealed drag reduction and enhanced aerodynamic performance, resulting in a increment of 5% in flight operating distance and a 17% boost in endurance [36]. However, the development of manned spanwise-morphing aircraft has been limited due to the bulky mechanisms involved and the persistent challenge of maintaining a flexible skin seal [37].

The swept angles of a wing significantly influence the lift and aerodynamic performance. Wings that feature considerable swept-back angles excel in lift and lower drag at elevated velocities, particularly at supersonic flows, due to their ability to withstand shock waves better. On the other hand, wings with minimal swept-back angles perform better in generating lift at lower velocities. [40]. During and post-World War II, numerous fighter aircraft designs featuring variable-sweep wings were introduced that enhanced performance across a broad range of speeds, from high-speed cruising and supersonic maneuvers to low-speed takeoffs and landings. The F-111 and F-14 stand out

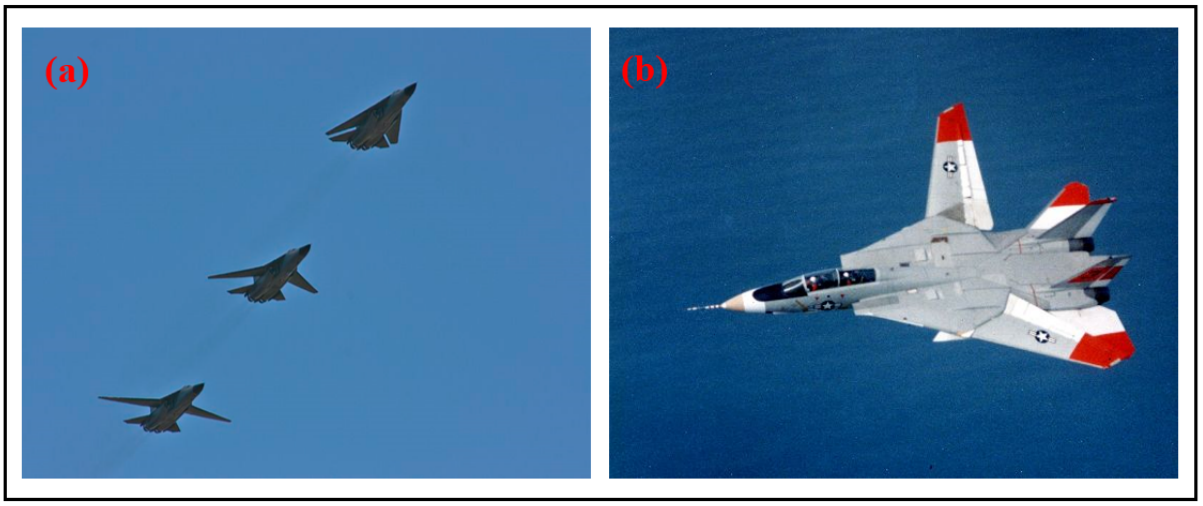

FIGURE 2.3: Morphing of aircraft utilizing sweeping procedure: (a) Symmetrical sweeping sequence of the F-111 aircraft [38] and (b) Asymmetrical Sweeping of the F-14 aircraft [39].

as the two most renowned examples of aircraft utilizing this technology, as shown in Figure 2.3 [38, 39]. At present, the use of variable-sweep technology represents the most accomplished application of morphing technology in manned aircraft. Nonetheless, early variable-sweep technologies were eventually phased out due to drawbacks such as complex mechanisms (Figure 2.4), poor reliability, and excessive weight [41, 42]. Over time, they have gradually been substituted by designs such as canard wings, double-delta wings, strake wings, and blended wing-body configurations [43].

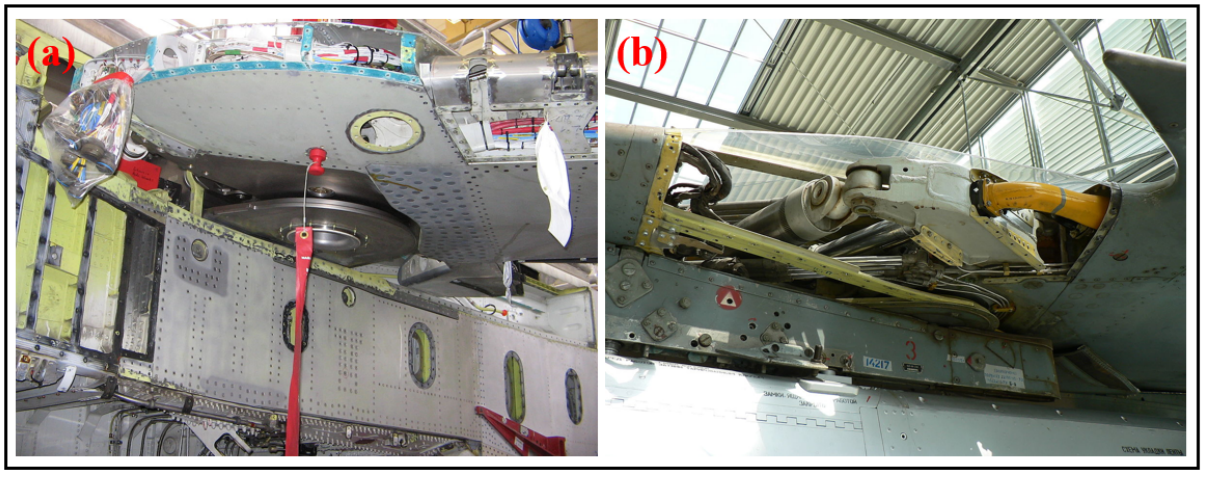

FIGURE 2.4: Complex operations of Swept Wings: (a) Panavia Tornado [41] and (b) MiG-23 [42]

Folding wing sections, otherwise known as dihedral morphing wings, enhance lift and stability during flight. The XB-70 supersonic bomber, also known as the Valkyrie, is a typical example. It achieved flight velocities of Mach 3 in high-temperature conditions during the late 1950s and early 1960s. During its flights, the outer panels of the XB-70's wings would fold down by nearly 30 degrees, as illustrated in Figure 2.5(a) [44]. However, winglet bending technologies used in aircraft are mostly ground-based and are designed to fulfill size specifications while minimizing the space needed for transport. Other morphing aircraft integrate fuselage and engine morphing technologies. The Concorde supersonic airliner, as shown 2.5(b), features a droop-able nose to reduce drag and improve supersonic flight performance (up to Mach 2). The long-pointed nose extends forward in front of the cockpit but obstructs the pilot's visibility because it sits at a steep angle during the takeoff and landing stages [9].

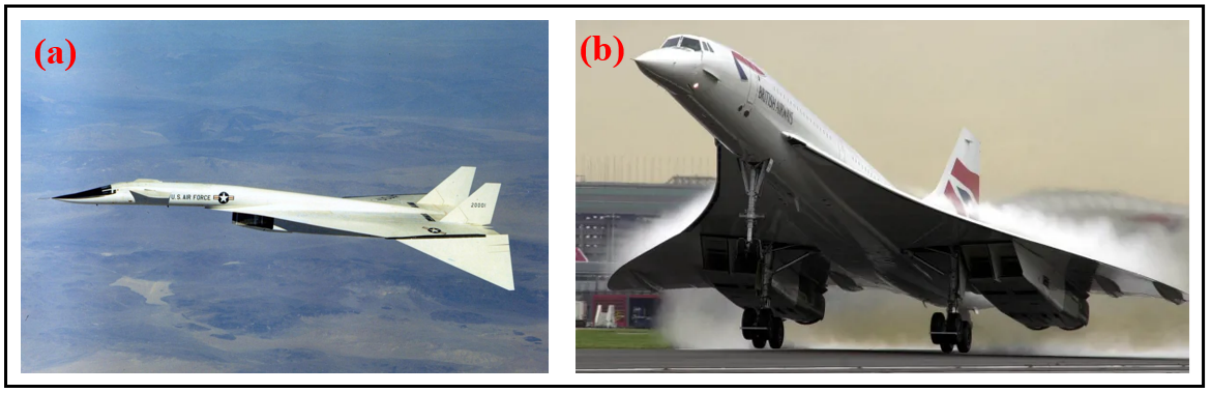

FIGURE 2.5: Other aircraft morphing mechanisms: (a) dihedral wings mechanism of XB-70 [44] (b) Concorde [9].

In recent years, there have been significant advancements in materials and manufacturing engineering, leading to commercial aircraft development with camber-change morphing designs. FlexSys Incorporated, in collaboration with NASA and the U.S.A.F. launched the Adaptive Compliant Trailing Edge (A.C.T.E.) program. Utilizing the FlexFoil™ variable-geometry control surfaces on the trailing edges allowed seamless wing camber adjustments on a test Gulfstream III Business Jet. To achieve a uniform fluid transition between the morphing and stationary wing sections, compliant

fairings were used, effectively reducing noise levels. Flight tests validated the capability for significant camber morphing at various angles, the ability to perform high-speed spanwise twists, and confirmed the structural integrity, durability, aerodynamic efficiency, morphing stability, and flow separation control offered by FlexFoil™ within the A.C.T.E. technology framework, as illustrated in Figure2.6(a) [45]. In 2016, FlexSys Inc. and Aviation Partners Inc. unveiled a breakthrough in aviation technology with their new FlexFoil™ demonstrator wing, featuring four adaptable control surfaces. This innovation enables the wing to transform shape seamlessly, offering benefits such as decreased drag, enhanced load management, better lift distribution, and roll control, in addition to capabilities like leading-edge droop and de-icing, as dispalyed in Figure 2.6(b) [46].

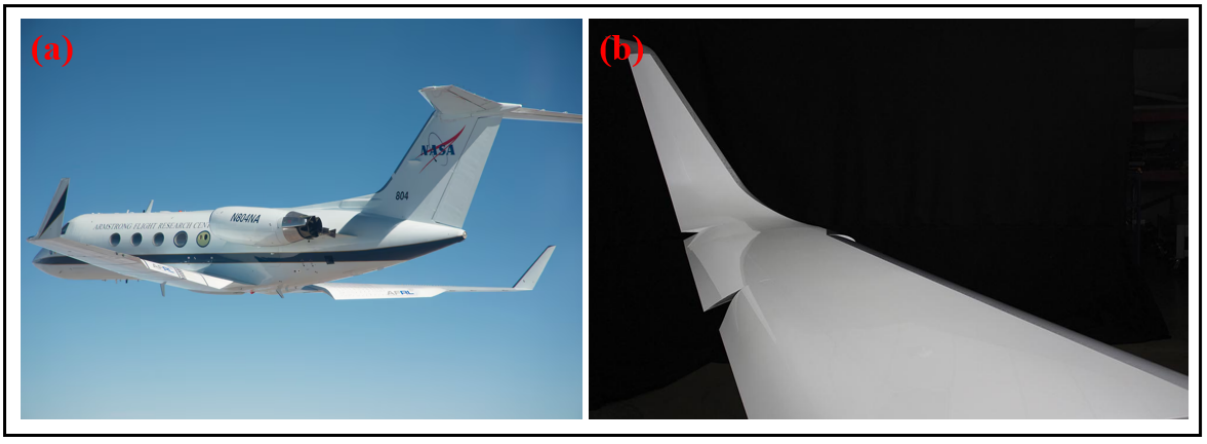

FIGURE 2.6: Camber Wing Morphing on (a) the Gulfstream III Commercial Aircraft and [45] (b) the FlexFoil™ Morphing Technology Demonstrator Wing [46].

2.4 Recent advancements in Camber Wing Morphing

As previously mentioned, there are three primary classifications of wing morphing: in-plane, airfoil, and out-of-plane, as exhibited in Figure 2.7 [47]. In-plane morphing involves alterations made to the wing's structure within the x and y planes, such as changes in span, chord, and sweep angles. In the case of airfoil, it pertains to alterations in

the profile, involving variations in camber rate and thickness. Out-of-plane morphing comprises modifications in the z-plane, such as spanwise bending and camber twisting. Camber broadly refers to the shape, convexity, or unevenness in an airfoil's profile from the front to the back edge. Adjusting the camber continuously provides advantages in terms of distribution of lift, control and reduction of noise from the airframe [48].

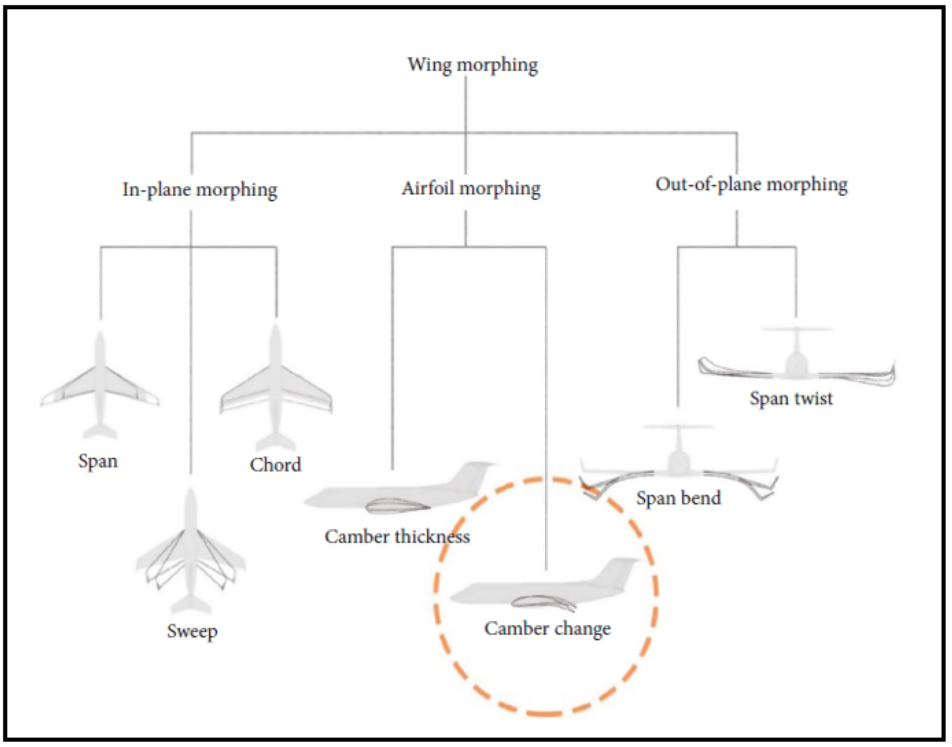

FIGURE 2.7: Types of Wing Morphing [47].

Designing and implementing a wing that can change its camber for testing in a wind tunnel or during actual flight experiments presents a series of challenges. The wing's inner structure must be rigid to resist structural warping and aerodynamic forces, yet it must also be flexible enough to transform shape in desired morphing directions. Consequently, for camber morphing wings, it is essential to explore the wing's ability to morph and how feasible and practical it is to manufacture and implement them for real-world flight scenarios.

Figure 2.8 shows a compliant wing concept to optimize roll control developed by Chanzy and Keane. Their design includes a wing covering that incorporates an open slot at the

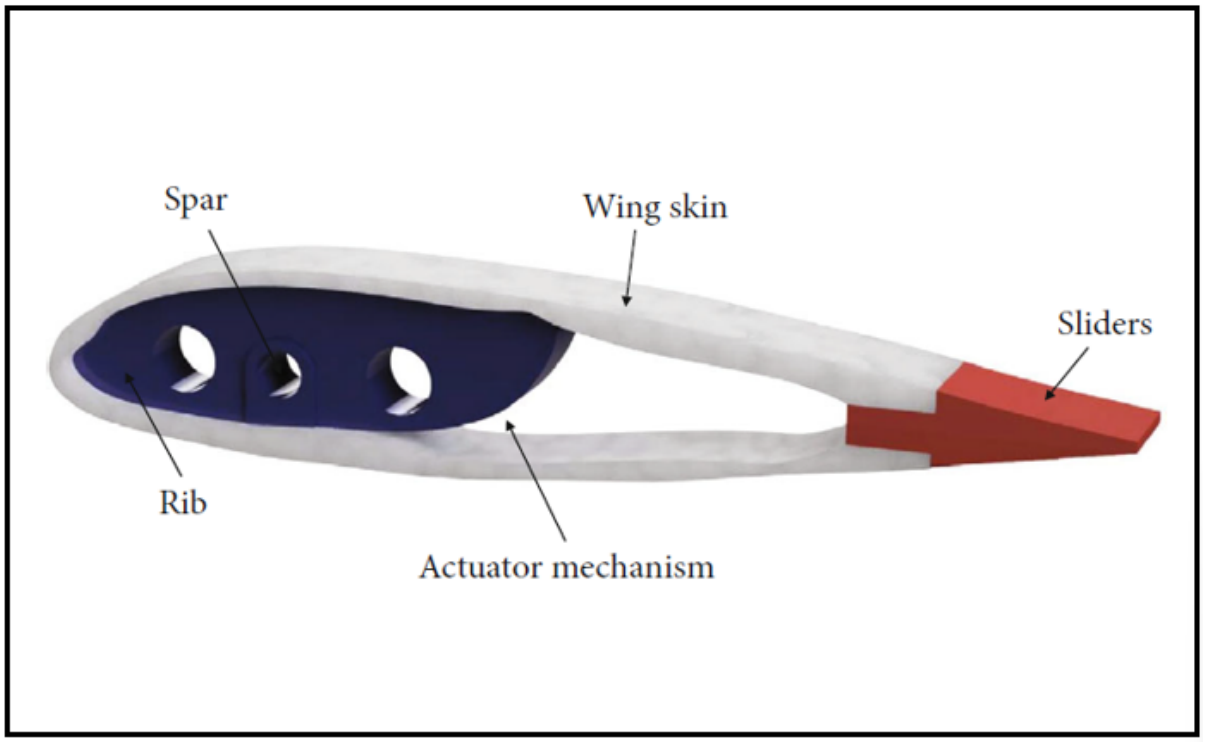

FIGURE 2.8: Design Concept for a Wing Cover with an Open-Slot Trailing Edge [49].

trailing edge, enabling the connection of ribs to the spar while allowing them to remain unattached at the trailing edge. This wing design permits the sliding movement between the upper and lower faces. Morphing is operated through a sets of slotted mechanisms in the trailing edge, interconnected to a controlling actuator. They used FEA and CFD analysis optimization of the design to achieve superior roll control. Additionally, morphing face material thickness was optimized at two internal locations to improve the overall lift coefficient. Their prototype, equipped with a multiturn servomotor for digital command, a worm-and-nut actuation system, a wing skin made of glass-fiber-reinforced polystyrene foam, ribs produced with SLS 3D-printing technology using nylon, and a carbon-fiber spar, underwent testing in a wind tunnel and actual flight conditions. These tests demonstrated a superior L/D ratio compared to traditional wings outfitted with standard ailerons [49].

Yokozeki *et al.* presented the application of corrugated structures within morphing wing sections to adjust wing camber, as shown in Figure 2.9. This concept involves incorporating corrugated elements within top and bottom surfaces fixed around a central

portion. The corrugated designs are reinforced on the upper surface, while a flexible sheet encapsulates the lower side. Each morphing section is controlled by two wired pulley mechanisms operated by motors at both ends for modifications. Computational simulations and physical experiments were conducted to analyze morphing performance under aerodynamic loads. A prototype created from CFRP for both the corrugations and top face confirmed seamless deformation capabilities when activated at a airflow speed of 20 m/s [50, 51].

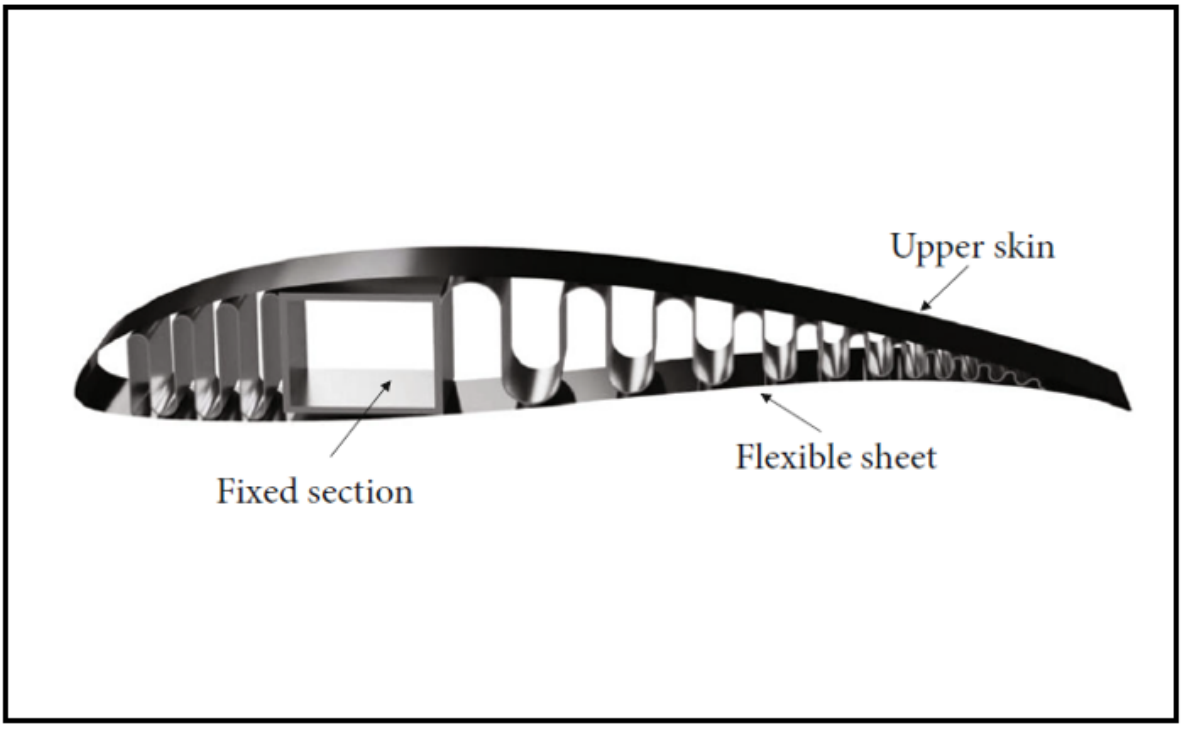

FIGURE 2.9: Design concept involving morphing through cambered corrugated structures [50, 51].

Maki developed and investigated a multi-slotted variable camber mechanism tailored for the NACA 4409 airfoil, as illustrated in Figure 2.10 [52]. This innovative mechanism divides a specific area of the primary airfoil into 5 overlapping segments with 4 slots, which can be morphed to adjust the camber. The mechanism features a linkage system and a control horn powered by a mono motor targeting enhancing STOL capabilities. Wind tunnel experiments have shown that this mechanism provides better lift properties and a considerable increase in stall margin compared to traditional flap and slat setups.

Moreover, Kuya *et al.* conducted computational investigations on the airfoil's multi-slotted design utilizing 2D and 3D Reynolds-averaged Navier-Stokes (RANS) models, focusing on analyzing tip vortices and flow separation phenomena [53].

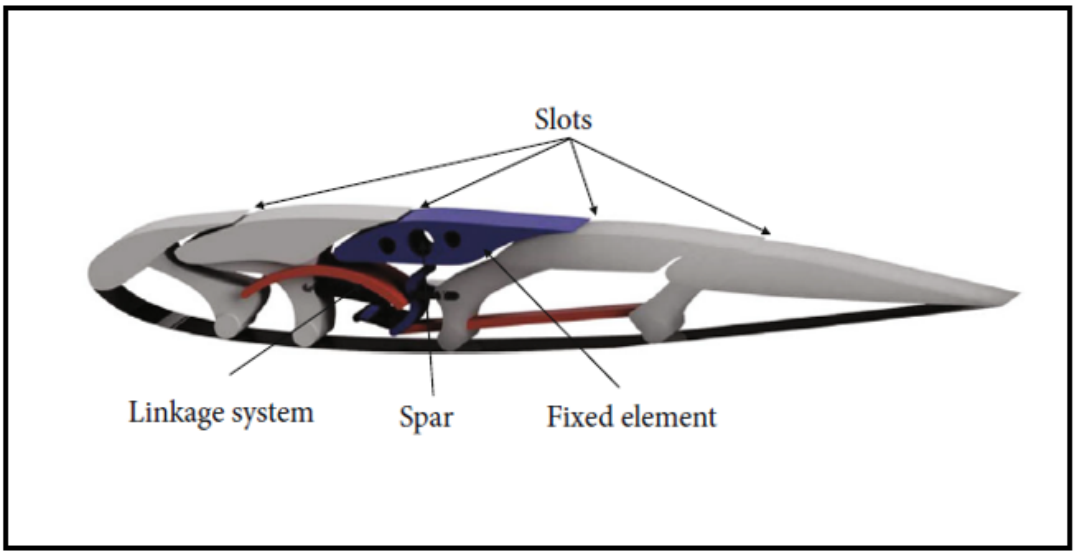

FIGURE 2.10: Design concept involving morphing through multi-slotted variable camber [52].

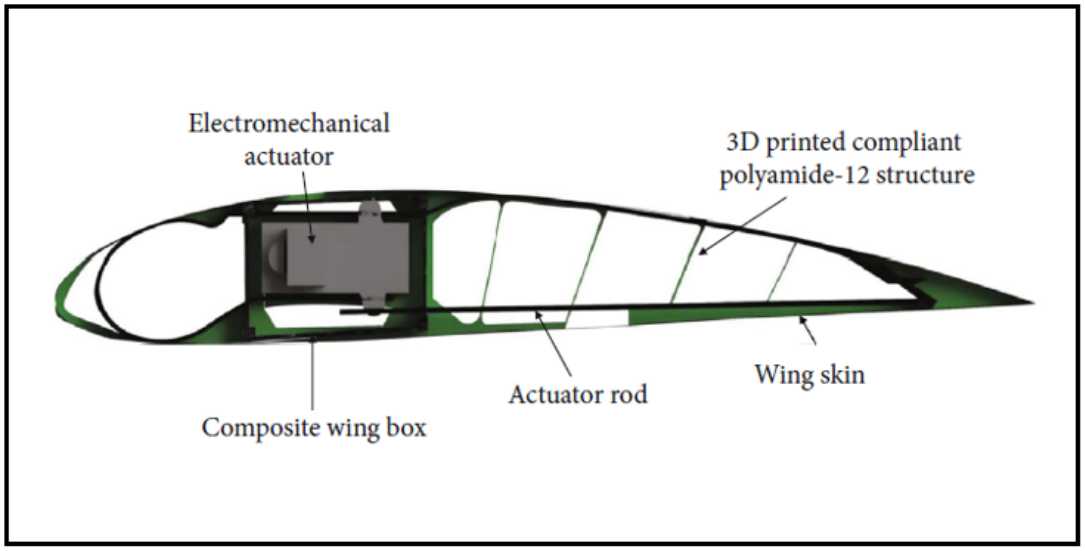

FIGURE 2.11: Design camber morphing concept of Additive Manufactured Drone [54].

A camber morphing mechanism based on materials utilizes anisotropy properties and employs topology optimization for effective material use in its structure. This concept is applied to an additive-manufactured drone and employs distributed compliance

alongside electromechanical actuators to manage control moments, as depicted in Figure 2.11. Constructed using CFRP and polyamide-12, the drone's wing ribs take advantage of the material's anisotropic qualities and robustness. Through push-pull actions generated by actuator rods, the drone's trailing edge is morphed, with each actuator along the wing's span fine-tuning lift distribution to aid in roll control. Flight assessments of the drone displayed enhanced agility and roll rates reaching 240°/s [54].

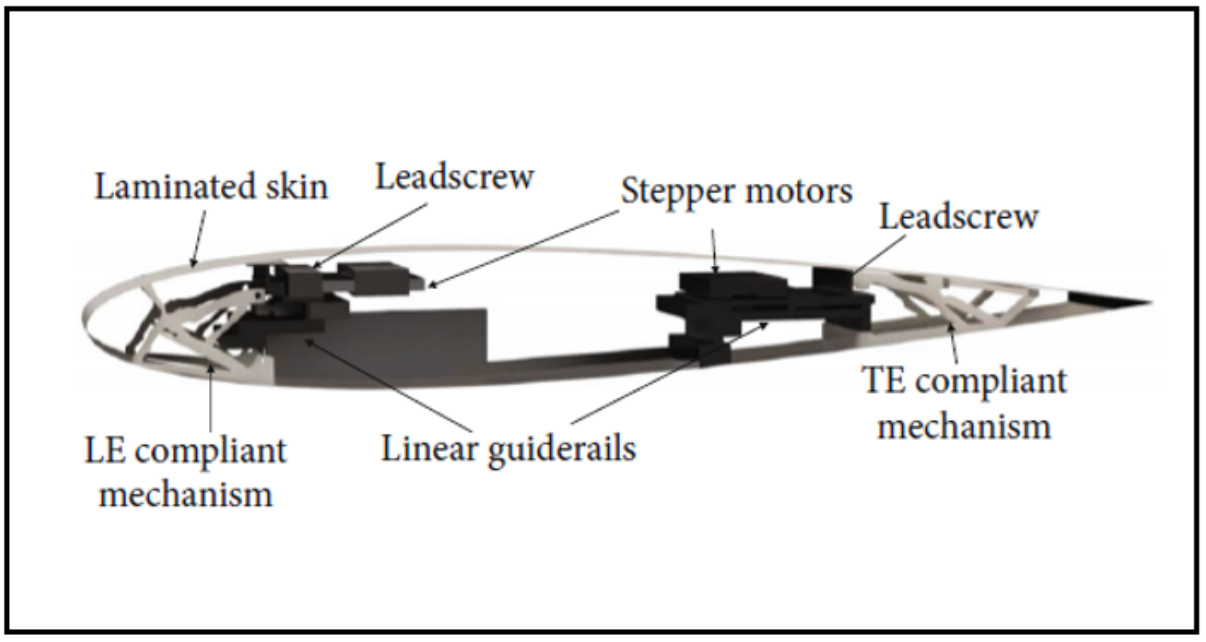

FIGURE 2.12: Design concept with a layered skin and an adaptable camber morphing wing [55].

Zhang and colleagues developed a hybrid variable camber morphing wing that incorporates a monolithic compliant structure at both its leading and trailing edges. The deforming mechanism is activated linearly, altering the wing's exterior profile, as shown in Figure 2.12. For the prototype, materials such as spring steel and glass-fiber reinforced polymer composites were used for the exterior layer, while aluminium was chosen for the structural stringers. The compliant structure was manufactured from elastic PLA using 3D printing technology, and movement was facilitated by a linear stepper motor paired with a lead screw. The experiment showed that the deflection at the leading edge was approximately 27°, while at the trailing edge, deflections varied between -8° and 40° [55].

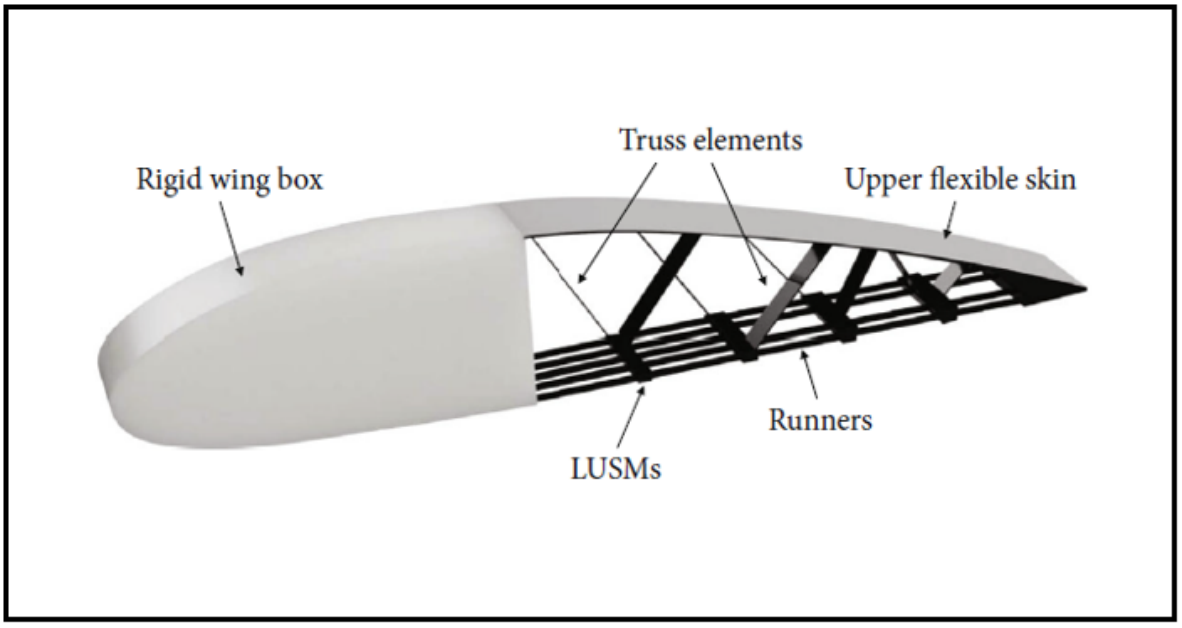

FIGURE 2.13: Design concept on adjustable camber with multiple degrees of freedom [56].

Wu *et al.* suggested a camber morphing approach featuring a multi-degree of freedom (DOF) system, enabling a variety of morphing configurations, as depicted in Figure 2.13. The structure includes a stiff wing box complemented by several compliant truss components. The ends of each truss are secured to the elastic upper face close to the trailing edge through hinges, while their opposite ends are maneuvered by compliant runners powered by linear ultrasonic motors (LUSMs) that employ piezoelectric ceramics. By securing multiple runners to the underneath of the trailing edge and permitting the truss components to glide along these runners via the LUSMs, morphing is accomplished. The design's morphing capability, aerodynamic advantages, and load-bearing capacity were examined and confirmed by testing carbon fiber composite airfoil prototypes and through aerodynamic and aerodynamic advantages and computational studies [56].

The CHIRP smart airfoil is an optimized hybrid camber morphing design that blends structural strength with advanced aerodynamics for improved roll control and reduced air resistance. The model features a semi-monocoque configuration combined with a sturdy

D-spar. The design is further enhanced by a unique section in the middle, based on Voronoi geometry, and a compliant, flexible trailing edge equipped with corrugated patterns on its underside. This airfoil incorporates intelligent materials, such as piezoelectric patches and dielectric elastomers, acting as actuators. These actuators adjust the trailing edge's position, as detailed in Figure 2.14 [57].

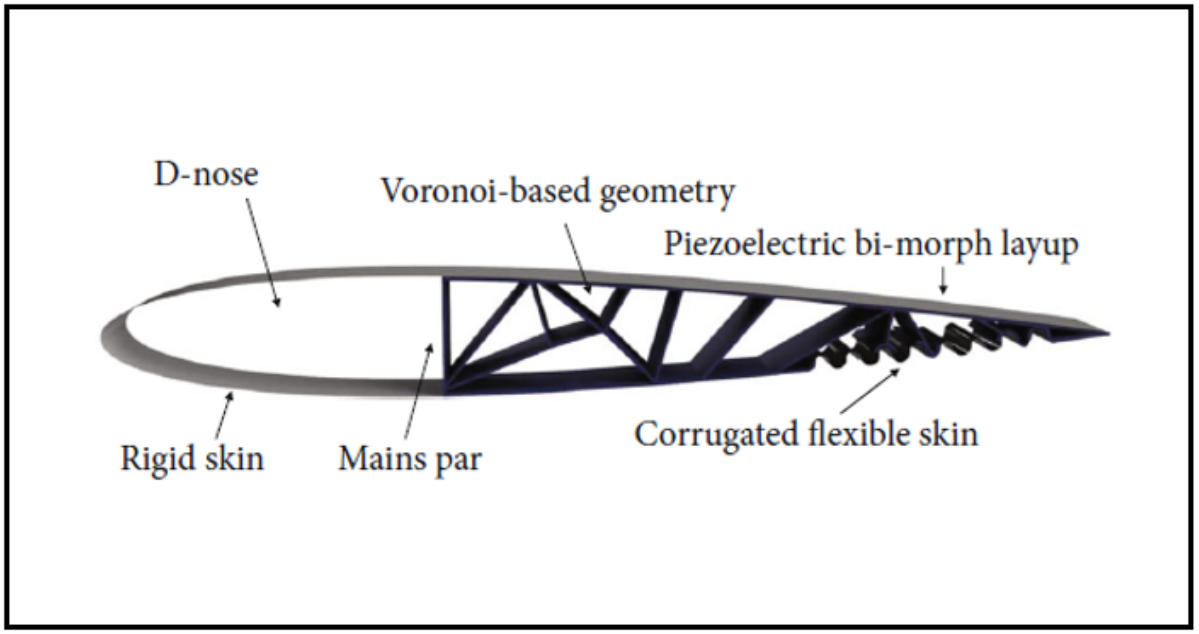

FIGURE 2.14: CHIRP optimized hybrid camber morphing design [57].

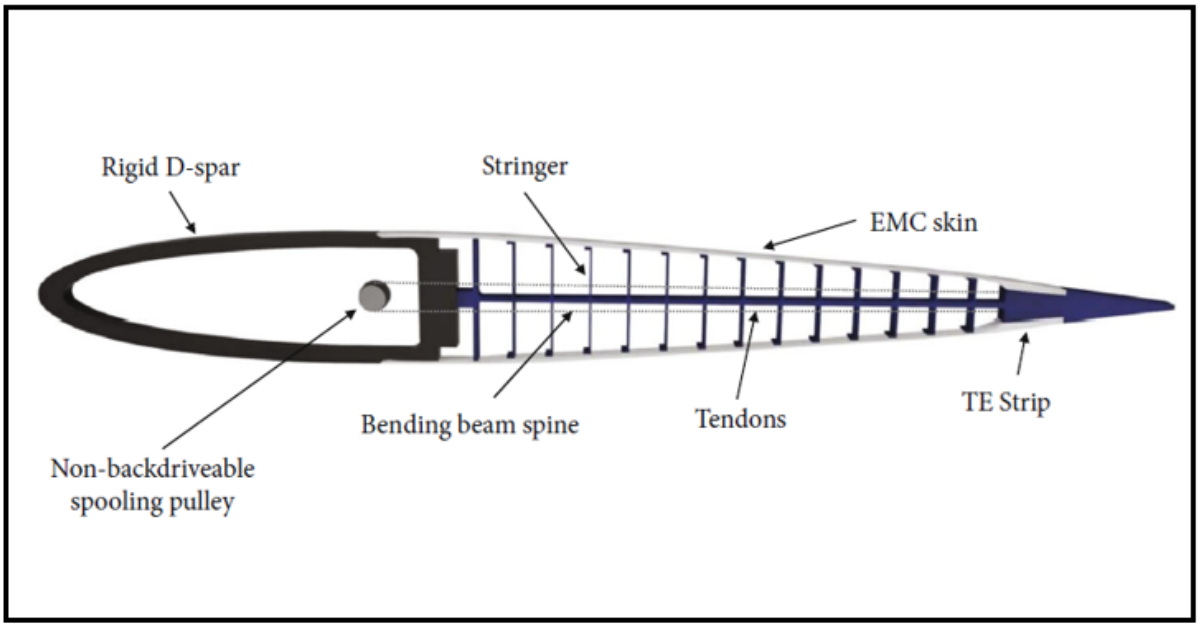

FIGURE 2.15: FishBAC camber morphing design [58, 59].

Woods and Friswell developed the FishBAC (Fish Bone Active Camber) design, taking inspiration from the anatomy of fishfish anatomy. This innovative design features a thin-flexible structure similar to a fish's spine, paired with longitudinal supports resembling fish ribs. These supports are attached to a skin made of pre-tensioned elastomeric matrix composite (EMC), ensuring the outer surface remains at a constant distance from the central spine, therefore preserving the airfoil profile. The central spine's flexibility allows controlled adjustments through bending moments, managed by a system of tendons within the D-spar. These tendons are fixed at one end to the airfoil's trailing edge and at the other to an actuator through a non-backdrivable mechanism such as a worm gear, as depicted in Figure 2.15. The FishBAC prototype made of ABS plastic, underwent wind tunnel experiments, exhibiting an improved L/D ratio in comparison to traditional trailing edge flaps [58, 59].

The emergence of new AM techniques has facilitated the accurate printing of intricate three-dimensional lattice designs. These advancements have had a significant impact and have opened the door to further research on using periodic lattice structures to morph wings. The characteristics of cellular lattice structures can be adjusted with the choice of material and the design's configuration. Due to their porous nature, these structures require minimal material use, making them lightweight while still offering substantial resilience and toughness [60]. The honeycomb cellular frameworks allows the structure to undergo significant strains with zero or negative Poisson ratios, contributing to its superior energy absorption capabilities [61, 62]. The cubic lattice configuration showcases different ways of deforming, such as stretching, bending, and twisting, which vary based on the type and porosity of the unit cell. Lattice structures like F2CCZ primarily experience stretching as their mode of deformation, while lattice structures that are hollow spheres tend to bend [63]. Lattice structures can be integrated into aircraft for structural support, load distribution, and force transmission as essential components in the aircraft's morphing capabilities [6]. Integrating lattices as morphing structures considerably reduces the spaces

between discrete mobile and stationary sections, resulting in a more streamlined airfoil shape or singular monolithic structure capable of modulating as one component.

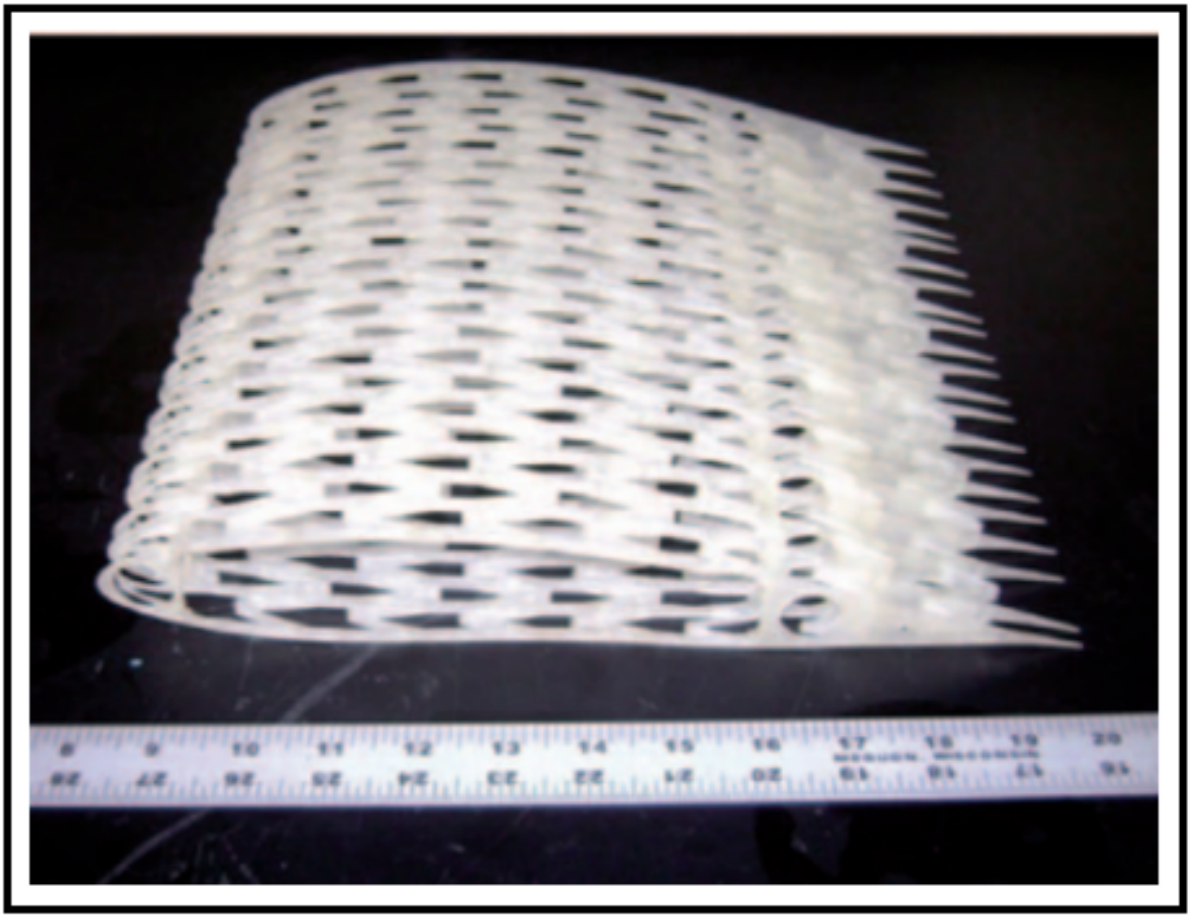

FIGURE 2.16: Morphing prototype fabricated by Vocke and colleagues [64].

Vocke and colleagues developed a morphing-wing segment prototype that could expand its span by 100%, as depicted in Figure 2.16. This design incorporated V-shaped structures connected to the wing's ribs, functioning similarly to springs, to facilitate a morphing process without altering the planar core's ratio (referred to as zero-Poisson morphing). The prototype was crafted using Stereolithography (SLA). It featured an external layer made of a silicone elastomer reinforced with unidirectional carbon fibers to reduce the Poisson effect and ensure the wing maintained a streamlined shape during transformation. The wind tunnel experiment of the prototype demonstrated the ability to morph its span

at velocities reaching 130 km/h, with a maximum deviation from the original plane being just slightly over 0.5 mm [64].

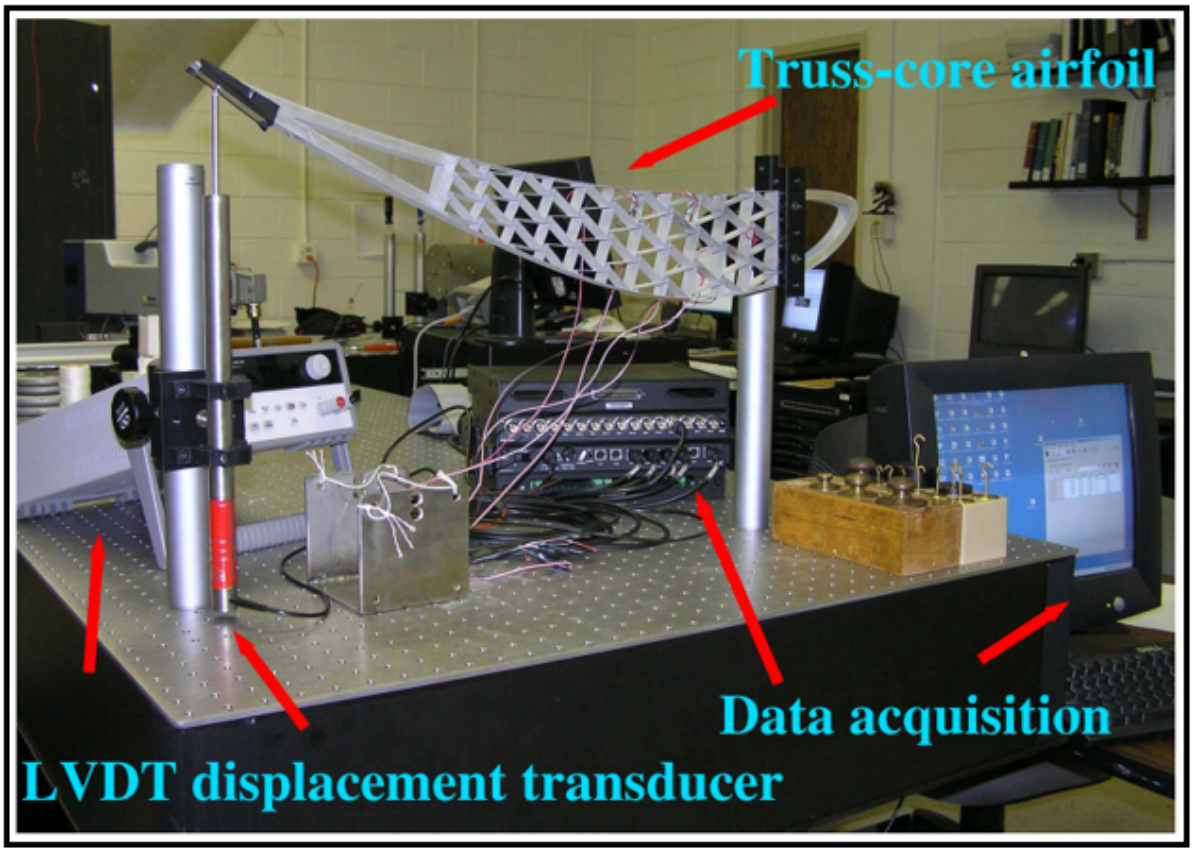

FIGURE 2.17: Experimental setup for the designed wing profile featuring chiral truss structure [12].

Spadoni and Ruzzene developed a novel wing integrating a chiral truss structure, as shown in Figure 2.17. It is chosen for its distinct deformation properties, achieving a theoretical Poisson's ratio of -1. This negative Poisson's ratio leads to a significantly high shear modulus, removing the necessity for either a stressed-skin design or a closed section. The study aimed to explore the airfoil's compliance behavior through experimental assessment, supported by numerical simulations that consider variations due to manufacturing. The study verified the core structure's geometry impacts compliance and demonstrates the capacity of airfoils with a chiral core to undergo significant deformations without breaching the yield strain thresholds [12].

FIGURE 2.18: The proposed prototype of the Wingbox mounted in a low-turbulence wind tunnel [65].

Martin *et al.* used a hexachiral structure as the core to create a passive morphing wing, as indicated in Figure 2.18. Characterized by negative Poisson's ratio, this chiral structure contributes to high levels of deformability while preserving the structural reliability of the wing box. A FEA study performed, integrating a detailed 2D representation of the wing incorporating cellular configuration with a panel code flow analysis tool. Through an iterative solver, the analysis confirmed alterations in the wing's camber prompted by airflow dynamics. A prototype wing was constructed and subjected to wind tunnel experiments to prove the theory. The experimental observations revealed that the final deformed wing configuration matches the finite element analysis projections [65].

Bornengo *et al.*, as illustrated in Figure 2.19, proposed adopting a chiral structure as an internal truss mechanism to design adaptable race car wing boxes. This structure, distinct from traditional symmetric cellular configurations, lacks mirror symmetry and demonstrates a negative Poisson's ratio across a broad range of strains when subjected to load. Computational analysis was performed using FEA combined with a panel code to assess one-way, static fluid-structure interactions. The designed cellular interior enables the wing box to adapt to varying airflow, achieving camber line and trailing edge movement changes, efficiently serving an aileron's purpose [66].

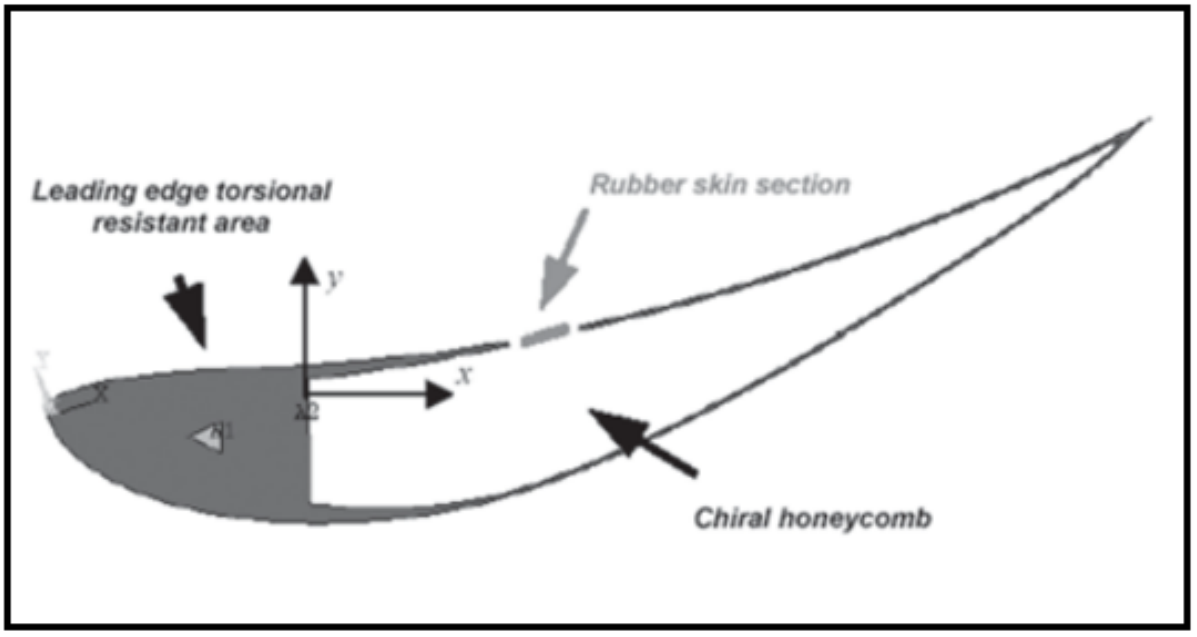

FIGURE 2.19: The proposed design of the race car wing box [66].

Bettini and Airoldi, as illustrated in Figure 2.20, explored the attributes of chiral configurations for wing morphing capacities and introduced a method for their fabrication using composite materials. Experimental findings validate the advantageous characteristics of chiral structures and showcase failure and the non-linear behavior resulting from geometrical influences when subject to large deformations. Altering the sequence of a uniform stacking layout of carbon fabric layers with either glass or carbon layers concluded in improving the morphing efficacy [67].

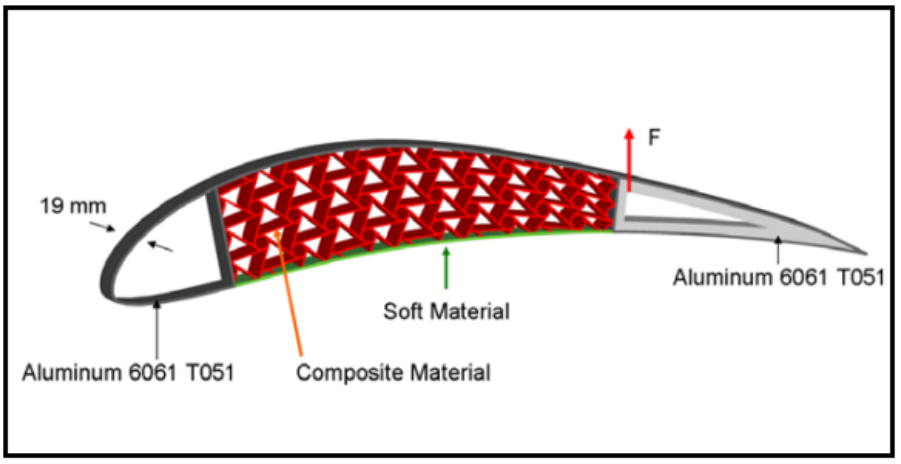

FIGURE 2.20: The proposed design of composite chiral airfoil [67].

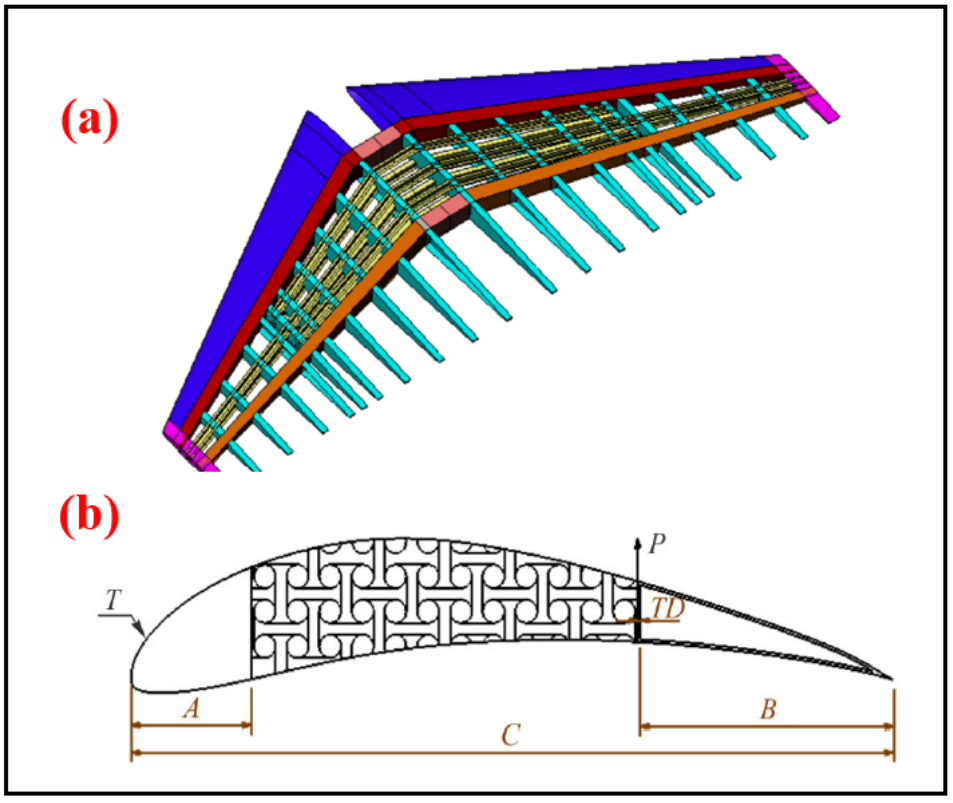

FIGURE 2.21: (a) 3D representation of the composite wing, and (b) an airfoil incorporating auxetic patterns consisting of circular cells [13].

Budarapu *et al.* introduced a methodology for aircraft wing structures that prioritizes structural strength. A numerical study exploring the application of aerodynamic forces as point loads along the wing's span is the basis for calculating shear forces, bending moments, and torsional moments along the wing's spang, as shown in Figure 2.21(a).

These calculations were practically applied to developing a morphing airfoil featuring an auxetic structure, illustrated in Figure 2.21(b). The computational analysis explored the airfoil's compliance characteristics, with findings matching experimental outcomes reported in existing literature [13].

A recent joint project between NASA and MIT produced a flying-wing aircraft incorporating a controllable system into a large-scale, ultralight, and compliant aeroelastic structure. The structure's primary composition includes ortho-octahedral cells, as shown in Figure 2.22, which enable adaptive aeroelastic shape morphing. Moreover, the modular design supports the seamless integration of distributed sensing and computing systems [68].

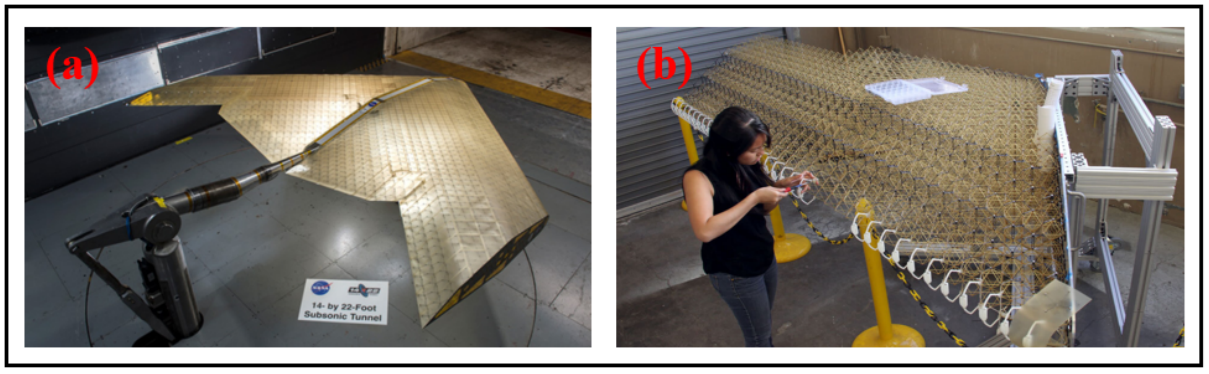

FIGURE 2.22: Design of hollow morphing airplane wing (a) outer structure, and (b) incorporated auxetic patterns consisting of ortho-octahedral cells [68].

2.5 Cellular Structures

Cellular structures, or auxetic mechanical metamaterials, arose as a new innovative approach to develop materials with unconventional mechanical characteristics and enhanced functionalities [69, 70]. These include negative Poisson's ratio, negative elasticity, and negative compressibility [71]. While the term "metamaterials" initially related to optics and electromagnetism, it has now broadened to include any material engineered to possess extraordinary properties not commonly found in the natural world

[72]. The distinctive macroscopic properties of these cellular structures/ auxetic metamaterials originate from the topology of the structure (i.e., their nano/micro-architecture), which can be altered to achieve specific mechanical or physical attributes [73].

Introduced by Evans in 1991, the word "auxetics" derived from the Greek word "auxetikos," which translates to "something that tends to increase" [74]. Unlike conventional materials that shrink when stretched, auxetic structures possess a negative Poisson's ratio, which makes them behave conversely, exhibiting lateral expansion [75]. Within classical mechanics, the presence of auxetic materials in nature is a topic of debate. Nonetheless, researchers have observed auxetic properties in various natural materials, including cancellous bone, cow skin, tendons, specific minerals, and certain zeolites [76]. The three most well-known and established configurations exhibiting a negative Poisson's ratio are re-entrant, chiral, and rotating rigid geometries [77]. Auxetic configurations also offer better mechanical properties, including higher indentation resistance, thermal impact resistance, high shear moduli, and high fracture toughness [78].

2.5.1 Re-entrant hexagonal honeycombs

A honeycomb commonly describes the structured configuration of hexagon-shaped prismatic cells seen in a beehive. Regular hexagonal structures demonstrate uniform characteristics in their plane, but re-entrant hexagonal structures display strong anisotropy [79]. Nonetheless, they offer enhanced lateral Young's and shear modulus compared to regular hexagonal honeycombs. The re-entrant resembles a "bow tie," as illustrated in Figure 2.23(a), which denotes an inward orientation of something or has a negative angle between the ribs of the honeycomb [80]. From Figure 2.23(b), it can be seen that the key mechanism behind the distortion of reentrant configuration lies in the repositioning of cell ribs (hinging), with the bending and longitudinal deformation

(stretching) of the ribs also playing a role in the auxetic response. The lateral shear modulus is heavily impacted by the rib slenderness ratio (w/l), nearing the maximum limit as the rib slenderness ratio decreases [81].

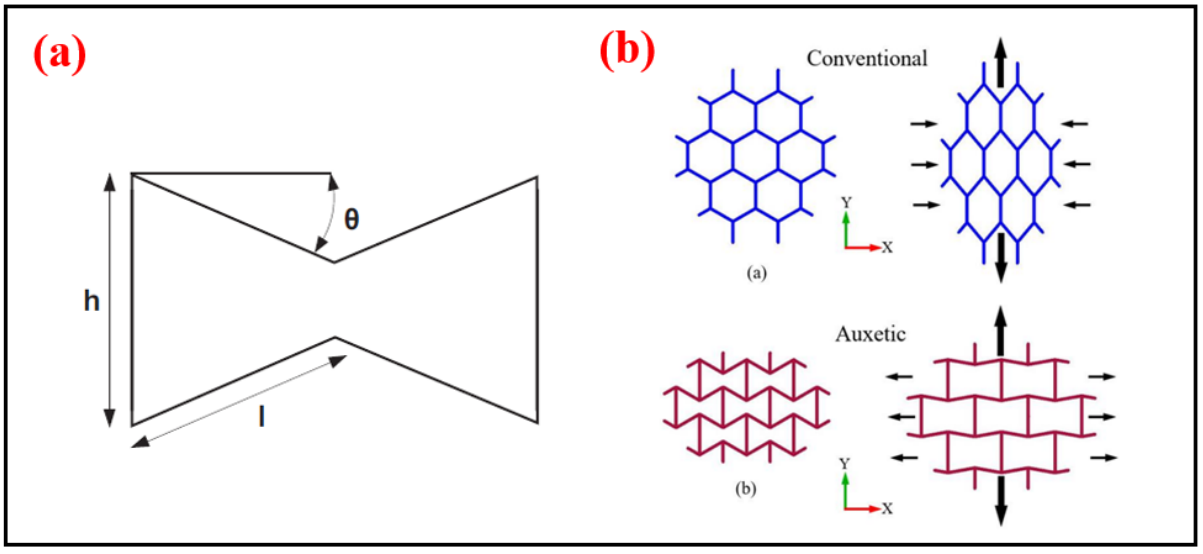

FIGURE 2.23: (a) Re-entrant configuration with θ being the negative re-entrant angle, and (b) Deformation of regular and re-entrant hexagonal honeycomb configurations under tensile loading [80].

Besides the re-entrant hexagonal honeycomb structures, various shapes have emerged that exhibit similar auxetic re-entrant deformation mechanisms. An auxetic arrowhead pattern (referenced as Figure2.23(a)) emerged from numerical topology optimization studies. The unique arrangement of the arrowhead (referenced as Figure 2.24(a)) exhibits a Negative Poisson's Ratio (NPR) of -0.92 when subjected to minor strains [82]. The foam model of the missing rib presents two auxetic arrangements, referred to as the Lozenge grid and the square grid (see Figure 2.24(b)). The arrangements exhibited a negative Poisson's ratio of -0.43 and -0.6, respectively [83]. When the arrows are linked together such that their ends form "stars," it is possible to build configurations that display rotational symmetry with orders of n = 3, 4, and 6. These configurations are identified as STAR-3, STAR-4, and STAR-6, as shown in Figure 2.24(d-f). Subjecting stars to open under unidirectional loading triggers the auxetic effect, and stiffness is calculated by the force constants applied [84].

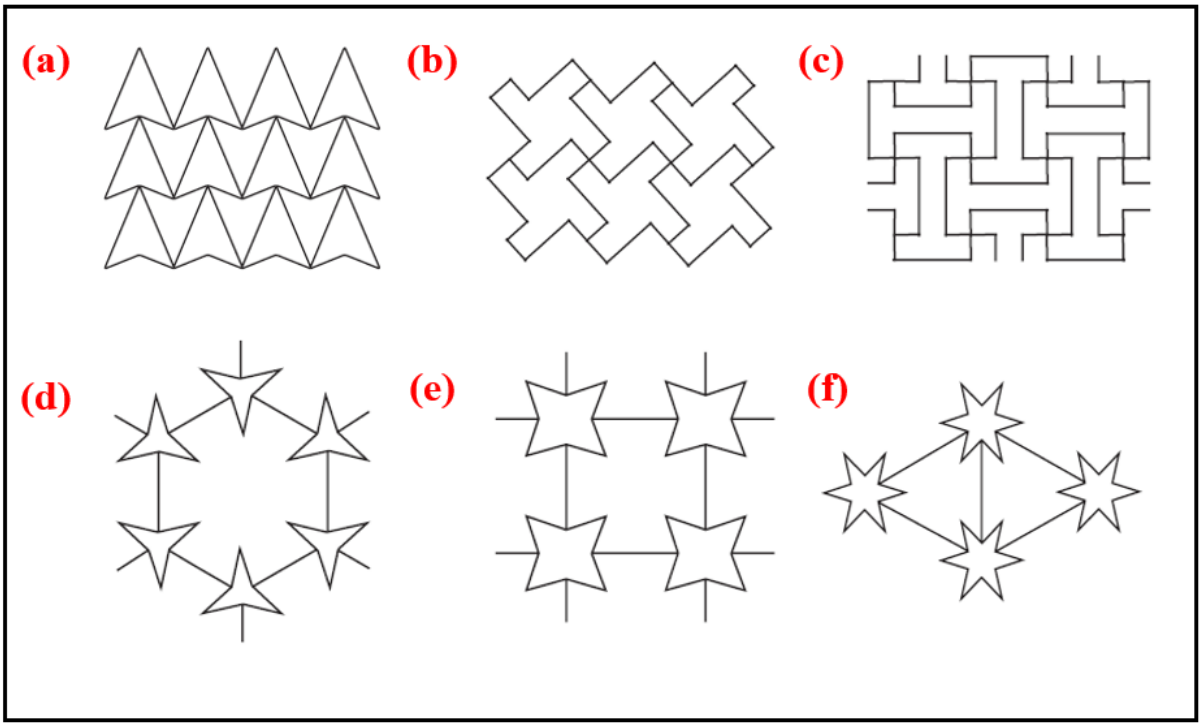

FIGURE 2.24: Other cellular honeycomb configurations: (a) Arrowhead, (b) Lozenge grid, (c) square grid, (d) 3-STAR, (e) 4-STAR, and (f) 6-STAR [82, 83, 84].

2.5.2 Chiral structures

A chiral structure is typically made up of a central cylinder with ligaments attached tangentially displaying distinct auxetic properties exhibiting negative Poisson's ratio approximating -1 upon loading, as displayed in Figure 2.25(a) [85]. The unit structure can be arranged right-handed or left-handed, leading to the formation of chiral or anti-chiral structures, respectively [86]. When these formations undergo mechanical pressure, the spinning of the cylinders causes the ligaments to either fold or unfold in response to tensile or compressive forces, respectively [87].

To construct periodic chiral formations, following the rules of rotational symmetry is mandatory, meaning the total ligaments joined to each node must be equivalent to the rotational symmetry's degree n. If the rule is not modified, as depicted in Figure 2.25(b-f), only 5 distinct configurations can be constructed: trichirals, anti-trichirals, tetra-chirals, anti-tetra-chirals, and hexachirals [70, 87]. Once the restriction on rotational symmetry is

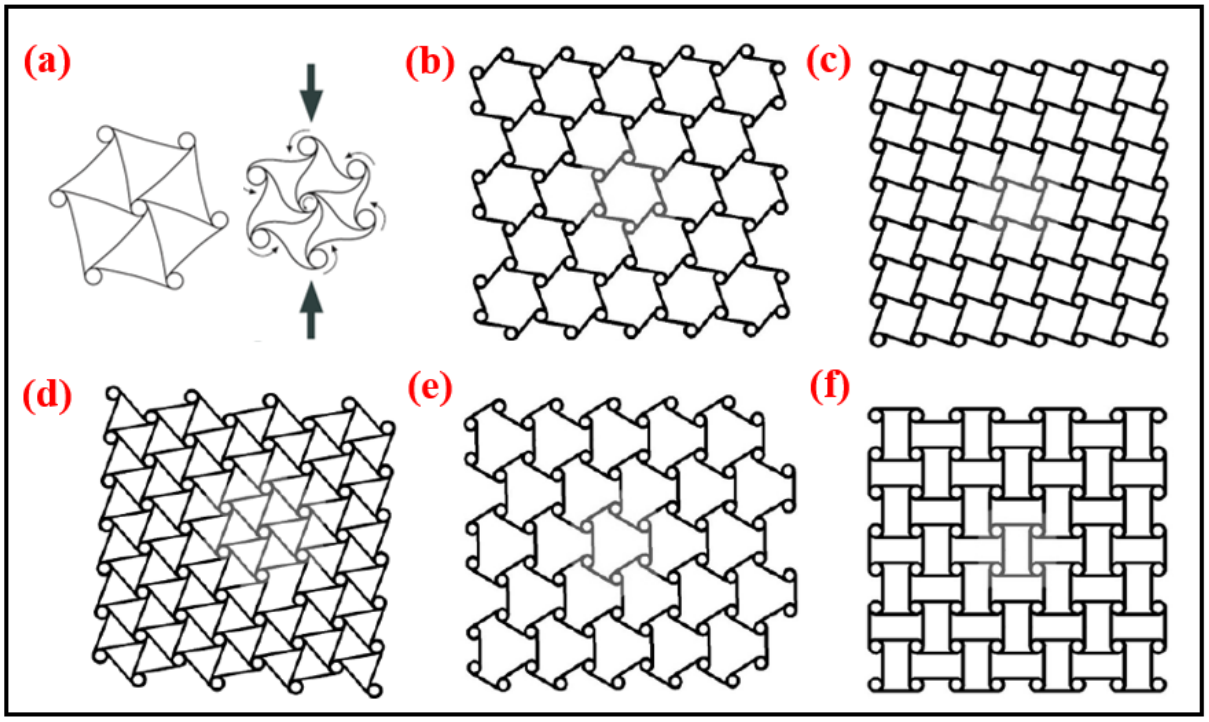

FIGURE 2.25: (a) Response of chiral arrangement under compressive loading; (b) hexachiral arrangement; (c) trichiral arrangement;(d) anti-trichiral arrangement; (e) tetrachiral arrangement; and (f) anti-tetrachiral arrangement [86, 87].

lifted, it becomes possible to design meta-chiral structures [86]. In contrast to re-entrant cells, Poisson's ratio of chiral structures is independent of the structural angle. Chiral structures have the unique feature of "winding" inward when compressed, which enables them to keep their Poisson's ratio constant across a significant strain range of 25% [88, 89]. Increasing the ligament count at each node enhances the stiffness of these structures [87]. Studies have shown that chiral honeycombs demonstrate superior moduli compared to their anti-chiral equivalents despite having an equal number of ligaments [87].

2.5.3 Rotating auxetic structures

A conceptual rotating structure is made up of rigid squares connected by hinges. These squares expand or contract after being loaded by pivoting at their corners [90]. This idea has been widely utilized, incorporating geometric shapes like squares, rectangles, triangles, rhombuses, and parallelograms, as displayed in Figure 2.26.

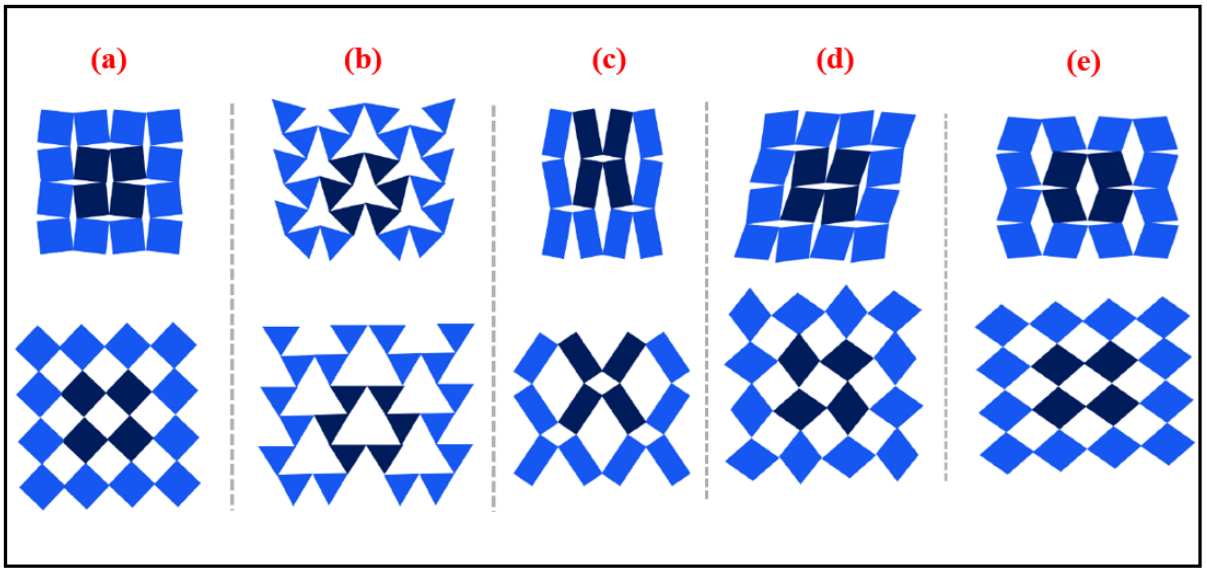

FIGURE 2.26: Distinct states of deformation observed in auxetic configurations: (a) rotating squares; (b) rotating triangles; (c) rotating rectangles; (d) α type rotating rhombi; and (e) β type rotating rhombi [90, 91].

Grima *et al.* were the pioneers in exploring the auxetic capabilities of rotating squares made of rigid material [90]. By applying the conservation of energy principle, they were able to model an ideal system that retains its aspect ratio, leading to a uniform Poisson ratio of -1. Replacing squares with rigid rectangles resulted in distinct behaviors. It was observed that these formations displayed positive as well as negative Poisson's ratio, which varied based on the rectangles' angular orientation. Additionally, a system involving rotating rigid triangles has been proposed to exhibit negative Poisson's ratios [92]. Rhombi can also be organized into two unique configurations, creating Type and Type β rotating rigid rhombi structures, as shown in Figure 2.26(d-e). The Type α structure is characterized by connecting a rhombus's obtuse angle with the acute angle of the adjacent rhombus. On the other hand, the Type β structure involves linking rhombi by matching angles, either acute to acute or obtuse to obtuse [91].

2.6 Research Gaps

Advancements in aerodynamics and the introduction of new morphing technologies have evolved the morphing process from being flexible, to rigid, and now, it has returned to being flexible once more. UAV technology has also played a significant part in this transformation. However, conventional aircraft still use complex and bulky mechanisms, including steering engines, hydraulic systems, linkages, pivots, and a range of systems to alter shape to achieve wing morphing. Most conventional aircraft today predominantly rely on passive morphing, which requires the pilot to follow commands or execute a set of procedures to facilitate the morphing transition. Even though conventional morphing technologies are well established for their accuracy and stability, they still lack in providing advantages in weight reduction and simplicity that novel cellular configurations and advanced materials developed have brought in the past few years.

Researchers employed smart materials and structures to develop autonomous monolithic wing morphing mechanisms. Smart structures or materials can alter their structural configuration in reaction to changes in stimuli, including light, electricity, heat, and pressure, allowing them to simultaneously carry out sensing, actuating, and structural functions. This could significantly reduce the weight and complexity of aircraft. Nonetheless, the desire to use such technology raises a conflicting requirement for finding the right balance between the structural stiffness necessary for load-bearing and the flexibility required for effective morphing. Cellular structures are identified for their enhanced mechanical properties and multifunctional capabilities, making them suitable for superior structural compliant wing morphing designs. The topology of cellular structures controls the auxetic features, implying that these features can be modified to fulfill specific application requirements or to obtain various functionalities.

The potential advantages of cellular lattice structures, such as chiral structures in the context of passive wing morphing, have been recognized; however, direct comparisons with

other cellular structures to determine their relative effectiveness have yet to be conducted. Despite these insights, the literature indicates a lack of research focused on optimizing wing morphing performance using cellular structures to achieve maximum trailing edge deflection while maintaining adequate stiffness. Furthermore, there is a notable absence of discussion regarding the impact of fluid-structure interaction on wing trailing edge deflection when subjected to changes in fluid flow angle of attack. To address the identified gaps in the existing literature, a detailed procedure is outlined in the Aims and Objectives section for developing a novel optimal unit cell to be incorporated within an airfoil auxetic core to achieve maximum trailing-edge deflection.

Chapter 3

Theoretical Background and Methodology

3.1 Introduction

This chapter details the theoretical modeling of auxetic structures and computational methodologies employed to explore the effect of cellular structures or materials on wing morphing in terms of achieving maximum trailing edge deflection. Section 3.2 presents the analytical modelling of the reentrant hexagonal honeycomb structures developed by Hedayati *et al.* Section 3.3 introduces the mathematics and employment of a MOGA to develop an optimal reentrant auxetic unit cell configuration with optimal elastic modulus and maximum negative Poisson's ratio. Section 3.4 presents the theoretical background of computational fluid dynamics techniques covering airfoil to turbulence models. Section 3.5 provides a brief overview of the airfoil profile and selected airfoil for this research. Sections 3.6, 3.7, and 3.8 detail the CAD modeling of the airfoil containing auxetic core alongside computational setups utilizing ANSYS commercial software to perform FEA structural and CFD decoupled fluid structural analysis.

3.2 Reentrant Auxetic Structure Analytical Modelling

This section begins with an analytic formulation presented by Hedayati *et al.* to derive the mathematical relationships for elastic properties, particularly elastic modulus, and Poisson's ratio [93]. The external forces required to be applied to a d.o.f q_i are denoted by Q_i. The force-displacement correlation of this system is expressed as follows:

$$\begin{Bmatrix} Q_1 \\ Q_2 \\ Q_3 \\ Q_4 \end{Bmatrix} = \begin{bmatrix} k_{11} & k_{12} & k_{13} & k_{14} \\ k_{21} & k_{22} & k_{23} & k_{24} \\ k_{31} & k_{32} & k_{33} & k_{34} \\ k_{41} & k_{42} & k_{43} & k_{44} \end{bmatrix} \begin{Bmatrix} q_1 \\ q_2 \\ q_3 \\ q_4 \end{Bmatrix} \tag{3.1}$$

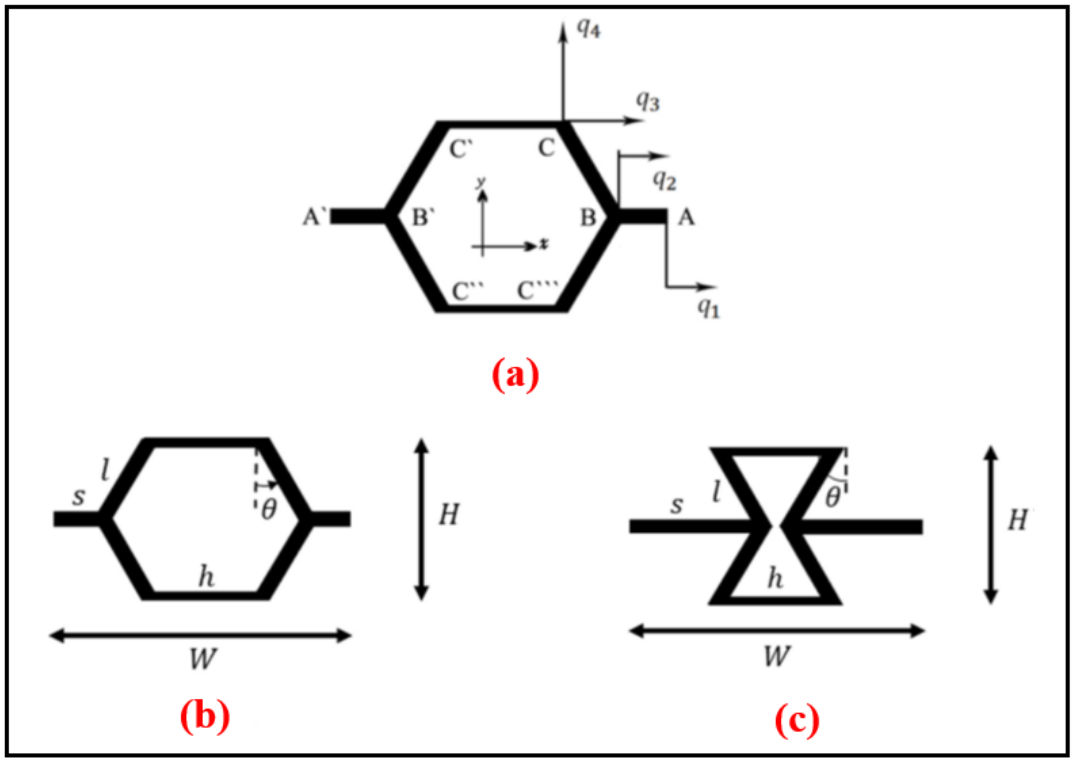

FIGURE 3.1: Figure representing (a) degree of freedoms for a unit cell configuration, (b) design of hexagonal honeycomb configuration, (c)design of a re-entrant hexagonal honeycomb configuration [93].

To compute the displacements, rotations, forces, and moments as a function of the applied force F, it is essential to determine elements of stiffness matrix, denoted as k_{ij}. This is

a critical step for computing the elastic properties of a unit cell. As illustrated in Figure 3.1, it becomes clear that

$$s = \frac{1}{2}\left(W - Htan\theta - h\right) \tag{3.2}$$

$$l = \frac{H}{2\ cos\theta} \tag{3.3}$$

The deformations within each beam element can be categorized into 3 distinct deformation categories: (a) lateral displacement δ without any rotation, (b) rotation θ without lateral shifting, and (c) pure axial extension. Figure 3.2 illustrates the required forces and moments needed to achieve each type of deformation.

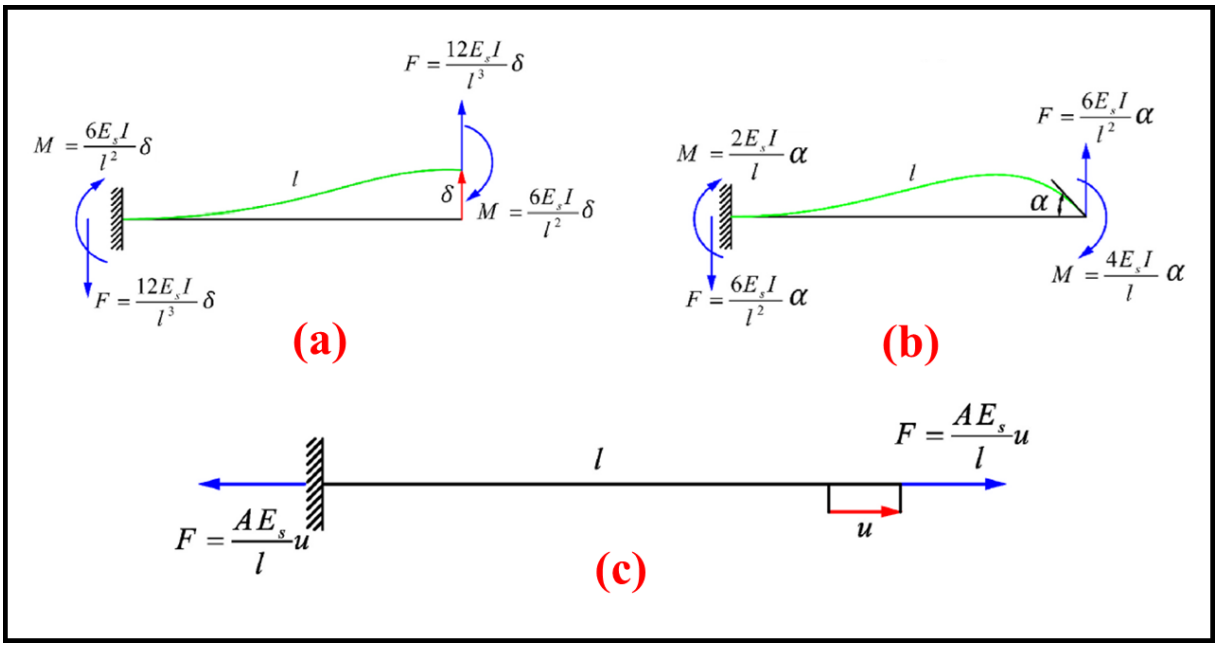

FIGURE 3.2: Figure representing forces and moments needed to cause (a) lateral displacement δ without rotation, (b) rotation θ without lateral displacement, and (c) pure longitudinal expansion at loose end of an EB beam [93].

Case 1: $q_1 = 1$

For case 1, the elements of the stiffness matrix's first column are calculated by assigning a displacement value of $q_1 = 1$ while keeping q_2, q_3, and q_4 at zero. This deformation leads to the outward and inward movements of the vertices A and A' by one unit each, respectively.

Due to this particular shift, the strut labeled AB undergoes an axial extension of one unit, causing it to apply a force labeled $\frac{AE_s}{s}$ (as shown in Figure 3.3) at vertices A and B.

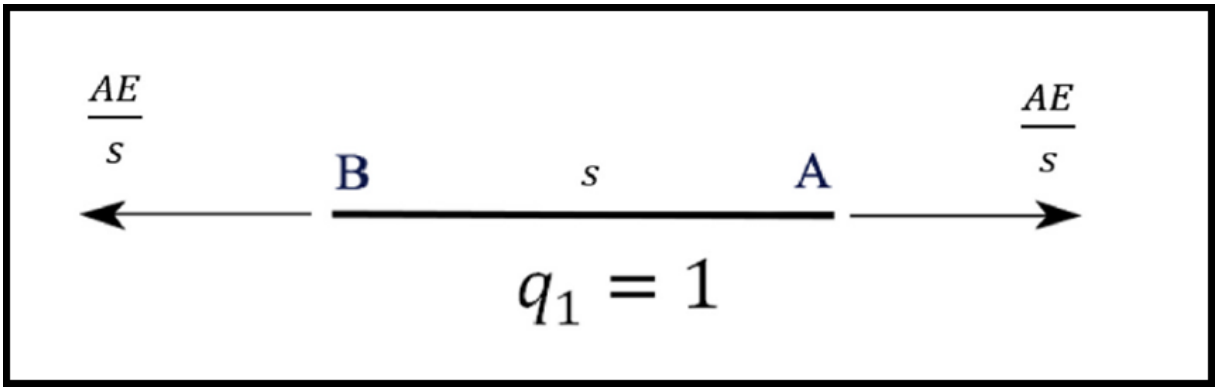

FIGURE 3.3: FBD of the ligament AB under extension with $q_1 = 1$ [93].

To achieve such a deformation, forces $\frac{Q_1}{2} = \frac{AE}{s}$ and $\frac{Q_2}{2} = \frac{-AE}{s}$ must be applied to vertices A and B. In other words, $Q_1 = k_{11} = \frac{2AE_s}{s}$ and $Q_2 = k_{11} = \frac{-2AE_s}{s}$. The negative value of Q_2 indicates that an external load must be applied to vertex B in the direction opposite to DOF q_2 to keep vertex B stationary. Since beams BC and CC' are unaffected by this deformation mode, no external force is needed at Point C; hence, $Q_3 = k_{31} = Q_4 = k_{41} = 0$.

Case 2: $q_2 = 1$

For case 2, beams AB undergo pure compression. Unlike the case where $q_1 = 1$, here we have $\frac{Q_1}{2} = \frac{-AE}{s}$ (Figure 3.4a). In contrast to the previous case, beam BC is deformed. Vertex A remains fixed while vertex B moves one unit to the right. The displacement of vertex B can be broken down into two components: $\cos\theta$ perpendicular to the undeformed beam BC and $\sin\theta$ along it. The axial displacement causes a force of $\frac{AEsin\theta}{l}$ and the lateral displacement imposes a force of $\frac{12EI}{l^3}\cos\theta$ on beam BC. The equilibrium of forces in the X direction at Point B is shown in Figures 3.4(a) and 3.4(b).

$$\sum f_{X,B} = 0 \rightarrow -2\left(\frac{AE_s}{l}\sin^2\theta + \frac{12E_sI}{l^3}\cos^2\theta\right) - \frac{AE_s}{s} + \frac{Q_2}{2} = 0 \tag{3.4}$$

$$\rightarrow Q_2 = k_{22} = 4\left(\frac{AE_s}{l}\sin^2\theta + \frac{12E_sI}{l^3}\cos^2\theta\right) + \frac{2AE_s}{s} \tag{3.5}$$

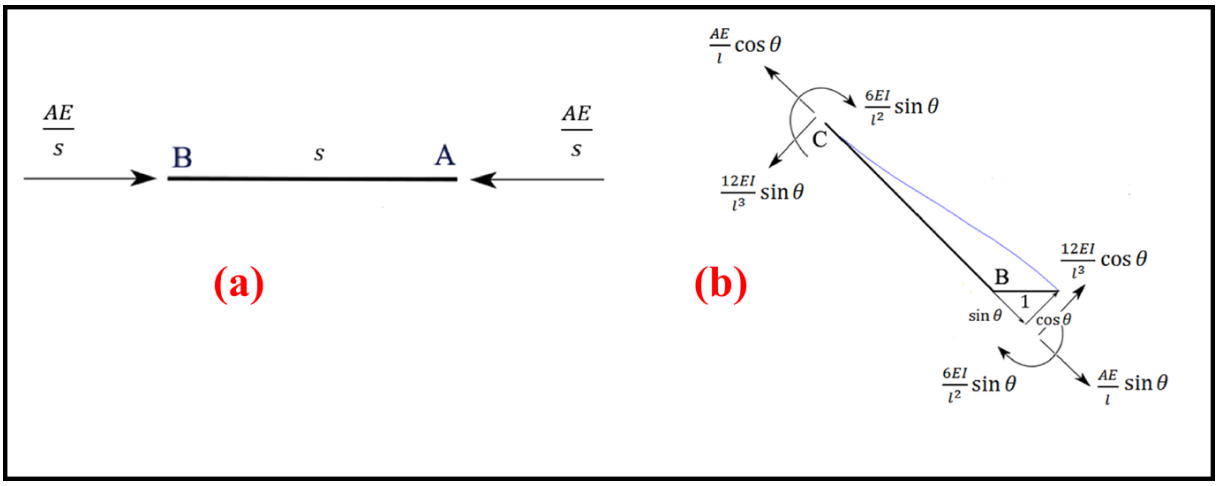

FIGURE 3.4: Free-body diagram of the ligaments AB and BC under compression with $q_2 = 1$ [93].

Beam CC' is fixed and does not exert any force on vertex C. Similarly, the equilibrium of forces in the Y direction at Point C is shown in Figure 3.4(b).

$$\sum f_{Y,C} = 0 \rightarrow -\left(\frac{AE_s}{l}\cos\theta\sin\theta + \frac{12E_sI}{l^3}\cos\theta\sin\theta\right) + \frac{Q_4}{4} = 0 \tag{3.6}$$

$$\rightarrow Q_4 = k_{42} = 4\cos\theta\sin\theta\left(\frac{AE_s}{l} + \frac{12E_sI}{l^3}\right) \tag{3.7}$$

From Figure3.4(b) equilibrium forces in the X direction at vertex C gives

$$\sum f_{X,C} = 0 \rightarrow \left(\frac{AE_s}{l}\cos^2\theta + \frac{12E_sI}{l^3}\sin^2\theta\right) + \frac{Q_3}{4} = 0 \tag{3.8}$$

$$\rightarrow Q_3 = k_{32} = 4\left(\frac{AE_s}{l}\cos^2\theta + \frac{48E_sI}{l^3}\sin^2\theta\right) \tag{3.9}$$

Case 3: $q_3 = 1$

For case 3, this type of deformation shifts vertex C one unit to the right (Figure A21a).

Beam AB remains undeformed; therefore, no load is imposed on point B. Additionally, point A is unaffected by this deformation mode, so $Q_1 = k_{13} = 0$.

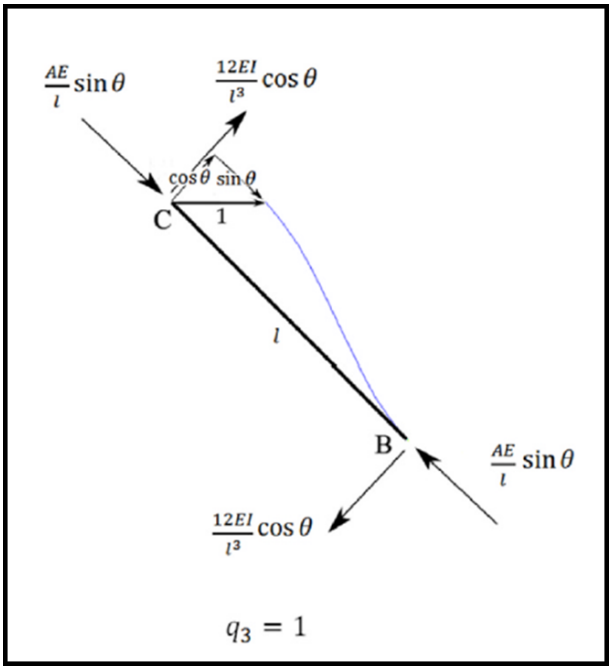

FIGURE 3.5: FBD of the ligament BC under deformation $q_3 = 1$ [93].

The equilibrium forces in the X direction at Point B, as demonstrated in Figure 3.5, can be written as:

$$\sum f_{X,B} = 0 \rightarrow 2\left(\frac{AE_s}{l}\sin^2\theta + \frac{12E_sI}{l^3}\cos^2\theta\right) + \frac{Q_2}{2} = 0 \tag{3.10}$$

$$\rightarrow Q_2 = k_{23} = -4\left(\frac{AE_s}{l}\sin^2\theta + \frac{12E_sI}{l^3}\cos^2\theta\right) \tag{3.11}$$

Beam CC', with a length of h and a cross-sectional area of $\frac{A}{2}$, is stretched by 2 units, thereby exerting a force of $\frac{AE_s}{h}$ on Point C. The equilibrium of forces in the X direction at Point C is given by:

$$\sum f_{X,C} = 0 \rightarrow -\frac{AE_s}{l}\sin^2\theta - \frac{12E_sI}{l^3}\cos^2\theta - \frac{AE_s}{h} + \frac{Q_3}{4} = 0 \tag{3.12}$$

$$\rightarrow Q_3 = k_{33} = \frac{4AE_s}{l}\sin^2\theta + \frac{48E_sI}{l^3}\cos^2\theta + \frac{4AE_s}{h} \tag{3.13}$$

Similarly, the equilibrium of forces at Point C in the Y direction is given by:

$$\sum f_{Y,C} = 0 \rightarrow \cos\theta\sin\theta\left(\frac{AE_s}{l} - \frac{12E_sI}{l^3}\right) + \frac{Q_4}{4} = 0 \tag{3.14}$$

$$\rightarrow Q_4 = k_{43} = \cos\theta\sin\theta\left(\frac{48E_sI}{l^3} - \frac{4AE_s}{l}\right) \tag{3.15}$$

Case 4: $q_4 = 1$

For case 4, this type of deformation moves vertex C one unit upwards (Figure 3.6). As with the case where $q_3 = 1$, here $Q_1 = k_{14} = 0$. The equilibrium of forces at Point B in the X direction is shown in Figure 3.6.

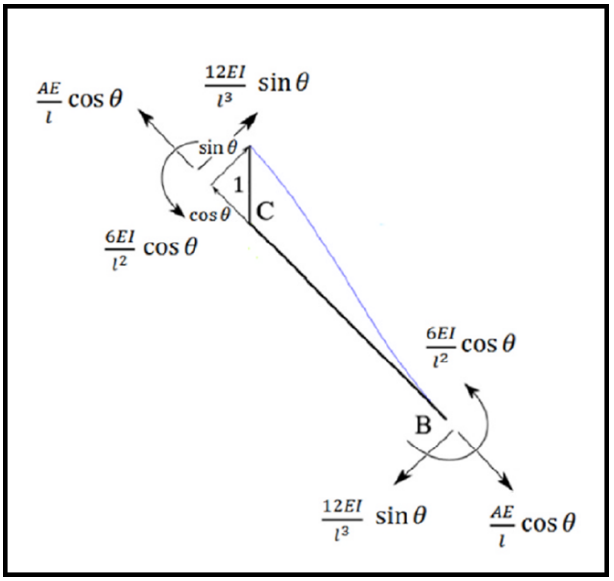

FIGURE 3.6: FBD of the ligament BC under deformation $q_4 = 1$ [93].

$$\sum f_{X,B} = 0 \rightarrow -\frac{2AE_s}{l}\cos\theta\sin\theta + \frac{24E_sI}{l^3}\cos\theta\sin\theta + \frac{Q_2}{2} = 0 \tag{3.16}$$

$$\rightarrow Q_2 = k_{24} = \left(\frac{4AE_s}{l} - \frac{48E_sI}{l^3}\right)\cos\theta\sin\theta \tag{3.17}$$

Beam CC' moves without deformation, so it does not apply any load to Point C. The equilibrium of forces at Point C in the Y direction is given by:

$$\sum f_{Y,C} = 0 \rightarrow -\frac{AE_s}{l}\cos^2\theta - \frac{12E_sI}{l^3}\sin^2\theta + \frac{Q_4}{4} = 0 \tag{3.18}$$

$$\rightarrow Q_4 = k_{44} = \frac{4AE_s}{l}\cos^2\theta + \frac{48E_sI}{l^3}\sin^2\theta \tag{3.19}$$

Similarly, the equilibrium of forces at Point C in the X direction is given by:

$$\sum f_{X,C} = 0 \rightarrow \cos\theta\sin\theta\left(\frac{AE_s}{l} + \frac{12E_sI}{l^3}\right) + \frac{Q_3}{4} = 0 \tag{3.20}$$

$$\rightarrow Q_3 = k_{34} = \cos\theta\sin\theta\left(\frac{48E_sI}{l^3} - \frac{4AE_s}{l}\right) \tag{3.21}$$

The total forces from outside acting on point B are zero, and similarly, on the vertex C in the X direction is also zero; therefore, $Q_2 = Q_3 = 0$. Conversely, the force acting on point C in the Y direction is $\sigma_y bW$, and the external force on point A is $\sigma_x bH$. Therefore, the force vector is:

$$\begin{Bmatrix} Q_1 \\ Q_2 \\ Q_3 \\ Q_4 \end{Bmatrix} = \begin{Bmatrix} \sigma_x bH \\ 0 \\ 0 \\ \sigma_y bW \end{Bmatrix} \tag{3.22}$$

The elastic modulus in each direction is determined by dividing the stress in that direction (i.e., $\frac{\sigma_x W}{2q_1}$ in the X direction and $\frac{\sigma_y H}{2q_4}$ in the Y direction) by the strain in that direction. The relative elastic modulus in the X direction is obtained by substituting $\sigma_y = 0$ as follows:

$$\left(\frac{E}{E_s}\right)_X = \frac{Wt^3 cos\theta}{H\left\{l\left(l^2-t^2\right)cos^3\theta + t^2\left(l+W\right)cos\theta - Ht^2 sin\theta\right\}} \tag{3.23}$$

Similarly,the relative elastic modulus in the Y direction can be written as:

$$\left(\frac{E}{E_s}\right)_Y = \frac{Ht^3}{Wl\left\{\left(l^2-t^2\right)sin^2\theta + t^2\right\}} \tag{3.24}$$

The Poisson's ratio can be determined by dividing the strains in the X and Y directions. For ν_{xy}, it is given by $\nu_{xy} = -\frac{\epsilon_y}{\epsilon_x} = \frac{q_2}{q_1}\frac{W}{H}$ when $\sigma_y = 0$. From F-D relation, the Poisson's ratio ν_{xy} is calculated as follows:

$$\nu_{xy} = \frac{Wl\cos^2\theta\sin\theta\left(l^2-t^2\right)}{H\left\{l\left(l^2-t^2\right)cos^3\theta + t^2\left(l+W\right)cos\theta - Ht^2 sin\theta\right\}} \tag{3.25}$$

For ν_{yx}, it is given by $\nu_{yx} = -\frac{\epsilon_x}{\epsilon_y} = \frac{q_1}{q_4}\frac{H}{W}$ when $\sigma_x = 0$. From F-D relation, the Poisson's ratio ν_{yx} is calculated as follows:

$$\nu_{yx} = \frac{H\left(l^2-t^2\right)\sin(2\theta)}{2W\left\{\left(l^2-t^2\right)sin^2\theta + t^2\right\}} \tag{3.26}$$

3.3 Multi-Objective Genetic Algorithm

In problems involving multiple objectives, it's common to encounter objectives that conflict or make it difficult to optimize them simultaneously. This scenario is frequently observed in engineering challenges, where the goals often include reducing costs, enhancing performance, and improving reliability. Addressing such issues is challenging yet practical. Genetic algorithms (GAs), a widely used meta-heuristic method, are particularly effective for these problems. To adapt traditional GAs for multi-objective scenarios, they utilize specific fitness functions and techniques that encourage various solutions.

Two main strategies exist for tackling multi-objective optimization problems. The first strategy involves merging multiple target functions into one comprehensive function or relegating all objectives except one to the constraints category. With first strategy, a single objective can be determined using methods like the weighted sum method or utility theory. The main challenge, however, comes from the need to precisely choose the correct weights or utility functions that accurately reflect the preferences of the decision-maker. The second strategy identifies a complete set of Pareto optimal solutions or a significant subset. A collection of Pareto optimal solutions includes options that are not dominated when compared to one another. Transitioning from one Pareto solution to another invariably involves a compromise, as enhancing one objective necessitates declining performance in another area [94].

Holland and his team developed the concept of genetic algorithms (GAs) after getting influenced from the principles of evolutionary biology, which accounts for the evolution of species, GAs mimic this natural process. In the wild, species that are not adaptable or strong enough eventually die out due to natural selection, whereas those that are more robust stand a better chance of passing their genes on to the next generation through reproduction. Over periods, species that acquire the most advantageous genetic combinations tend to prevail within their communities. Occasionally, random genetic mutations occur, and such alterations prove beneficial; they lead to new and better species emerging from the existing ones. Conversely, unsuccessful mutations are weeded out by natural selection [95].

MOGA represented the initial genetic algorithm that combined Pareto-based ranking and niching techniques in a multi-objective context explicitly [96]. This method led the search closer to the true Pareto front while keeping the variety in the population intact. Thus, MOGA stands out as a prime illustration of how to effectively combine Pareto-based ranking with fitness sharing in a multi-objective genetic algorithm. Below is a summary of the MOGA process [97]:

Step 1: Start by creating an initial population P_0 through random generation.

Step 2: Terminate and return P_t if the pre-defined stopping criteria are met.

Step 3: Conduct a fitness assessment of the current population using the steps below:

Step 3.1: For each solution x in the population P_t, calculate its ranking $r(x,t)$ according to the ranking method outlined in the following Equation:

$$r\left(x,t\right)=1+\ nq\left(x,t\right) \tag{3.27}$$

where nq(x,t) represents the total solutions that dominate solution x during the generation at time t.

Step 3.2: Based on their rankings, allocate fitness scores to each solution as follows.

$$f\left(x,t\right)\ =\ N-\sum_{k=1}^{r(x,t)-1}n_k-0.5\times\left(n_{r(x,t)}-1\right) \tag{3.28}$$

where nk denotes the total solutions that have a rank of k.

Step 3.3: For each solution x that belongs to P_t, compute its niche count using the equation below, where σ_{share} is the niche size.

$$nc\left(x,t\right)=\sum_{y\epsilon P,\ r(y,t)\ =r(x,t)}max\left\{\frac{\sigma_{share}-dz\left(x,y\right)}{\sigma_{share}},0\right\} \tag{3.29}$$

Step 3.4: Determine the shared fitness value for every solution x within P_t using the following method:

$$f'\left(x,t\right)\ =\frac{f\left(x,t\right)}{nc\left(x,t\right)} \tag{3.30}$$

Step 3.5: Adjust the fitness values by applying the normalized shared fitness values.

$$f^{"}\left(x,t\right)=\frac{f^{'}\left(x,t\right)}{\sum_{y\epsilon P_t\ r(y,t)=r(x,t)}f'\left(x,t\right)}f\left(x,t\right) \tag{3.31}$$

Step 4: Employ a stochastic selection process, guided by the fitness metric, to select parents for breeding. Conduct crossover and mutation within this breeding group until the resulting population of offspring, denoted as Q_t, achieves the desired population size N. Subsequently, update $P_{t+1} = Q_t$.

Step 5: Update t to $t + 1$ and return to Step 2.

3.3.1 Performing Multi-Objective Optimisation using Matlab

Multiobjective optimization is a vital area of research and application, where multiple conflicting objectives need to be optimized simultaneously. In MATLAB, the gamultiobj function found in the Global Optimization Toolbox stands out as a powerful tool for tackling complex problems. The gamultiobj function is useful in situations where conventional optimization methods struggle, such as with objective functions that are nonlinear, non-differentiable or contain discontinuities. It uses genetic algorithms to determine a set of Pareto-optimal results that balance the trade-offs among the objectives.

The mathematical formulation of the gamultiobj tool can be performed by utilizing the following script in MATLAB. The optimization process primarily involved the imposition of constraints on lower and upper bounds, with default settings for population size, maximum generations, and tolerance [98].

$$Objective : \begin{cases} f_1 = \quad \text{fn}(x_1, x_2, x_3, ..., x_n) \\ f_2 = \quad \text{fn}(x_1, x_2, x_3, ..., x_n) \end{cases} \tag{3.32}$$

Find:

$$fn = min(f_1, f_2) \tag{3.33}$$

$$
ProblemScript: \begin{cases}
\text{*** Objective Function Definition ***} \\
FunctionOutput = Minimisation(Input); \\
x() = Input; \\
f_1 = (); \\
f_2 = (); \\
Output = (); \\
\\
\text{*** Main Program Script ***} \\
A = []; b = [] \\
Aeq = []; beq = [] \\
LowerBound = []; \\
UpperBound = []; \\
PopulationSizeData = []; \\
MaxGenerationsData = []; \\
ToleranceData = []; \\
x = gamultiobj(FitnessFunction, nvars, A, b, Aeq, beq, lb, ub)
\end{cases} \tag{3.34}
$$

A Pareto front is analyzed to extract optimal data from the output that does not affect the parameters dominantly. To accomplish this objective, an individual x_i at generation t, dominated by $\pi(t)$ individuals in the current population, is considered the default. Its current position in the individuals' rank can be determined by following Equation, where all the non-dominating values are assigned the value of unity, as depicted in Figure 5.

$$rank(x_i, t) = 1 + pi^t \tag{3.35}$$

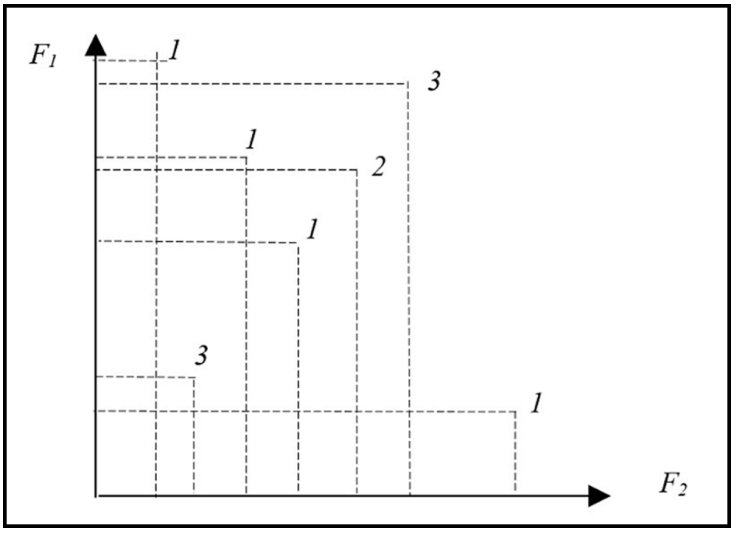

FIGURE 3.7: Pareto rank chart[98].

Subsequently, the procedure mentioned in Figure 5 is integrated into the code utilizing the plot functions available in MATLAB. The following demonstration executes this integration.

$$\begin{cases} \text{options} = \text{optimoptions(@gamultiobj,PlotFcn,[ ],[ ]);} \\ \text{gamultiobj(FitnessFunction,numberofvariables,[ ],[ ],[ ],[ ],lb,ub,options);} \end{cases} \tag{3.36}$$

3.4 CFD Theoretical Background

The fundamental concepts of fluid dynamics are based on three essential equations: conservation of mass, momentum, and energy. These equations are vital in describing fluid movement across various contexts, from the aerodynamics of vehicles to the circulatory transfer of blood in the human body. In this research, fluid flow over an airfoil was set as 0.45, indicating the need for compressible flow analysis to model the relevant physical phenomena accurately. For compressible flow situations, the fluid's density is influenced by variations in pressure and temperature. The energy equation is vital for considering changes in the fluid's energy, notably thermal energy, which directly affects the fluid's density. By resolving the energy equation, it's possible to precisely

track temperature fluctuations and their effects on density, thus achieving realistic and reliable simulations. The governing equations are as follows:

Continuity Equation:

$$\frac{\partial \rho}{\partial t} + \left(\frac{\partial (\rho u)}{\partial x} + \frac{\partial (\rho v)}{\partial y} + \frac{\partial (\rho w)}{\partial z} \right) = 0 \tag{3.37}$$

Momentum Equation (x-direction):

$$\begin{aligned} \frac{\partial (\rho u)}{\partial t} + \left(\frac{\partial (\rho u^2)}{\partial x} + \frac{\partial (\rho uv)}{\partial y} + \frac{\partial (\rho uw)}{\partial z} \right) &= -\frac{\partial p}{\partial x} \\ + \left[\frac{\partial}{\partial x} \left(\lambda (\nabla \cdot \mathbf{V}) + 2\mu \frac{\partial u}{\partial x} \right) + \frac{\partial}{\partial y} \left(\mu \left(\frac{\partial v}{\partial x} + \frac{\partial u}{\partial y} \right) \right) \right. & \\ \left. + \frac{\partial}{\partial z} \left(\mu \left(\frac{\partial u}{\partial z} + \frac{\partial w}{\partial x} \right) \right) \right] + \rho f_x & \end{aligned} \tag{3.38}$$

Energy Equation:

$$\begin{aligned} \rho \frac{D}{Dt} \left(e + \frac{V^2}{2} \right) = \rho \dot{q} + \frac{\partial}{\partial x} \left(k \frac{\partial T}{\partial x} \right) + \frac{\partial}{\partial y} \left(k \frac{\partial T}{\partial y} \right) + \frac{\partial}{\partial z} \left(k \frac{\partial T}{\partial z} \right) & \\ - \frac{\partial (up)}{\partial x} - \frac{\partial (vp)}{\partial y} - \frac{\partial (wp)}{\partial z} & \\ + \frac{\partial (u\tau_{xx})}{\partial x} + \frac{\partial (u\tau_{yx})}{\partial y} + \frac{\partial (u\tau_{zx})}{\partial z} & \\ + \frac{\partial (v\tau_{xy})}{\partial x} + \frac{\partial (v\tau_{yy})}{\partial y} + \frac{\partial (u\tau_{zy})}{\partial z} & \\ + \frac{\partial (w\tau_{xz})}{\partial x} + \frac{\partial (w\tau_{yz})}{\partial y} + \frac{\partial (w\tau_{zz})}{\partial z} & \\ + \rho \mathbf{f} \cdot \mathbf{V} & \end{aligned} \tag{3.39}$$

This study uses the transient Reynolds-Averaged Navier–Stokes (RANS) equations to determine the aerodynamic performance of Eppler airfoil [99]. The turbulence modeling approach uses the standard k–ω model, where k represents turbulent kinetic energy governing turbulence energy, and ω denotes specific turbulent dissipation rate governing the rate of dissipation per unit turbulent kinetic energy. The standard k–ω model is

widely implemented in mainstream Computational Fluid Dynamics (CFD) packages and is recognized as the industry standard for its robustness and numerical stability [100].

The Wilcox $k-\omega$ model was utilized for its effective integration of a robust and accurate formulation in the near-wall region. The transient transport equations governing the $k-\omega$ model are as follows:

$$\frac{\partial}{\partial t}(\rho k) + \frac{\partial}{\partial x_i}(\rho k v_i) = \frac{\partial}{\partial x_j}\left(\Gamma_k \frac{\partial k}{\partial x_j}\right) + G_k - Y_k + S_k \tag{3.40}$$

$$\frac{\partial}{\partial t}(\rho \omega) + \frac{\partial}{\partial x_i}(\rho k v_i) = \frac{\partial}{\partial x_j}\left(\Gamma_\omega \frac{\partial \omega}{\partial x_j}\right) + G_\omega - Y_\omega + D_\omega + S_k \tag{3.41}$$

In the above-mentioned equations, G_k denotes turbulence kinetic energy generation from mean velocity gradients and G_ω denotes the generation of ω. Γ_k and Γ_ω represent the effective diffusivity of k and ω, respectively. Y_k and Y_ω indicate turbulence-induced dissipation k and ω. Additionally, S_k and S_ω denote user-defined source terms.

3.5 Airfoil selection for morphing applications

In the aerospace engineering sector, airfoils play a crucial part in theoretical research and real-world applications. The initial designs of airfoil sections used in aviation were developed and patented by Horatio Phillips in the 1880s [101]. These pioneer airfoil shapes, depicted in Figure 3.8, were based on the bird's wings in different flight stages.

Over time, our grasp of airfoil shapes has grown more nuanced and advanced, resulting in the recognition of different airfoil designs. The NACA Algorithm is a widely recognized method for characterizing airfoil shapes. Figure 3.9 demonstrates the typical variables that can be assigned to define the shape of an airfoil [101].

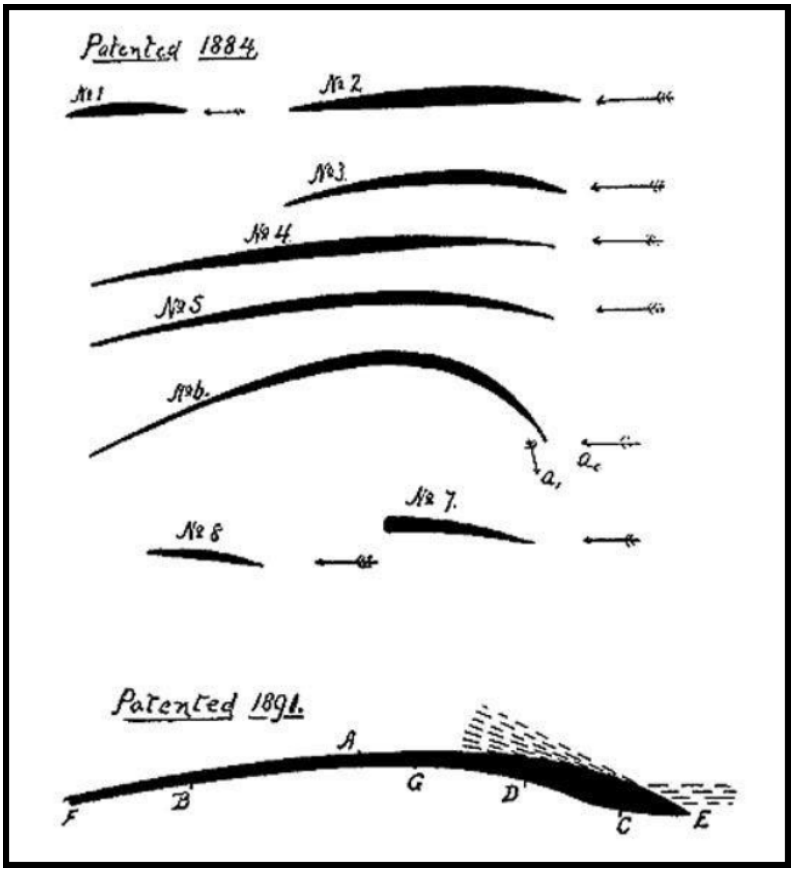

FIGURE 3.8: Pioneer airfoil shapes developed by Horatio Phillips [101].

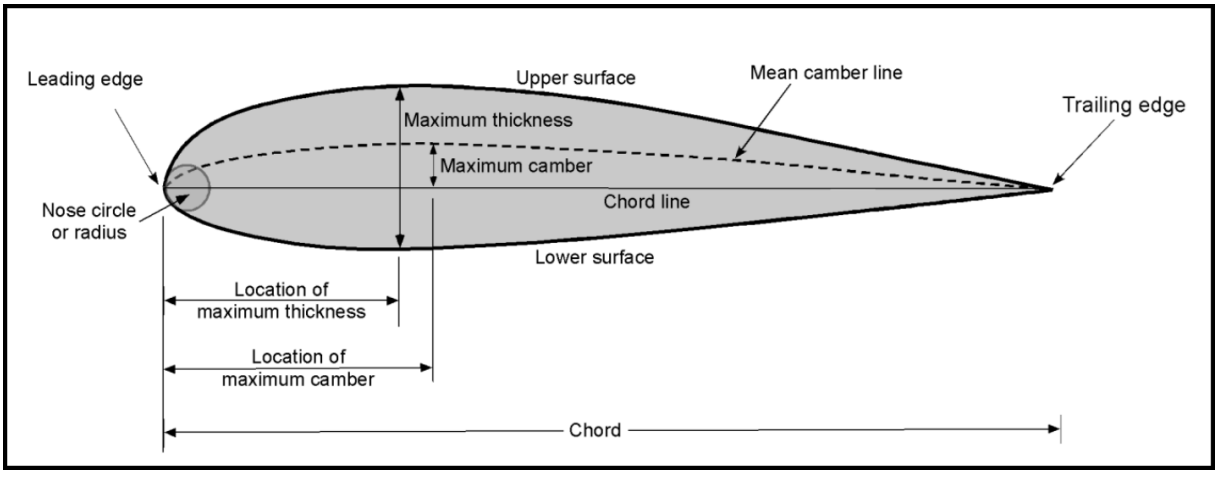

FIGURE 3.9: Key geometric variables to define an airfoils shape [101].

Figure 3.9 depicts an airfoil with a positive camber, highlighting it as one of the main three types of airfoils. The remaining categories encompass the symmetric airfoil, noted for its camber line and chord line being identical in both position and length, as well as the reflex cambered airfoil. The latter is often utilized in aircraft wings and helicopters,

distinguished by its positive camber close to the leading edge and a negative camber towards the trailing edge. Cambered airfoils, particularly the Eppler 420 and Eppler 423, are frequently recommended for their substantial camber, contributing to a favorable lift-to-drag ratio. The comparative tests have shown that the Eppler 420 outperforms the Eppler 423, generating higher lift and lower drag. Consequently, the selected Eppler 420 airfoil for this research is shown in Figure 3.10.

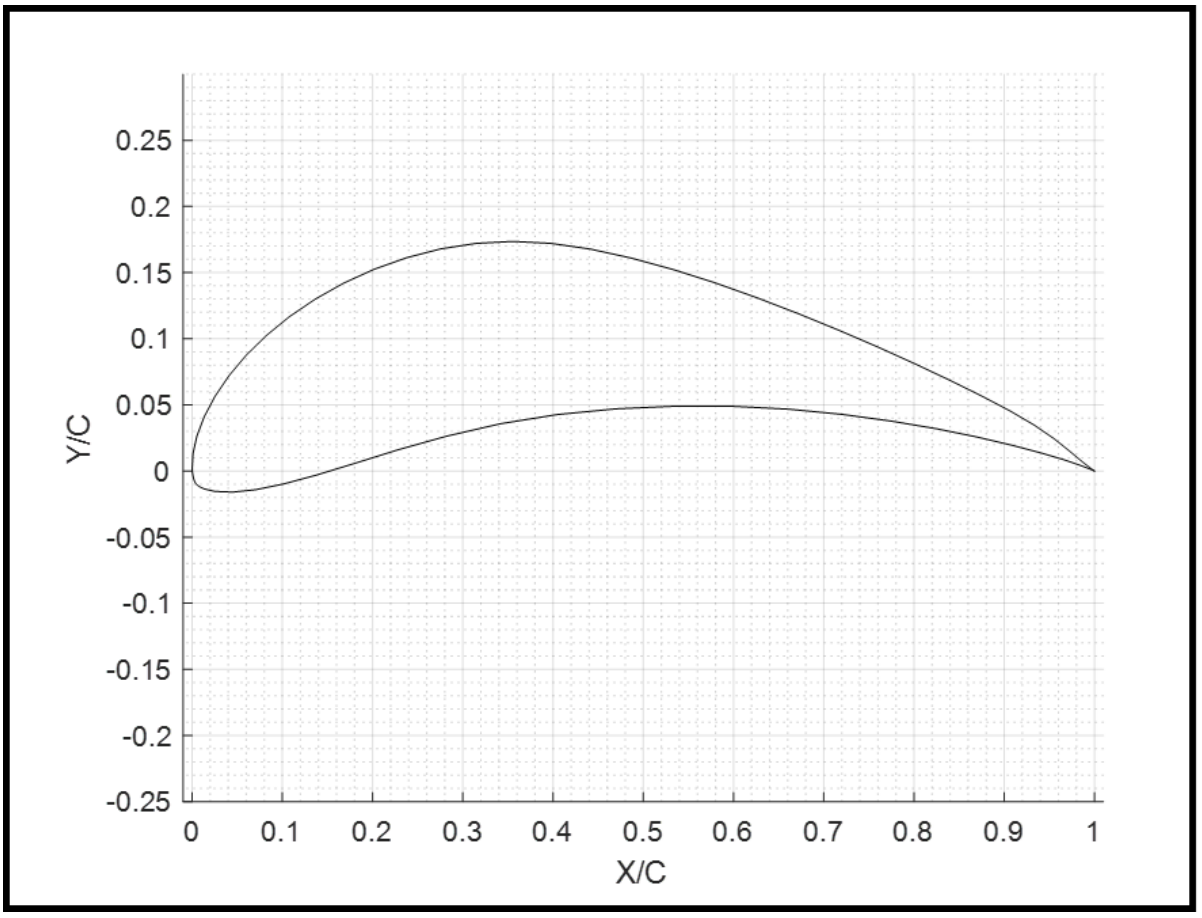

FIGURE 3.10: Selected Eppler 420 airfoil profile.

3.6 Computer Aided Design (CAD) of 3D Airfoil featuring different Auxetic Cores

When it comes to designing compliant cellular structures, it becomes mandatory to balance the conflicting requirements of stiffness and flexibility. This section focuses on developing different cellular auxetic structures to be embedded into the airfoil's core to boost the morphing performance in terms of trailing edge deflection. Each auxetic structure designed has the same effective stiffness under aerostatic loading.

Since the in-plane shear strain is discovered to be the primary deformation mechanism in the compliant auxetic structures, the auxetic configurations are engineered to possess the same shear modulus to determine which cellular structure exhibits better-trailing edge deflection. Three types of cellular structures are examined for the core layout in this study: chiral honeycomb, regular hexagonal honeycomb, and re-entrant hexagonal honeycomb. The leading edge displacements of airfoils with different auxetic cores are compared, and the peak permissible strains are analyzed by examining the local stresses in the constituent material.

Additionally, from the comparative FEA analysis of airfoils with different auxetic cores discussed in the next chapter, it was concluded that the re-entrant structure exhibits superior morphing performance in terms of both deflection and stiffness compared to other structures. Based on this finding, a particular emphasis was placed on designing a novel reentrant cell with optimal geometric dimensions to maximize the negative Poisson's ratio and enhance elastic stiffness.

Consequently, four distinct auxetic structures have been engineered for their incorporation into the core of the airfoil. SolidWorks 2020 was employed to design the respective CAD geometries in this regard. The cellular unit cell configurations, alongside their geometrical parameters, are illustrated in Figure 3.11. The values considered for the geometrical

specifications for all the unit configurations are highlighted in Table 3.1. Additionally, a detailed procedure to design an airfoil containing an auxetic core is displayed in Figure 3.12.

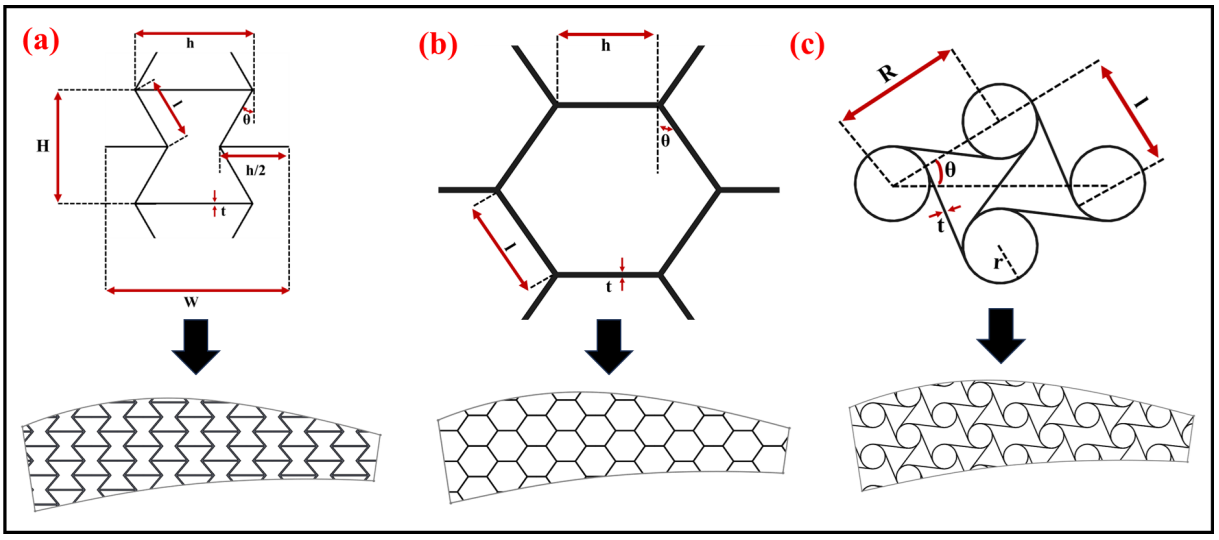

FIGURE 3.11: Representation of unit cell configuration and their respective cores (a) reentrant hexagonal honeycomb, (b) regular hexagonal honeycomb, and (c) chiral honeycomb

TABLE 3.1: Selected geometrical parameters for different auxetic unit cell configurations.

Type	R (mm)	L (mm)	r (mm)	t (mm)
Chiral	45	37	13.5	0.30

Type	h (mm)	l (mm)	θ (degree)	t (mm)
Standard honeycomb	20.455	20.014	34.9917	1
Reentrant honeycomb	40.0192	20.0157	-40.0198	1.6413
Optimal Reentrant honeycomb	43.64	18.62	-45.821	1.5495

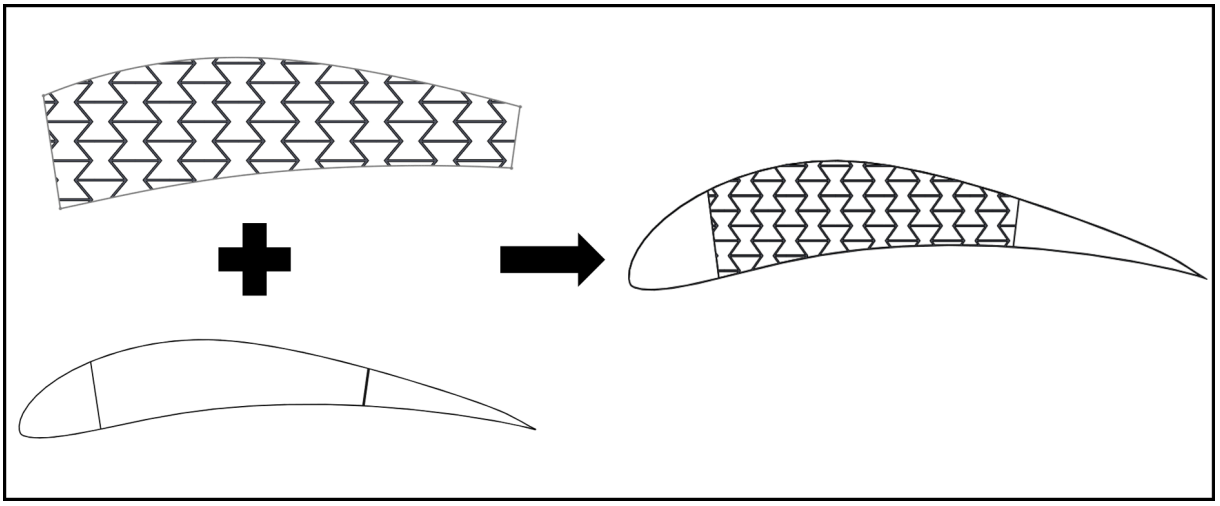

FIGURE 3.12: The process undertaken to design airfoil integrating the cellular core.

The geometrical configuration of the Eppler 420 airfoil integrating cellular core, as described in Figure 3.13, was based on the work of Heo & Kim [102]. The geometric parameters of the airfoil are as follows: chord dimension $c = 700$ mm, angles $\alpha = 8.58°$ and $\beta = 8.0°$, frontal and rear edge lengths $a = 110$ mm and $b = 235$ mm, surface thickness $t = 1$ mm, out-of-plane depth (along z-axis) $t_z = 19$ mm, and the trailing-edge thickness $t_D = 15.4$ mm. The finalized CAD models of the Eppler 420 airfoil featuring regular hexagonal, reentrant honeycomb, optimized reentrant honeycomb, and chiral honeycomb structures are presented in Figure 3.14.

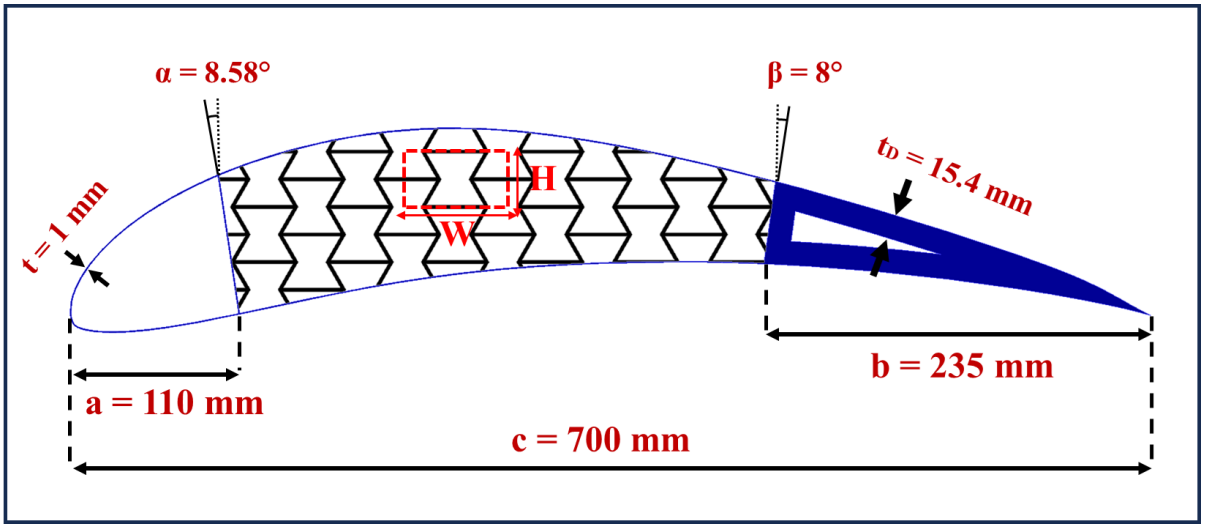

FIGURE 3.13: The Eppler 420 airfoil arrangement is integrated with an auxetic core

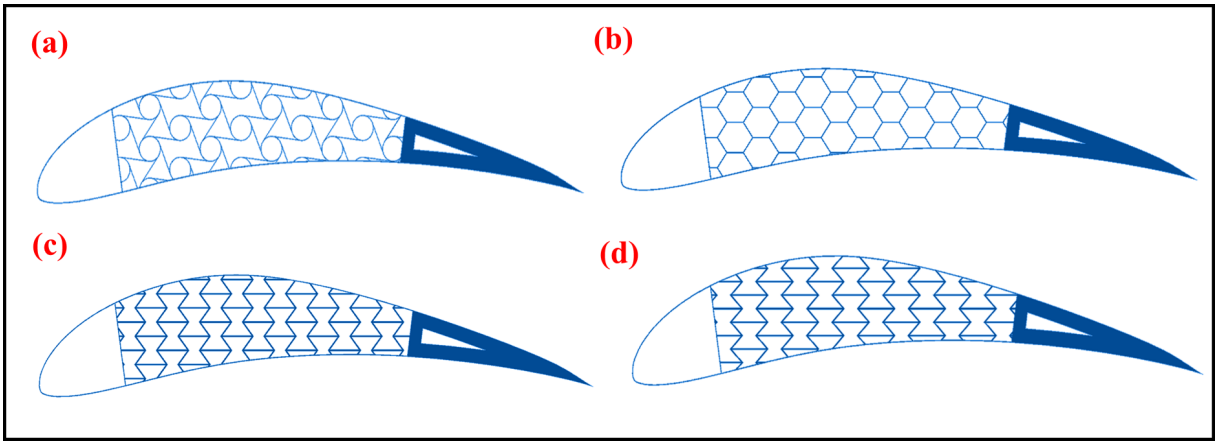

FIGURE 3.14: Representation of Eppler 420 airfoil featuring auxetic core arrangement (a) chiral honeycomb, (b) regular hexagonal honeycomb, (c) reentrant honeycomb, and (d) optimal reentrant honeycomb.

While auxetic structures are commonly associated with metals or alloys, their utilization extends beyond composites and polymers. Aluminium alloy 6061 with specified properties, as documented in Table 3.2, has been chosen for the research. Alloy 6061 is widely utilized when establishing a favorable balance between strength and weight, which is vital, notably in aerospace applications. The alloy 6061 T6 variant boasts superior machinability characteristics, an enhanced response to anodizing, and comparable corrosion resistance properties.

TABLE 3.2: Mechanical properties of aluminium alloy 6061.

Properties	**Values**	**Units**
Density (ρ)	2771	kg/m^3
Young's Modulus (E)	71000	MPa
Poisson's Ratio (ν)	0.33	–
Yield Strength (σ_{y_t})	280	MPa
Ultimate Strength (σ_{ut})	310	MPa

3.7 Finite Element Modelling

Finite Element Modelling (FEM) was performed using ANSYS Mechanical software packages. ANSYS static structural module within the ANSYS software collection provides tools for evaluating structural designs through steady-state linear and steady-state non-linear analyses.

The airfoil design, which incorporates auxetic mesostructures, was loaded into ANSYS to examine the deflection of the trailing edge and assess its structural durability against aerostatic loading conditions. The static structural analysis feature was deployed to quantify the trailing edge deformation, aiming to measure the efficacy of its morphing capabilities. The algorithm developed to simulate the deformation behavior of the Eppler airfoil integrating auxetic core is presented in Figure 3.15.

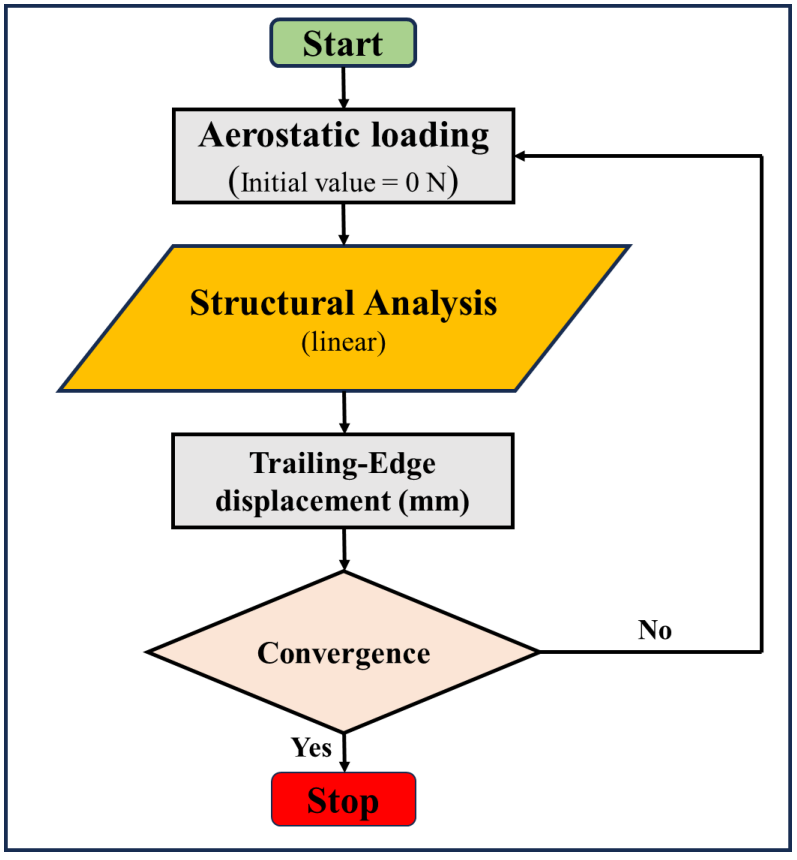

FIGURE 3.15: The flowchart represents the algorithm adopted to conduct the static 3D aeroelastic analysis.

The FEA analysis typically involves three stages: pre-processing, solving, and post-processing. The initial stage, the pre-processing stage, primarily involves clearing geometrical defects and meshing. The default tetrahedral mesh element size was utilized to reduce computational time and cost to carry out the simulations. The next phase involves the assignment of materials and the application of necessary boundary constraints. An aluminium alloy with standard material properties based on the ANSYS material library was selected for analysis. Figure 3.16 illustrates the boundary constraints applied: the frontal edges were clamped (fixed), and an axial load (F) was imposed on the region near the trailing edge, causing deformation in the loading direction. The last stage of post-processing involves analyzing and visualizing the results obtained from the FEA simulations, which are detailed in the next chapter.

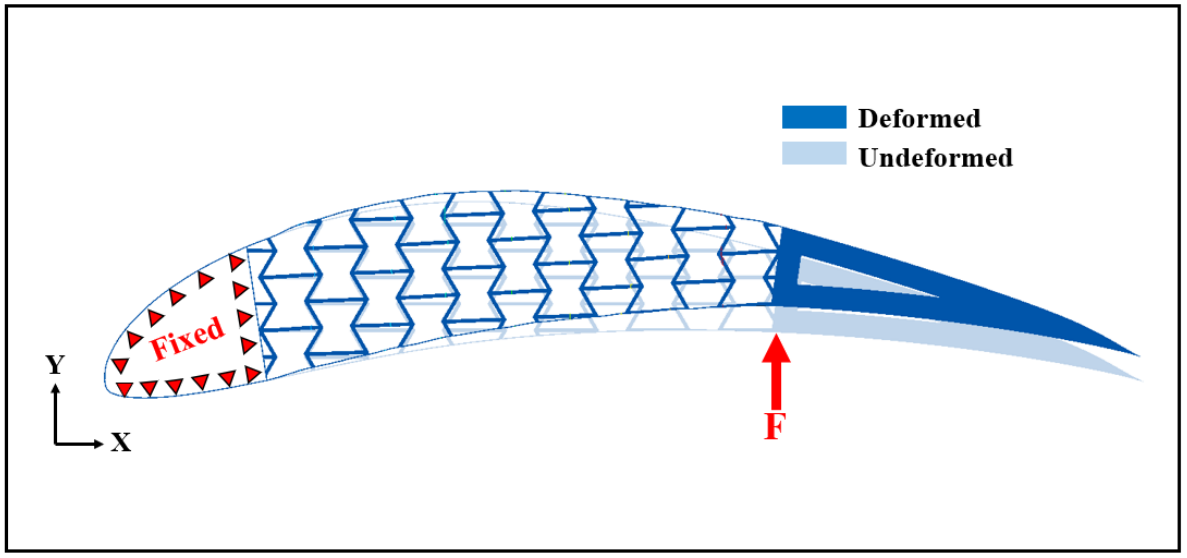

FIGURE 3.16: Assigned boundary constraints to determine trailing edge deflection under unidirectional aerostatic loading.

3.8 Computational Fluid Dynamics (CFD) Modelling

Accurately determining the c_l and c_d (coefficients of lift and drag) is crucial for the design of aircraft and other aerial vehicles. In recent years, numerical approaches have gained

significant attraction due to experimental methods' expense and limited applicability. The reduced cost, increased speed, and capability to accurately model complex geometries and operational conditions render computational simulations highly suitable for aerodynamic analysis. Following the practice adopted by many research scientists and organizations, including NASA, the ANSYS Fluent software is utilized for aerodynamic calculations [103, 104].

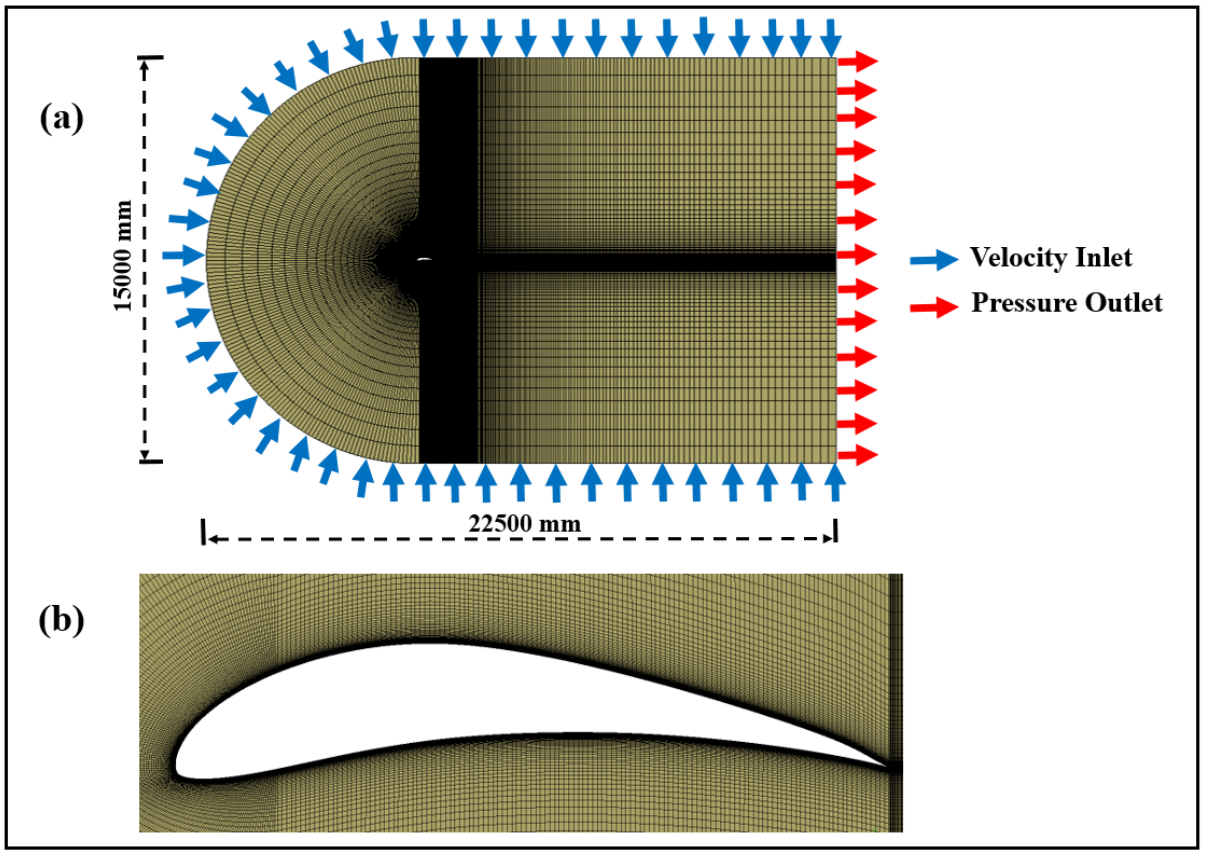

FIGURE 3.17: (a) Meshed fluid domain with structured grids and boundary constraints, (b) Close-up view of structured mesh near airfoil regions.

A two-dimensional (C-type) flow field is constructed with a horizontal distance of 22,500 mm (32c) and a vertical distance of 15,000 mm (21.4c), as illustrated in Figure 3.17. To accurately capture the fluid behavior at the fluid-solid interface, a structured mesh with a y^+ value of 1 was utilized for discretizing the fluid domain. The generated mesh network for the fluid domain, using the ANSYS Fluent meshing tool is shown in Figure 3.17. A finer mesh density is used adjacent to the airfoil to capture fluid behavior around the

airfoil. The mesh density is relaxed in regions further from the airfoil, where the fluid does not directly induce deformation effects on the airfoil.

Initially, 2D CFD simulations using ANSYS Fluent were executed to validate and assess the impact on aerodynamic coefficients at various angles of attack for NACA 0012 and NACA 2412 airfoils across different Reynolds numbers. Later, the same physics was extended and applied to perform a decoupled fluid structural analysis of the Eppler 420 airfoil integrating cellular core to determine aerodynamic coefficients and maximum trailing edge deflection at different Reynolds numbers.

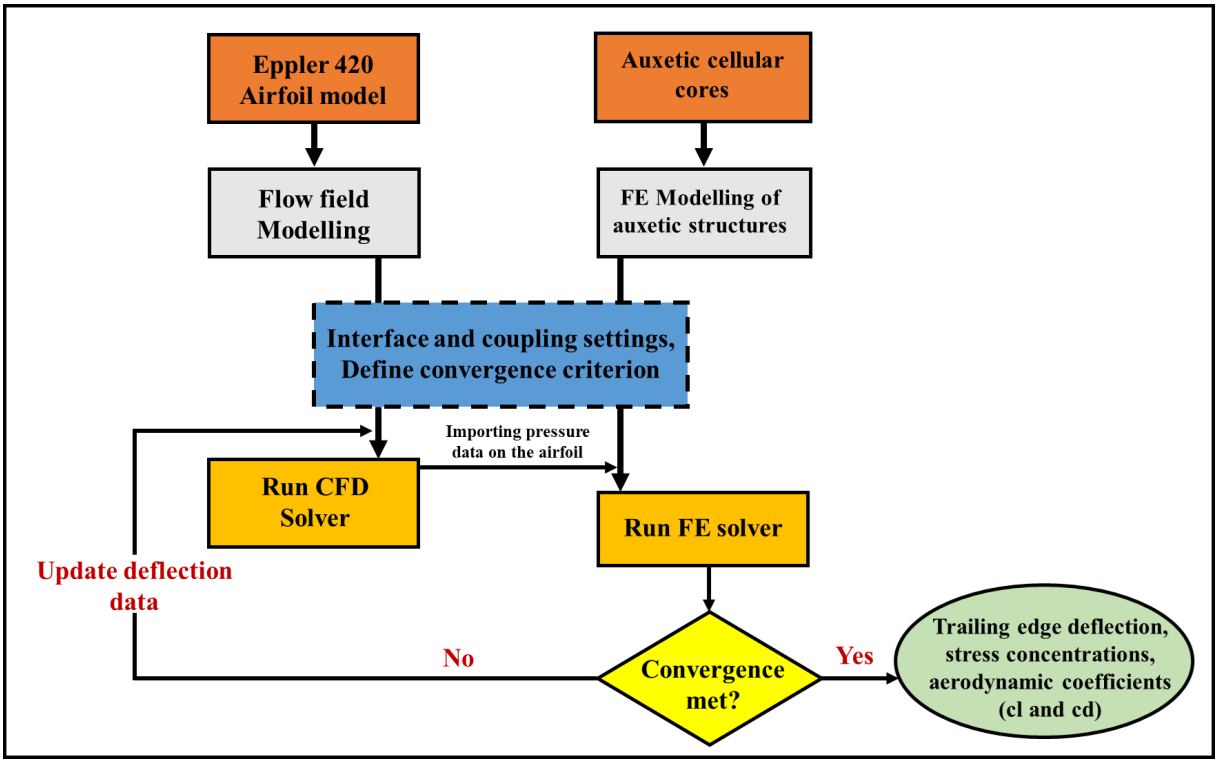

FIGURE 3.18: Flowchart illustrating the algorithm used for one-way coupled fluid-structural analysis.

A one-way coupling of fluid-structural analysis is used to evaluate the maximum trailing edge deflection, optimizing computational efficiency and reducing simulation runtime. The algorithm developed to carry out decoupled fluid structural analysis is outlined in Figure 3.18. The algorithm begins by creating a two-dimensional domain to simulate fluid flow behavior, measuring aerodynamic forces and pressure distribution over the airfoil. The

next stage involves generating the mid-surface model of the Eppler airfoil with an auxetic core, import pressure loading, and calculating the trailing edge deflection utilizing the Static Structural module.

Table 3.3: Computational conditions to conduct airfoil simulations.

Parameter	**Value**
Analysis Type	Transient
Viscous Model	SST $k-\omega$
Fluid Material	Air Density - 1.225 kg/m^3 Viscosity - 1.7894e-05 $kg/m.s$
Boundary Condition	Inlet: Velocity - Mach no.: 0.25,0.45 Temperature - 288.16 k Outlet: Gauge Pressure - 0 Pa Airfoil: Wall
Solution Methods	Scheme: Coupled Scheme: Flux Type: Rhie-Chow - distance based Gradient: Least Squares Cell Based Presure: Second Order Momentum: Second Order Upwind Turbulent Kinetic Energy: Second Order Upwind Turbulent Dissipation Rate: Second Order Upwind
Residual Criterion	continuity: 1e-06 x-velocity: 1e-06 y-velocity: 1e-06 k: 1e-06 ω: 1e-06
Initialisation	Hybrid
Iterations	10000

The inlet velocities of the fluid field were set to Mach 0.25 and 0.45, with AoA varying from 0° to 14° with increments of 4°. The analysis uses air as the fluid with standard properties. The pressure within the fluid zone is adjusted to 1 atm, and the outlet pressure is maintained at 0 Pa gauge pressure. The airfoil profile and the flow field interface are designed as a no-slip wall, with an adiabatic wall boundary condition assigned to the airfoil surface. Gravitational force and other body forces are not considered, and the internal frame of the reference region is assumed to be stationary. The performance and fluid behavior analysis of the Eppler 420 airfoil were conducted using Ansys Fluent based on the computational conditions outlined in Table 3.3.

Chapter 4

Results and Discussion

4.1 Introduction

In this chapter, the section 4.2 begins with a parametric investigation of the reentrant honeycomb unit cell configuration utilizing the analytical relationships formulated by Hedayati and his colleagues to understand the effects of parameter variation on in-plane mechanical properties. Section 4.3 presents the strategy to develop a novel reentrant hexagonal honeycomb configuration with optimal parameters targeting enhancing elastic modulus and maximum negative Poisson's ratio. Section 4.4 provides a detailed FEA analysis of the Eppler 420 airfoil integrated with different auxetic cores under uniaxial aerostatic loading. Similarly, section 4.5 provides CFD decoupled fluid structural results for the differently designed airfoil models at various Reynolds numbers to account for the variations in the flow angle of attack.

4.2 Parametric Analysis Results

The parametric investigation examines the effects of varying reentrant honeycomb geometrical parameters, focusing on the mechanical properties, including the Elastic Modulus and Poisson's Ratio. Montgomery and colleagues modified the analytical expressions by prior authors to determine in-plane elastic moduli, and Poissons's ratio was utilized with the same symbols and dimensional parameters for a reentrant unit cell. This was accomplished to facilitate a comparative study of the various mathematical formulas proposed by different research groups. This strategy maintains methodological coherence and promotes the interpretability of other researchers' comparative findings.

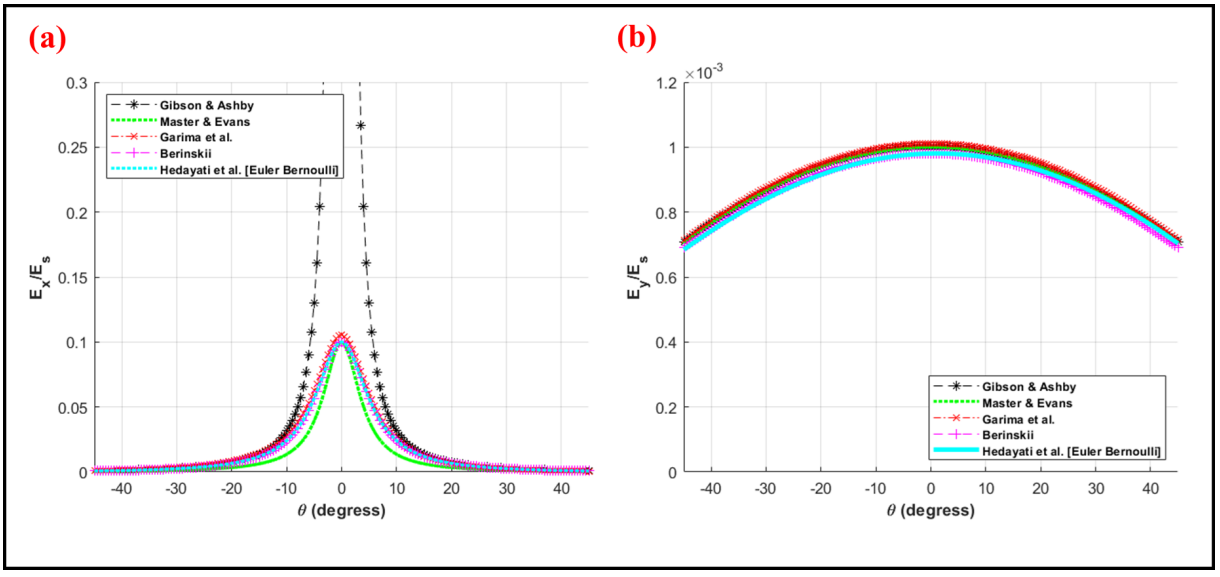

FIGURE 4.1: Parametric assessment of the in-plane relative elastic moduli (a) E_x/E_s and (b) E_y/E_s with variable θ proposed by different authors for analyzing reentrant auxetic configurations.

The chosen geometric unit cell has dimensions of W*H = 1*1 unit length, featuring a wall depth thickness of d = 0.5 unit lengths and a consistent thickness of t = 0.05. The material selected for this structure is an aluminum alloy with an elastic modulus of 71000 MPa and a Poisson's ratio of 0.33. Given that the angle between the struts chiefly governs the auxetic attributes of the reentrant structure, the parametric investigation focuses on assessing the effects of varying this angle from -45° to 45° on elastic moduli and Poisson's

ratio using a MATLAB Script [105]. The mechanical properties, namely in-plane elastic moduli, and Poisson's ratio are plotted using the above-mentioned geometric constraints, and the obtained respective graphs are presented in Figures 4.1 and 4.2.

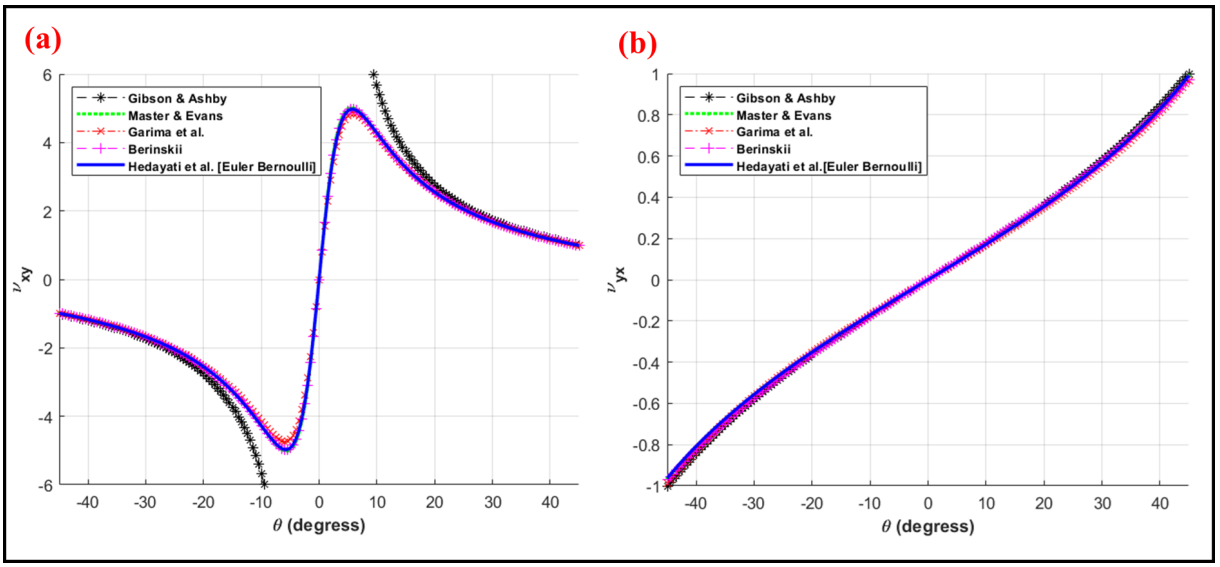

FIGURE 4.2: Parametric assessment of the Poisson's ratios (a) ν_{12} and (b) ν_{21} with variable θ proposed by different authors for analyzing reentrant auxetic configurations.

Figure 4.2 exhibits the plotted Poisson's ratio ν_{yx} curves showing complete overlap among analytical formulations by diverse authors. However, for ν_{xy}, the depicted curves indicate an analogous pattern except for formulations of Gibsons and Ashby. The ν_{xy} curve tends towards infinity at θ equals 0 degrees. The primary reason behind this deviation in literature is that the author only considered bending as a deformation mechanism of reentrant honeycombs and neglected another critical phenomenon, such as hinging and stretching. In Figure 4.1, following the Gibson formulation, the relative elastic moduli along x-axis exhibits asymptotic variation. Conversely, formulations suggested by other authors for E_x and E_y show close agreement for various theta values.

4.3 Multi-Objective Optimisation Results

This section delves into utilizing a genetic algorithm for parametric optimization to strengthen the robustness of the re-entrant configuration. The emphasis is placed on optimizing geometrical factors to attain superior mechanical properties. The optimization task involves efficiently addressing two objective functions, utilizing a single-objective optimization approach. To achieve this, both functions are combined into a single multi-objective function.

Optimization is executed using the multi-objective genetic algorithm, particularly the gamultiobj toolbox, implemented in MATLAB. Simultaneously, two critical objective functions are pursued for the multi-objective optimization of auxetic structures. Using MATLAB's gamultiobj tool, the geometrical dimensions of the unit configuration are optimized using a Genetic Algorithm approach. This process involves developing a comprehensive function considering their respective domains' objectives, constraints, and design parameters.

The gamultiobj tool aims to minimize the objective function, so it is crucial to define the objectives clearly to obtain accurate results. The primary aim is to attain a minimal negative Poisson's ratio and a maximum elastic modulus for the unit cell. This requires minimizing the negative modulus to maximize the objective and minimizing the Poisson's ratio below the null limit of 0. The Euler-Bernoulli beam theory formulations (derived by Hedayati *et al.*) E_x and ν_{xy} are selected as the objective functions for optimization. The baseline parameters are based on the reference by Heo and Kim, with the upper and lower bounds set by varying the baseline by 15% for the geometric parameters. The chosen goal function and geometrical constraints for optimizing are outlined as follows:

$$Objective: \begin{cases} Maximise\, E = & \text{fn(W,H,t,}\theta\text{)} \\ Minimise\, \nu = & \text{fn(W,H,t,}\theta\text{)} \end{cases}$$

Find:

$$\text{fn} = \min\ (E_x, \nu_{xy})$$

$$E_x = \frac{-\sigma}{E}$$

$$\nu_{xy} = \frac{-\epsilon_y}{\epsilon_x}$$

$$Subjected\ to: \begin{cases} 41.516 \leq \text{W} \leq 62.440 \\ 27.453 \leq \text{H} \leq 37.825 \\ 1.395 \leq \text{t} \leq 1.8874 \\ -46 \leq \theta \leq -34 \end{cases}$$

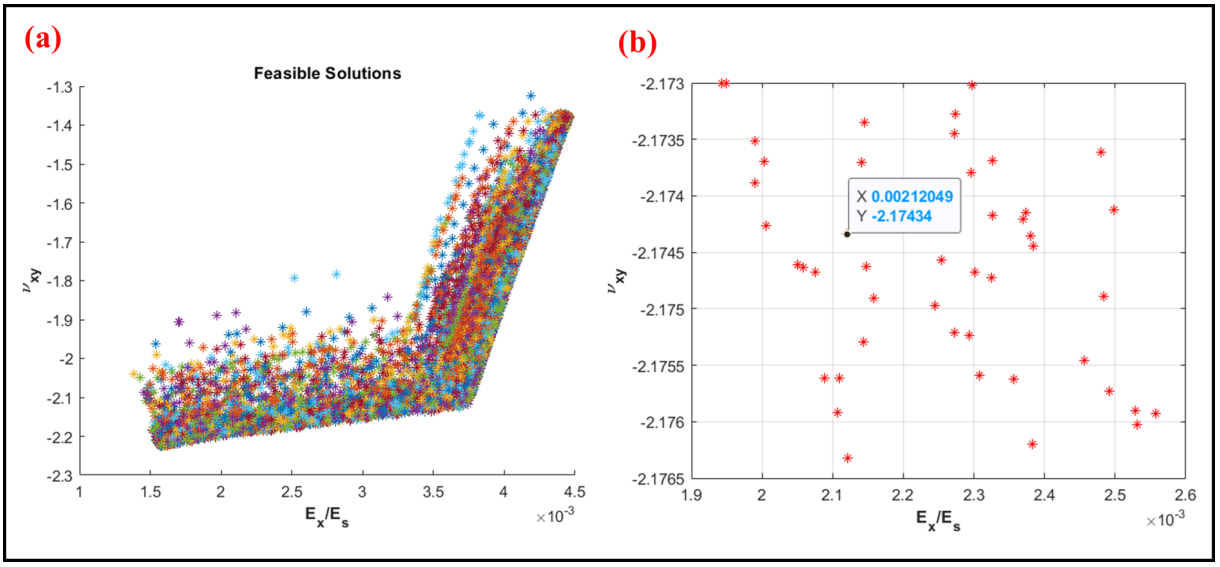

FIGURE 4.3: (a) Pareto front illustrating feasible solutions with optimized objective functions including Poisson's ratio ν_{xy} and relative Elastic moduli E_x/E_s. (b) The selected optimal point represents the best values for the objective functions.

The gamultiobj solver generated roughly 4700 possible solutions, with the Poisson's ratio extending from -2.3 to -1.3 and the relative elastic moduli ranging from 0.0015 to 0.0045, as depicted in Figure 4.3. The goal of optimization was to develop a structure that minimizes the negative poison's ratio while demonstrating a high relative modulus.

To identify the optimal reentrant configuration, the targeted ranges for Poisson's ratio and relative modulus are adjusted to -2.1765 to -2.173 and 0.0019 to 0.0026, respectively. The selected optimal point for designing a novel optimized reentrant honeycomb configuration is highlighted in Figure 4.3(b). In addition, Table 4.1 documents the baseline and optimized parameters for the reentrant structure obtained alongside the objective functions. Multi-objective optimization using gamultiobj solver resulted in a significant 54.65% improvement in Poisson's ratio and a significant 37.5% increase in the relative elastic modulus, as determined analytically.

TABLE 4.1: Outcomes of the objective functions employing both baseline and optimized geometrical parameters of reentrant auxetic structures.

Parameters	**W (mm)**	**H (mm)**	**t (mm)**	$\boldsymbol{\theta}$ (degrees)	$\boldsymbol{E_x/E_s}$	$\boldsymbol{\nu_{xy}}$
Baseline	54.296	30.656	1.6413	-40.0198	-1.4061	0.0016
Optimised	62.344	27.584	1.5626	-45.889	**-2.1746**	**0.002147**

4.4 FEA Simulation Results under Aerostatic Load

This section commences with the comparative FEA results of the Eppler 420 airfoil featuring chiral honeycomb, hexagonal honeycomb, and reentrant honeycomb configurations. The goal is to determine the most desirable auxetic configuration that enhances wing morphing capabilities. An FEA study was performed with uniaxial loading boundary conditions to verify the superior auxetic configuration for wing morphing among the three discussed designs. This approach ensures the stress generated remains within the elastic limit of the constituent material assigned to the 3D airfoil

model, thereby preventing any non-linear deformations. The three unique loads designed for distinct auxetic configurations are applied to achieve identical resultant stress and factor of safety (FOS) for each model.

The axial or aerostatic load is applied close to the edge of the compliant core as a localized force in incremental steps, starting with an initial load of 10 N and then incremented by 10 N up to the maximum possible material elastic limit achieved for the respective models. The maximum loads applied for the Eppler 420 airfoil integrating chiral honeycomb, hexagonal honeycomb, and reentrant honeycomb configurations are 107 N, 250 N, and 475 N, respectively.

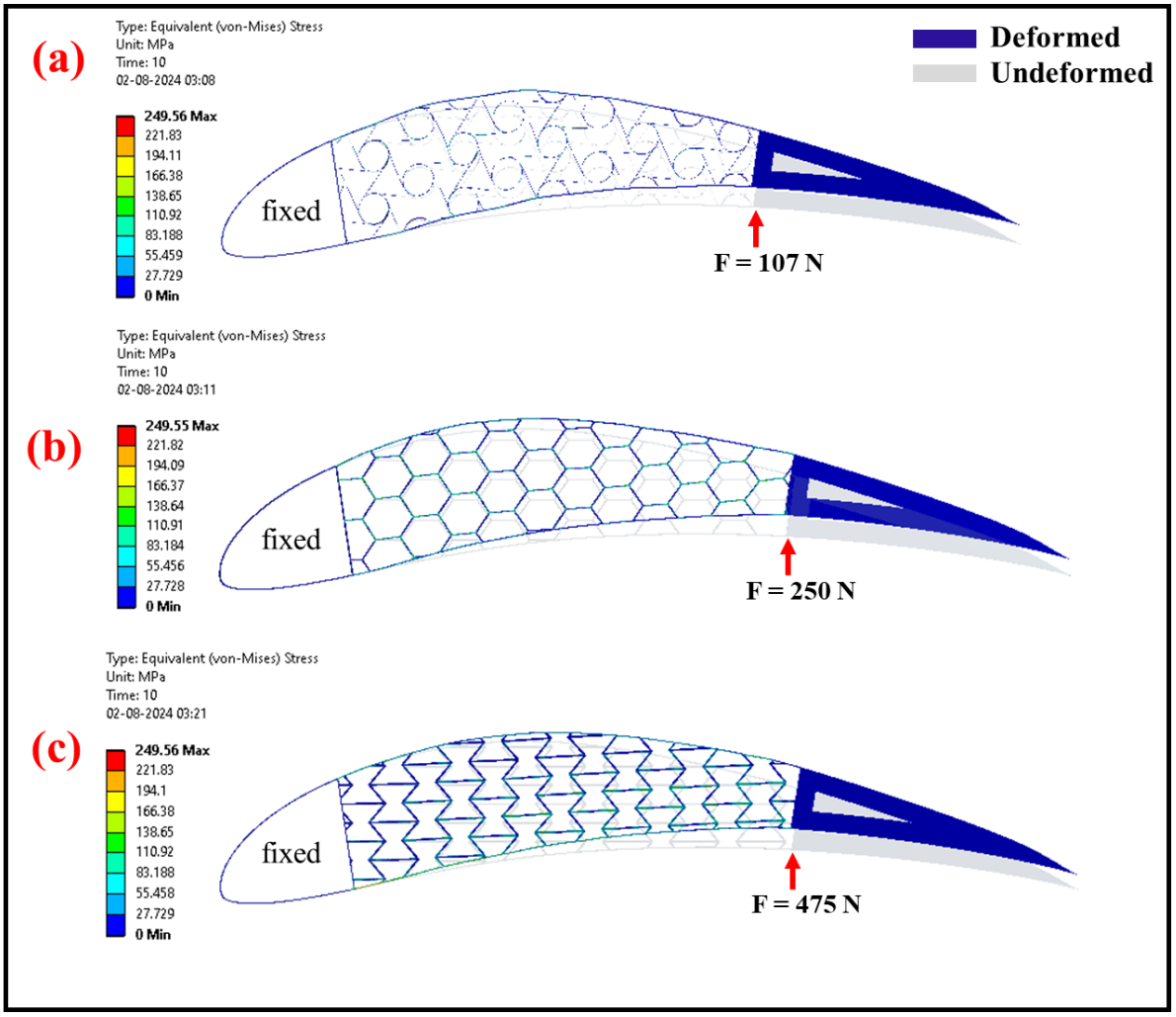

FIGURE 4.4: Von-Mises Stress contours at distinct loads for Eppler 420 airfoil featuring (a) chiral honeycomb core, (b) hexagonal honeycomb core, and (c)reentrant honeycomb core.

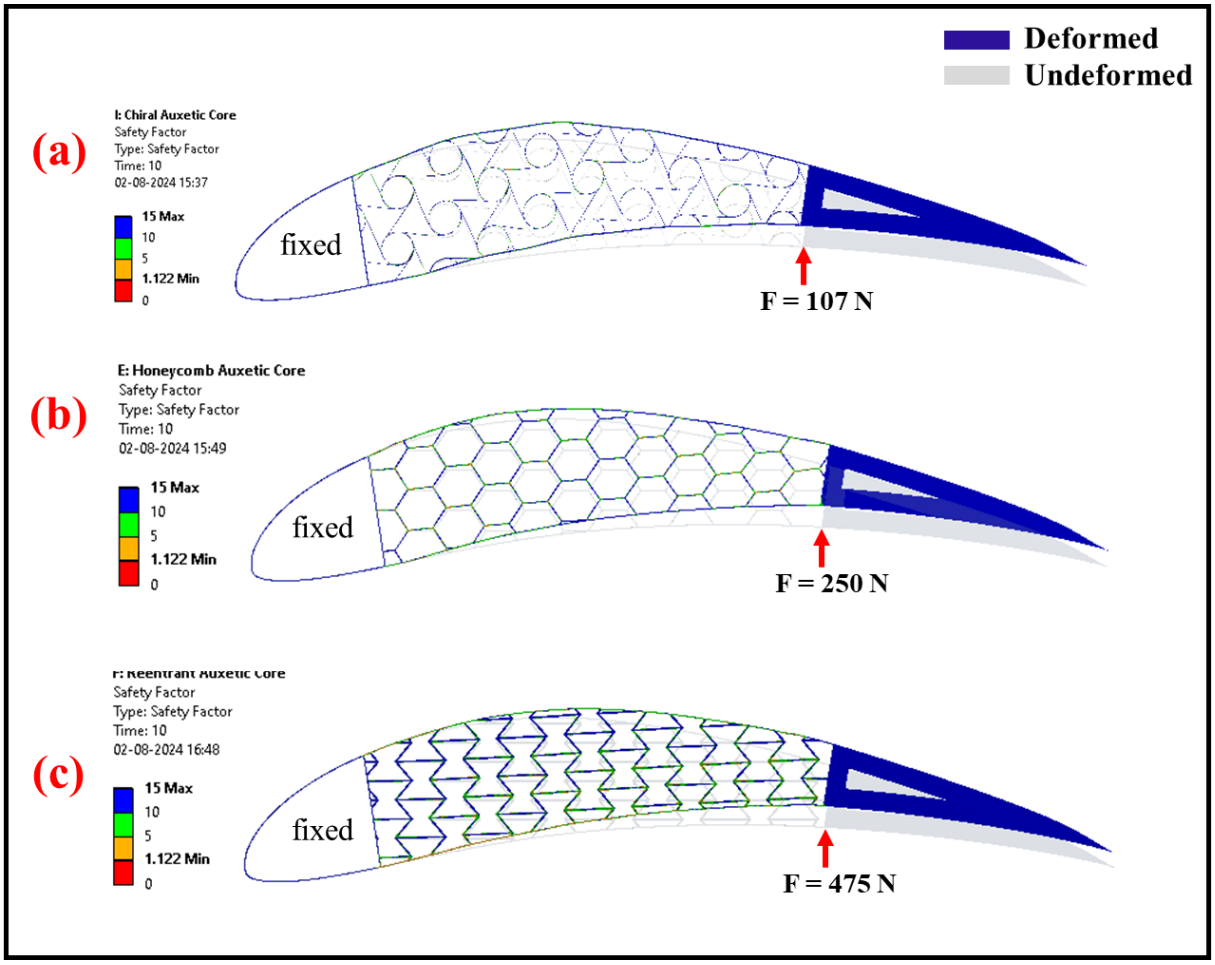

FIGURE 4.5: Factor of Safety (FoS) contours at distinct loads for Eppler 420 airfoil featuring (a) chiral honeycomb core, (b) hexagonal honeycomb core, and (c) reentrant honeycomb core.

From the force magnitudes, it is clear that the energy absorption capacity to withstand loads is highest for reentrant honeycomb configuration, followed by hexagonal honeycomb, and least for the chiral honeycomb structures. The results obtained at the last load step from the structural simulations of chiral, hexagonal, and reentrant auxetic configurations are presented in Figures 4.4, 4.5 and 4.6. Furthermore, the results obtained at each load step from static structural simulations are illustrated through MATLAB graphs plotted and presented in Figure 4.7 and 4.8.

Figure 4.4 explicitly shows three distinct uniaxial loads applied near the ending edge of the auxetic core while the front edges are clamped or restricted. The stress generated in the structure due to resultant loads indicates the equivalent stress generated in all the

cases is identical. Similarly, Figure 4.5 indicates the identical minimum safety factor of the structure determined under the same prior boundary conditions. The reason behind obtaining identical equivalent stress and safety factors for the Eppler 420 airfoil featuring auxetic configurations is to evaluate which configuration efficiently can handle more loads and produce maximum complainant deflection. In this regard, the edge loads applied were incrementally increased by 10 N to ensure that the resulting stress on the structure stayed within the elastic threshold. Upon conducting several simulations, it was concluded that an applied force of 107 N on an airfoil with chiral honeycombs, 250 N with hexagonal honeycombs, and 475 N with reentrant honeycombs yielded the same stress levels and the minimum safety factor.

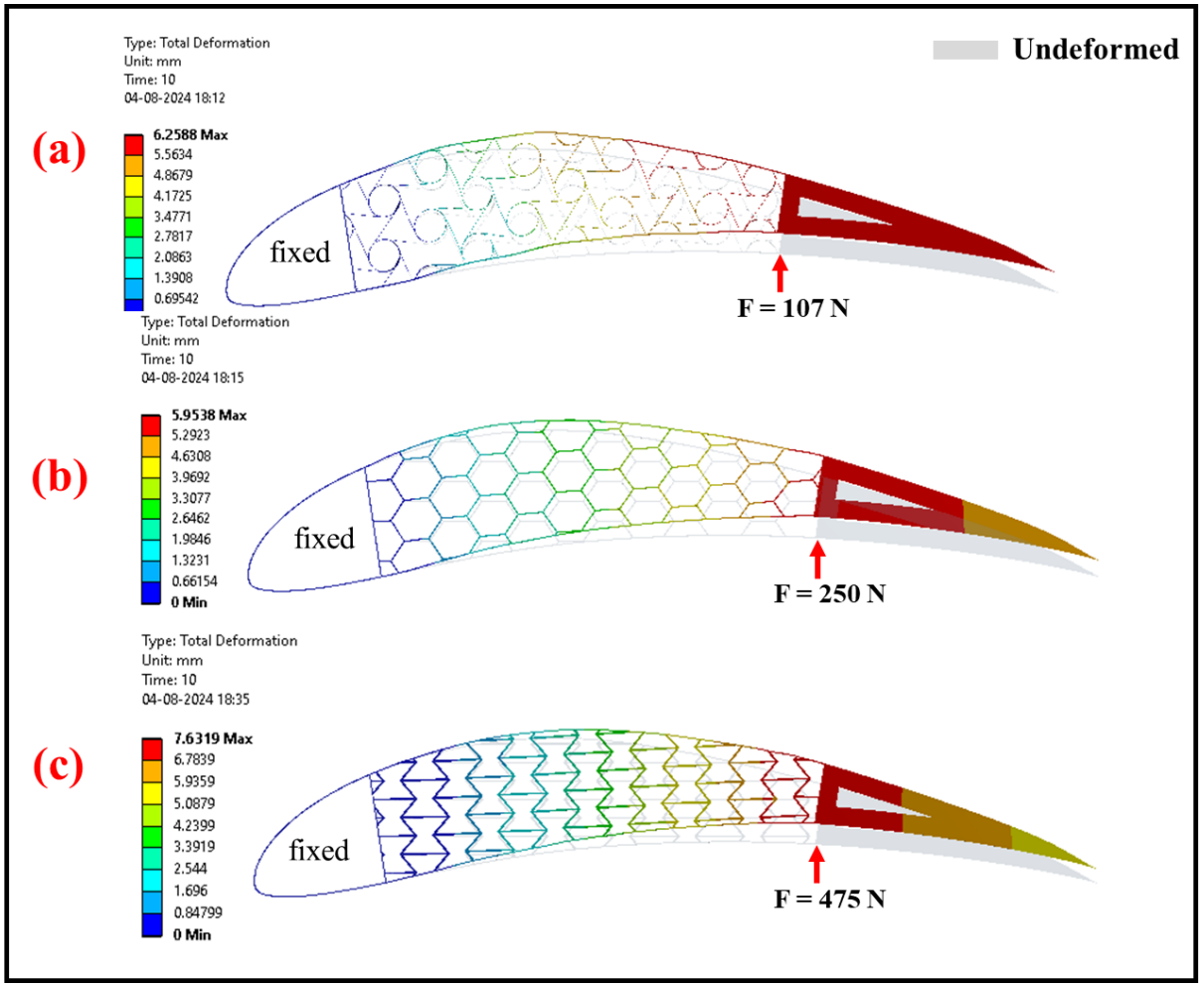

FIGURE 4.6: Total displacement contours at distinct loads for Eppler 420 airfoil featuring (a) chiral honeycomb core, (b) hexagonal honeycomb core, and (c) reentrant honeycomb core.

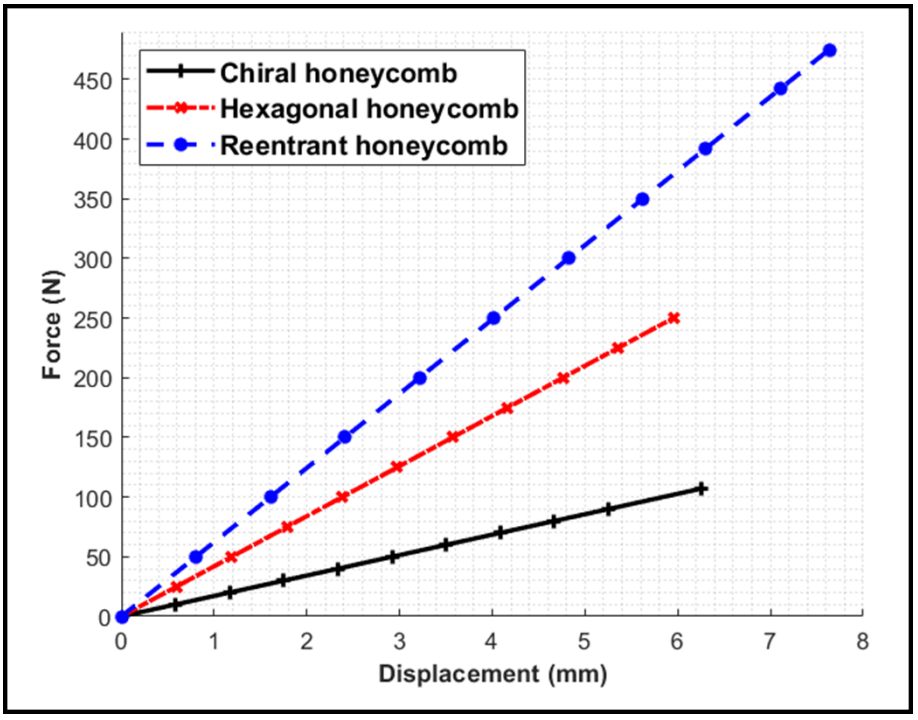

FIGURE 4.7: Comparison of the force versus displacement for Eppler 420 airfoil configuration featuring (a) chiral honeycomb, (b) hexagonal honeycomb, and (c) reentrant honeycomb.

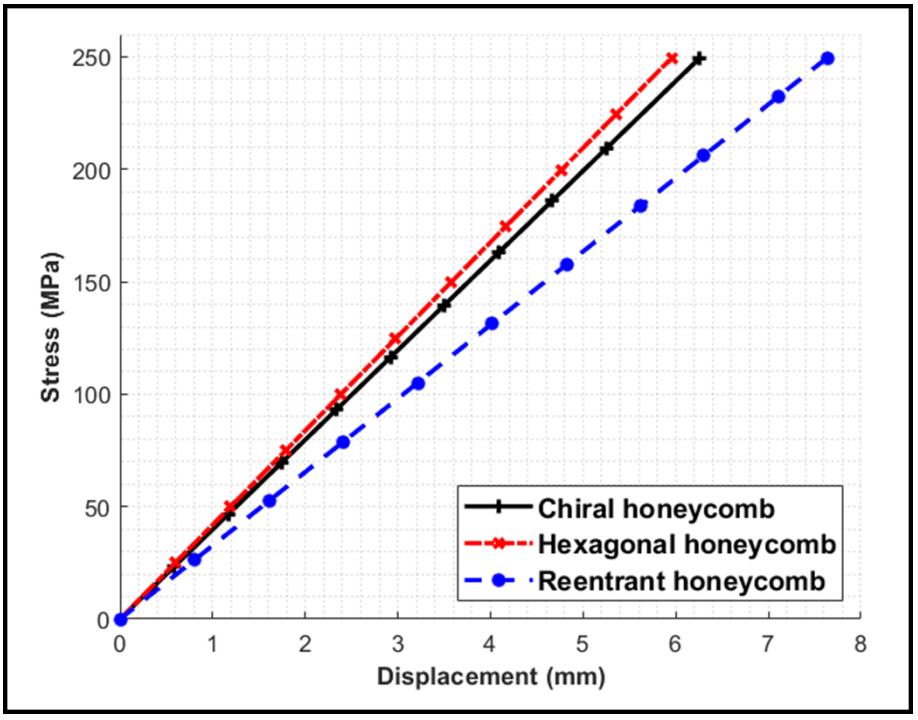

FIGURE 4.8: Comparison of the stress versus displacement for Eppler 420 airfoil configuration featuring (a) chiral honeycomb, (b) hexagonal honeycomb, and (c) reentrant honeycomb.

Figure 4.6 demonstrates the deformation patterns of the Eppler 420 airfoil when paired with various auxetic core structures. It is evident from Figure 4.6 that Eppler 420 airfoils incorporating the reentrant honeycomb design exhibit the highest amount of deflection at the trailing edge, reaching 7.63 mm. This is followed by the airfoils with the chiral honeycomb design, which have a trailing edge displacement of 6.26 mm and the least deflection observed in the hexagonal honeycomb design, with a displacement of 5.95 mm. Furthermore, different loading conditions based on the core design influence these variations in the trailing edge.

Meanwhile, Figures 4.7 and 4.8 compare the trailing edge deflections under step stress and step force loads for the chiral, hexagonal, and reentrant honeycomb configurations. Notably, Figure 4.7 reveals that the reentrant honeycomb configuration, when incorporated into the Eppler 420 airfoil, exhibits a linear response and the greatest deflection at the trailing edge compared to the other designs. Conversely, Figure 4.8 highlights that the reentrant configuration achieves superior trailing edge deflection under the same applied stress. Hence, when assessing the criteria of maximum load bearing capacity and maximum compliant deformation of the trailing edge, the reentrant honeycomb configuration emerges as the most effective auxetic core for the Eppler 420 airfoil.

The comparative analysis led to the conclusion that the reentrant honeycomb configuration outperforms both chiral and hexagonal designs in terms of the morphing efficiency of the Eppler 420 airfoil. Moreover, the auxetic configuration's stiffness and flexibility for wing morphing present a conflicting requirement, which motivated to explore further and develop an optimal reentrant honeycomb configuration. The optimal configuration aims to achieve superior trailing edge deflection compared to the baseline configuration by optimizing the geometrical parameters. Steady-state structural analysis was carried out using ANSYS Mechanical to evaluate the morphing performance of the reentrant honeycomb structure using both baseline and optimal geometric parameters.

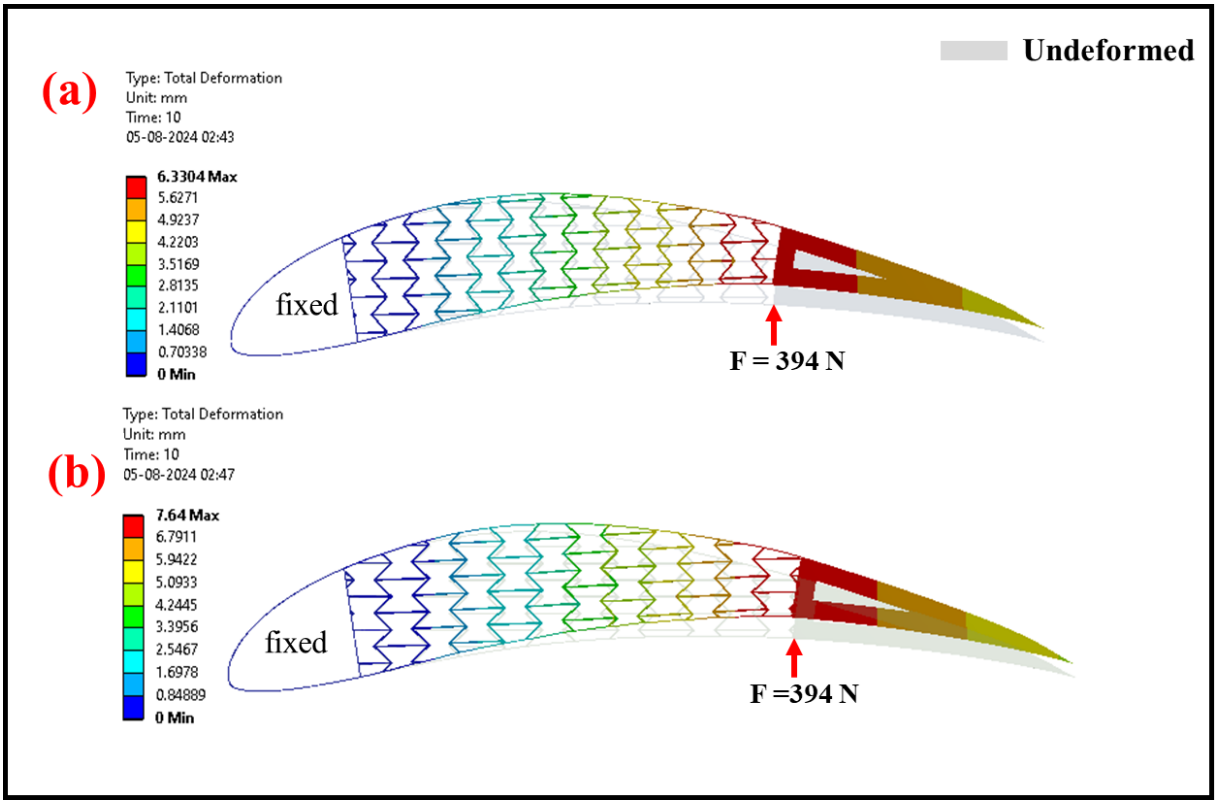

FIGURE 4.9: Total displacement contours at identical loads for Eppler 420 airfoil featuring (a) baseline reentrant honeycomb core and (b) optimal reentrant honeycomb core.

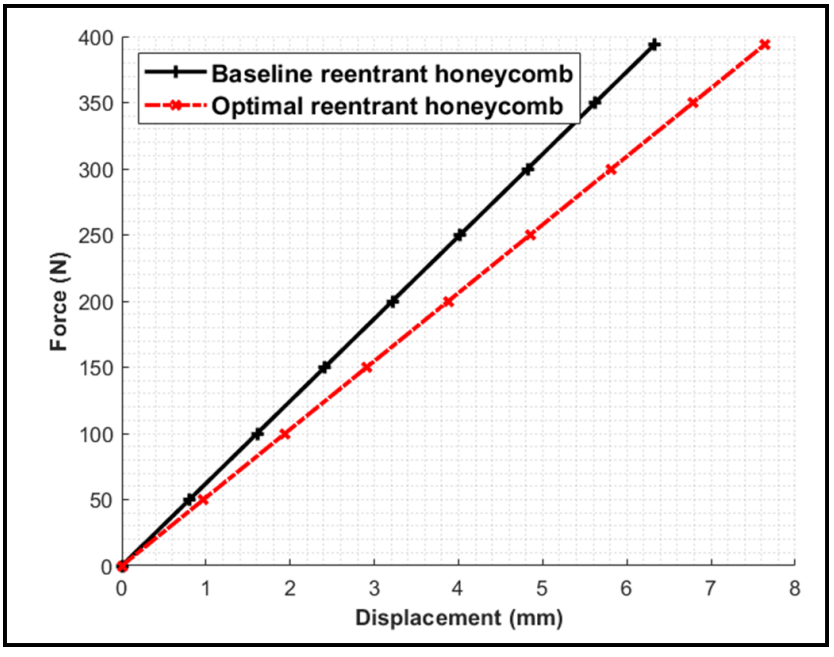

FIGURE 4.10: Comparison of the force versus displacement for Eppler 420 airfoil configuration featuring (a) baseline reentrant and (b) optimal reentrant honeycomb core.

This analysis maintained consistent prior boundary conditions, with the leading edge fixed and a uniaxial load of 394 N applied near the trailing edge of the flexible core, increasing in 50 N increments. Figure 4.9 shows the overall deformation contours of the Eppler 420 airfoil integrating both baseline and optimal reentrant honeycomb configuration at the uniaxial loading of 394 N. Additionally, the trailing edge deflection of the airfoil featuring both cores at incremental loads is illustrated in Figure 4.10.

Figure 4.10 shows a linear trend in the force versus displacement graphs, confirming that the applied load does not exceed the threshold elastic limit. As demonstrated by Figure 4.9, the maximum displacement at the trailing edge is observed to be 7.64 mm with the optimized reentrant honeycomb structure, compared to 6.33 mm for the standard reentrant honeycomb structure. Consequently, integrating the optimized reentrant honeycomb configuration into the core of the Eppler 420 airfoil enhances the morphing efficacy or deflection of the airfoil by roughly 21%.

4.5 CFD Simulation Results

Based on the FEA investigation, it has been concluded that the reentrant honeycomb airfoil configuration demonstrates superior morphing performance compared to chiral and hexagonal honeycomb configurations. As a result, the CFD investigation focuses exclusively on examining the morphing performance of the Eppler 420 airfoil featuring baseline and optimized reentrant honeycomb core for the free stream flow conditions. Since no experimental CFD data on the Eppler 420 airfoil exists in the literature, this research focuses on developing an algorithm to cross-validate the available experimental CFD data of an airfoil with ANSYS Fluent data. In this regard, the devised workflow utilizing Fluent was applied to validate aerodynamic coefficients for the NACA 0012 and NACA 2412 airfoils across different Reynolds numbers. The same workflow was later adopted to assess aerodynamic forces and coefficients of the Eppler 420 airfoil at

different mach numbers for the free stream conditions. The 2D decoupled fluid structural analysis was conducted utilizing weak or 1-way coupling to determine the morphing performance since the laptop cannot handle a strong coupling (2-way coupling), which generally requires three-dimensional analysis.

As discussed in the methodology, a C-type discretized domain achieving y+ of approximately 1 (as suggested in the ANSYS manual) was utilized along with the computational settings outlined in Table 3.3 to calculate and validate the aerodynamic coefficients, including drag coefficient (c_d) and lift coefficient (c_l) when NACA 0012 and NACA 2412 airfoils subjected to angular changes against the direction of oncoming airflow. Figures 4.11 and 4.12 present the validated data obtained from Fluent against the experimental coefficients data for NACA 0012 and NACA 2412 airfoils at Reynolds numbers $6e+06$ and $3.1e+06$, respectively [106, 107].

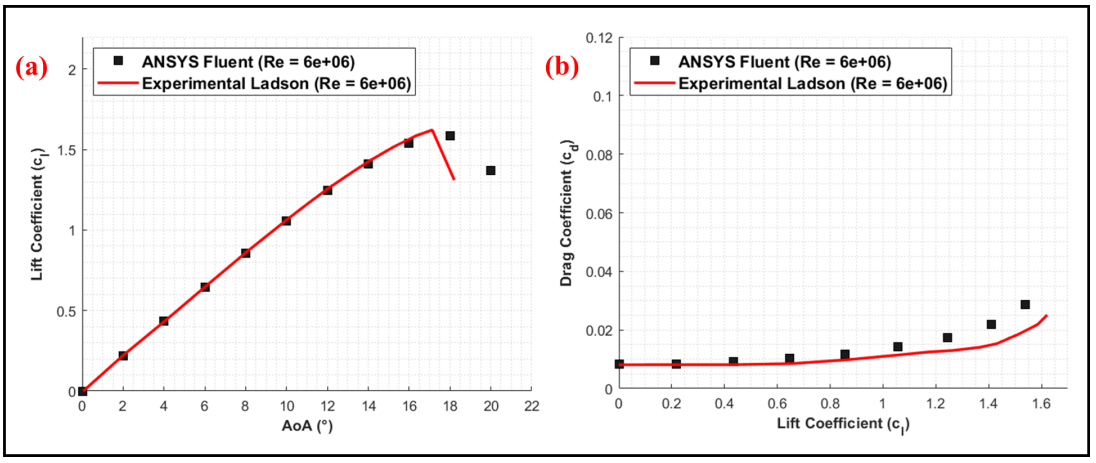

FIGURE 4.11: Comparison between Fluent and experimental results for NACA 0012 airfoil at Reynolds number 6 million, (a) displaying Lift coefficient (c_l) variation with AoA (angle of attack), (b) exhibiting drag coefficients (c_d) against lift coefficients (c_l).

Generally, increasing the AoA increases both c_l and c_d, but only up to the stall angle of the airfoil. Beyond this point, the c_l decreases while c_d increases due to flow separation, which induces greater drag and reduces lift. It is evident from Figures 4.11 and 4.12 that up to the stall angle, the c_l results obtained from simulations accurately match the wind tunnel experimental data.

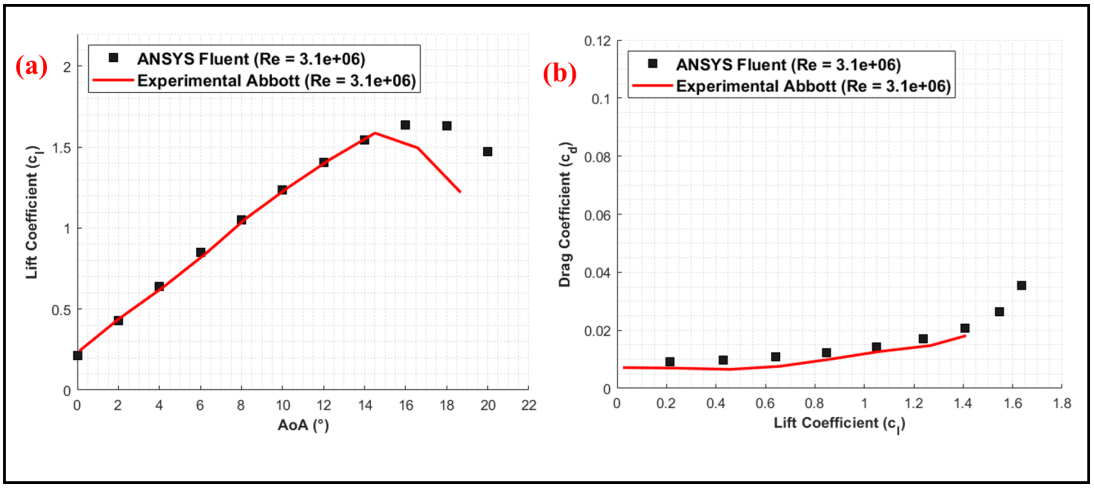

FIGURE 4.12: Comparison between Fluent and experimental results for NACA 2412 airfoil at Reynolds number 3.1 million, (a) displaying Lift coefficient (c_l) variation with AoA (angle of attack), (b) exhibiting drag coefficients (c_d) against lift coefficients (c_l).

However, at higher AoA, particularly beyond the stall limit, the fluent results show a slight deviation in lift coefficients in both cases. A similar pattern is observed while plotting the drag coefficient results against lift coefficients for both airfoils. Nonetheless, the Fluent results obtained from simulations accurately predict the behavior of aerodynamic coefficients similar to that of experimental data. The discrepancies between the Fluent and experimental results could have been minimized by performing a mesh independence study and inputting the precise turbulent intensity and turbulent viscosity ratio parameters specific to the wind tunnel in which the experiments were conducted.

The primary purpose of validating the NACA 0012 and NACA 2412 airfoils aerodynamics was to ensure that the computational Fluent setup is accurate and can be reliably extended to predict the aerodynamic forces and coefficients of any airfoil. The same setup was then used to evaluate the aerodynamics of the Eppler 420 airfoil, setting the oncoming free flow at two Mach numbers, 0.25 and 0.45, respectively. The pressure and velocity contours of the Eppler 420 airfoil at various angles of attack, subjected to a free stream velocity with a Mach number of 0.25, are presented in Figures 4.13 and 4.14. Figures 4.15 and 4.16 illustrate the equivalent contours for a Mach number of 0.45.

Figures 4.13 and 4.15 demonstrate that at lower AoA, such as $\alpha = 0°$ and 4°, the pressure

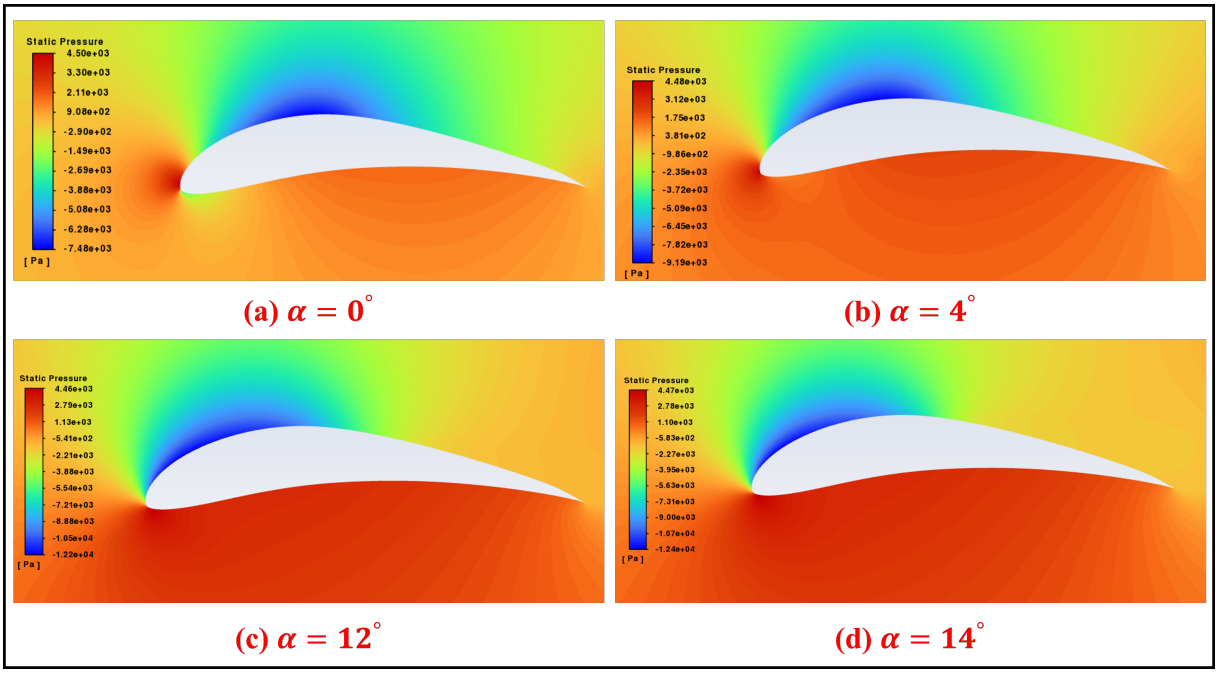

FIGURE 4.13: Pressure contours of the Eppler 420 airfoil subjected to flow velocity of Mach no. 0.25 at varying AoA (a) 0°, (b) 4°, (c) 12° and (d) 14°.

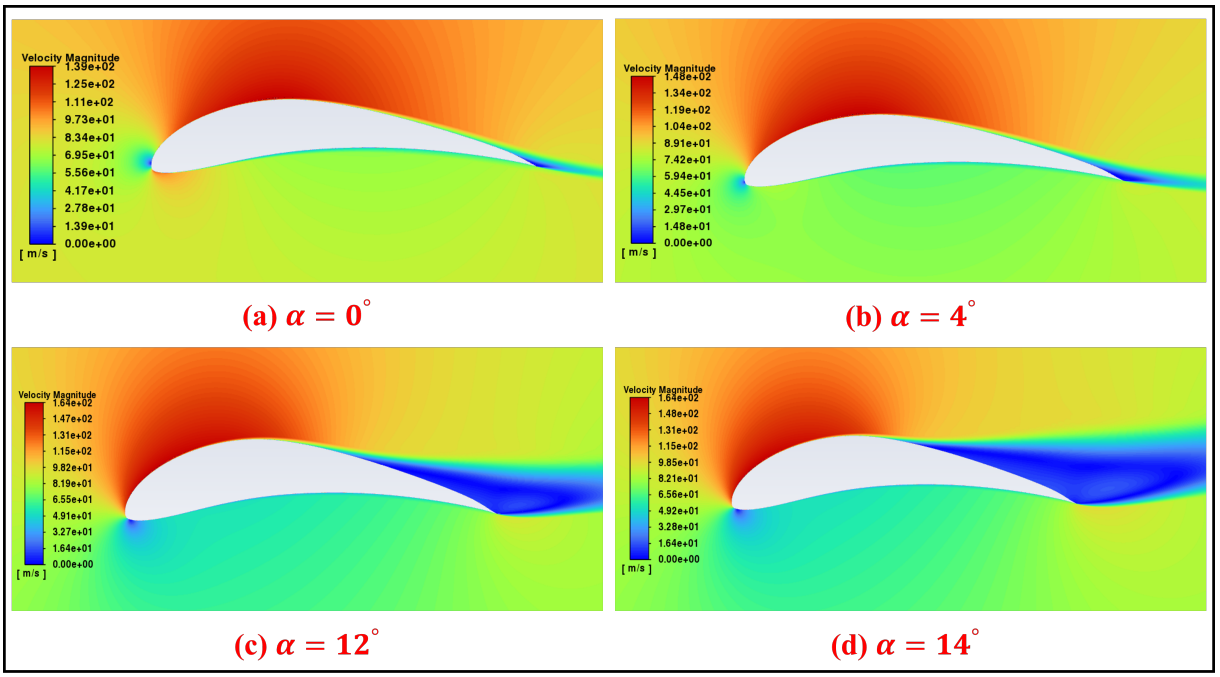

FIGURE 4.14: Velocity contours of the Eppler 420 airfoil subjected to flow velocity of Mach no. 0.25 at varying AoA (a) 0°, (b) 4°, (c) 12° and (d) 14°.

magnitudes are higher on the lower surface of the airfoil and lower on the upper surface. Conversely, as illustrated in Figures 4.14 and 4.16, the velocity magnitudes exhibit the

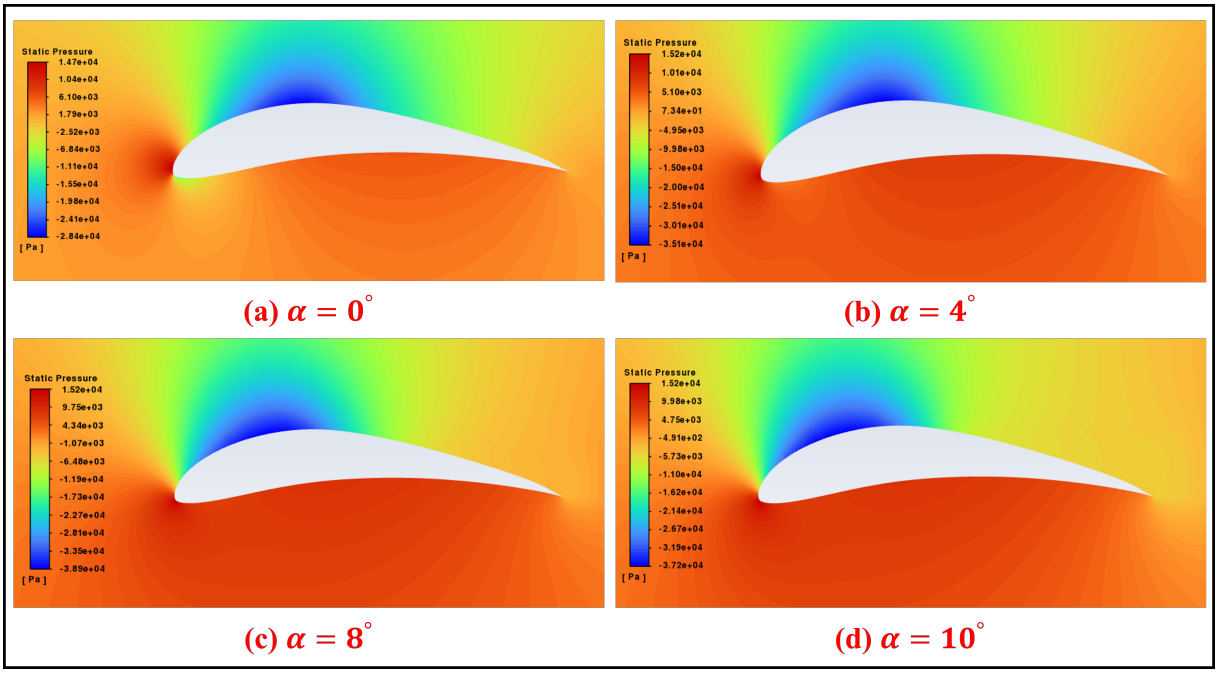

FIGURE 4.15: Pressure contours of the Eppler 420 airfoil subjected to flow velocity of Mach no. 0.45 at varying AoA (a) 0°, (b) 4°, (c) 12° and (d) 14°.

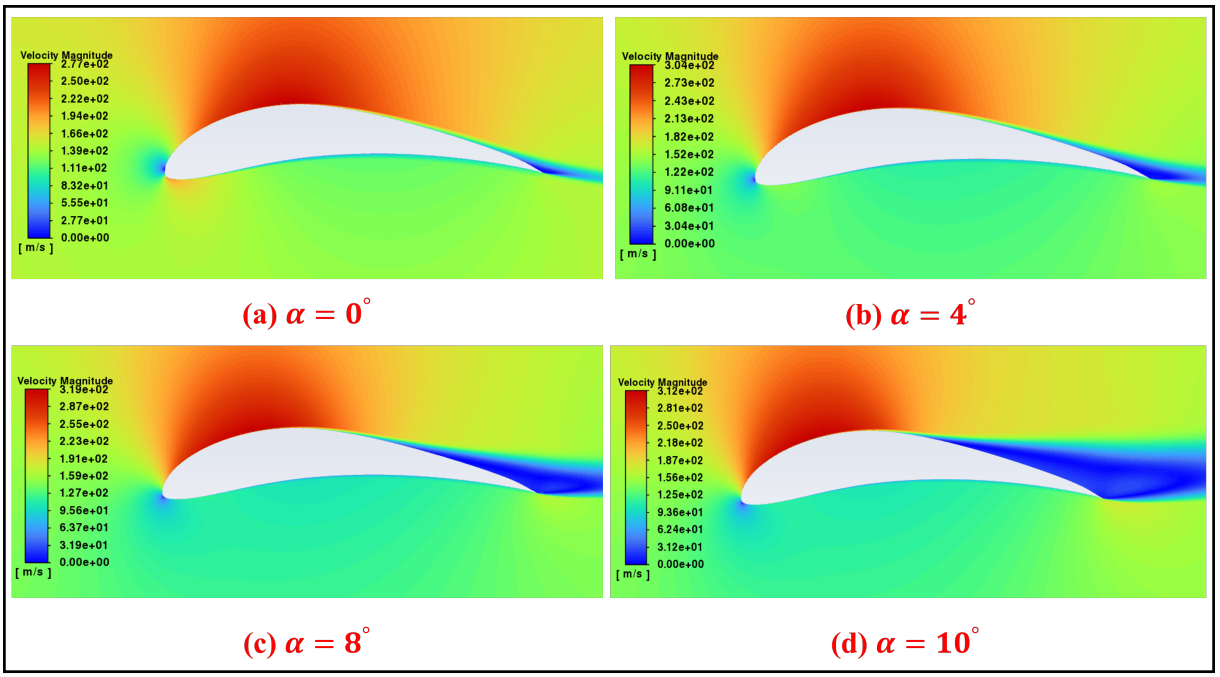

FIGURE 4.16: Velocity contours of the Eppler 420 airfoil subjected to flow velocity of Mach no. 0.45 at varying AoA (a) 0°, (b) 4°, (c) 12° and (d) 14°.

opposite behavior, with higher velocities on the upper surface and lower velocities on the lower surface, obeying Bernoulli's principle. At moderate AoA, such as $\alpha = 6°$ and 8°,

the pressure difference between both surfaces increases with more pronounced pressure distribution across the top surface of the airfoil. Additionally, it is evident from the velocity contours that the velocity magnitudes remain relatively lower at the bottom airfoil surface compared to the upper airfoil surface, forming a vortex in the vicinity of the trailing edge. At higher AoA, such as $\alpha = 10°$, $12°$, and beyond, the pressure difference between top and bottom surfaces increases continuously, and the phenomenon of flow separation starts to occur at the trailing edge and other parts of the airfoil. Beyond the critical angle or stall angle, the flow over the airfoil becomes highly turbulent and irregular, forming a large wake of vortices behind the airfoil.

The aerodynamic lift and drag coefficients for the Eppler 420 airfoil subjected to changes in angles of attack were evaluated by setting the oncoming flow conditions at Mach numbers 0.25 and 0.45, and the calculated results are presented in Figures 4.17 and 4.18.

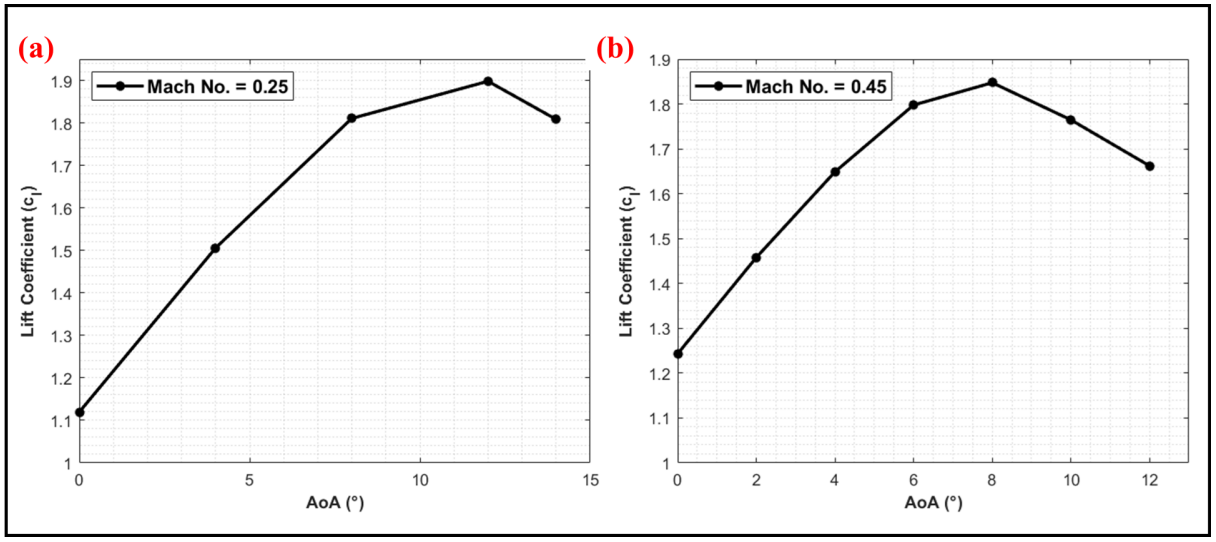

FIGURE 4.17: Fluent results of lift coefficients (c_l) estimated at different AoA with airflow conditions maintained at (a) Mach No. = 0.25 and (b) Mach No. = 0.45.

The plotted data clearly shows that with an increase in the angle of attack, both the lift and drag coefficients increase up to the stall angle. Beyond this critical angle, the lift coefficient starts to decline while the drag coefficient rises. Generally, this trend is expected for an airfoil when computational conditions are analyzed in an incompressible

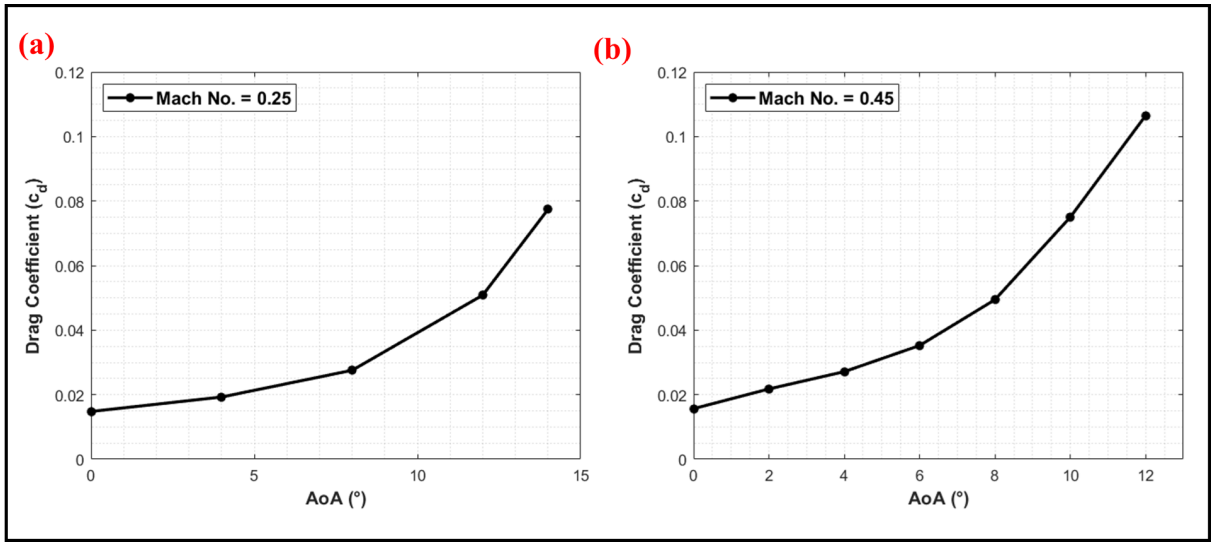

FIGURE 4.18: Fluent results of drag coefficients (c_d) estimated at different angles of attack (AoA) with airflow conditions maintained at (a) Mach No. = 0.25 and (b) Mach No. = 0.45

fluid regime. Moreover, increasing the Reynolds number while keeping the same Mach number for the airflow freestream shows that the fluid adheres to the airfoil surface for greater duration, increasing the lift and delaying stall angles.

However, the analysis performed for this research is carried out to understand the effect of flow behavior across Eppler 420 airfoil with the same material properties at Mach numbers in the incompressible and compressible regimes. The Fluent data predicted that for an oncoming airflow at Mach 0.25, the stall angle for the airfoil was found to be 12°. In contrast, for an oncoming airflow at Mach 0.45, Fluent predicted a stall angle of 8°. It becomes clear that the stall angle reduces at a higher Mach number because, at lower Mach numbers less than 0.3, compressibility effects are very minimal, and fluid adheres to the airfoil surface. In contrast, compressibility effects become significant at Mach numbers 0.3 and above. For highly-chambered airfoils like Eppler 420, the airfoil becomes more sensitive to changes in pressure distribution. This leads to the possibility that some parts of the flow over the airfoil may become transonic, leading to early flow separation and a lower stall angle even in the subsonic airflow regimes.

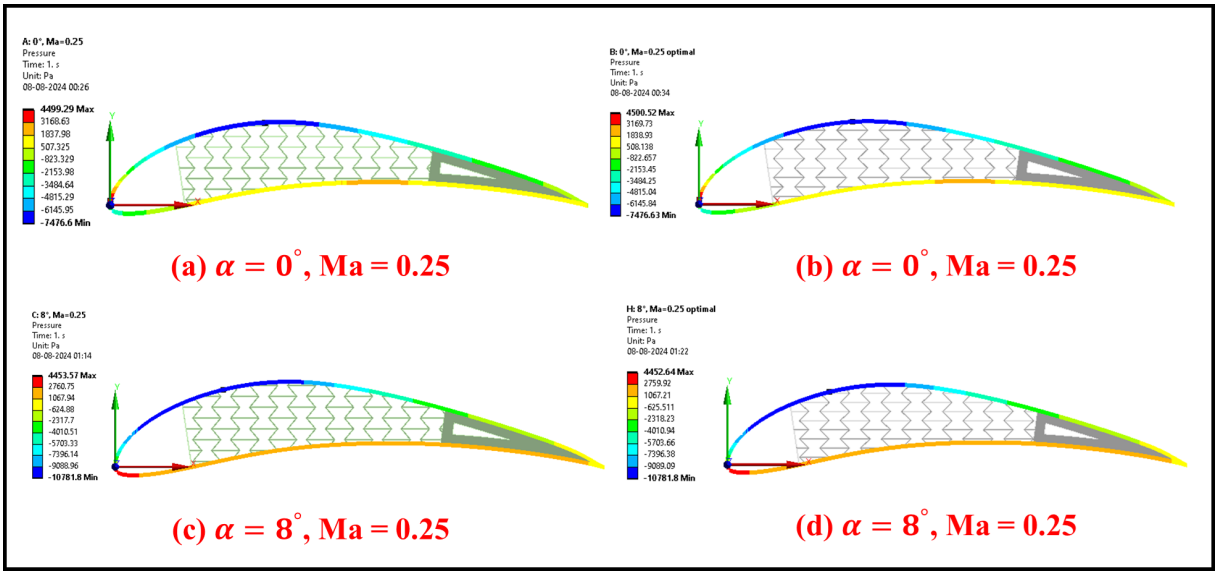

FIGURE 4.19: Imported pressure loading for free stream Mach no. 0.25 on the airfoil mid surface with (a) a standard core at 0° AoA, (b) an optimized core at 0° AoA, (c) a standard core at 8° AoA, and (d) an optimized core at 8° AoA.

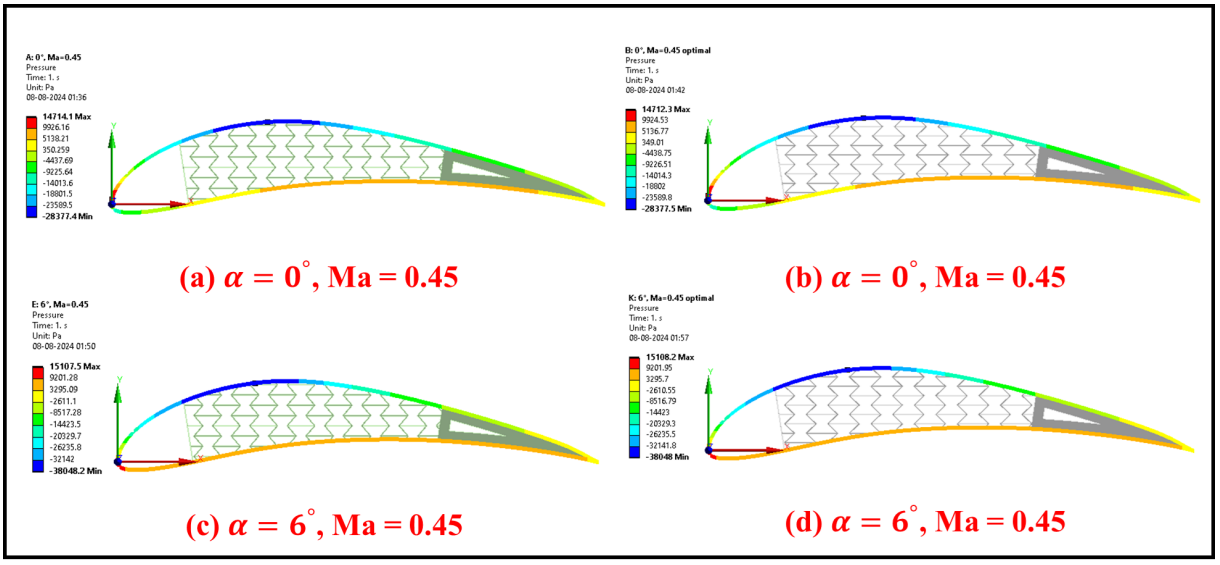

FIGURE 4.20: Imported pressure loading for free stream Mach no. 0.45 on the airfoil mid surface with (a) a standard core at 0° AoA, (b) an optimized core at 0° AoA, (c) a standard core at 6° AoA, and (d) an optimized core at 6° AoA.

To evaluate the impact of pressure distribution caused by fluid flow at various angles of attack on the Eppler airfoil, incorporating both baseline and optimized reentrant honeycomb cores, nodal pressure data from the top and bottom edges of the airfoil were collected and applied onto the mid-surface of the Eppler 420 airfoil incorporating a reentrant honeycomb cores. Using the Ansys Static Structural Module, the pressure

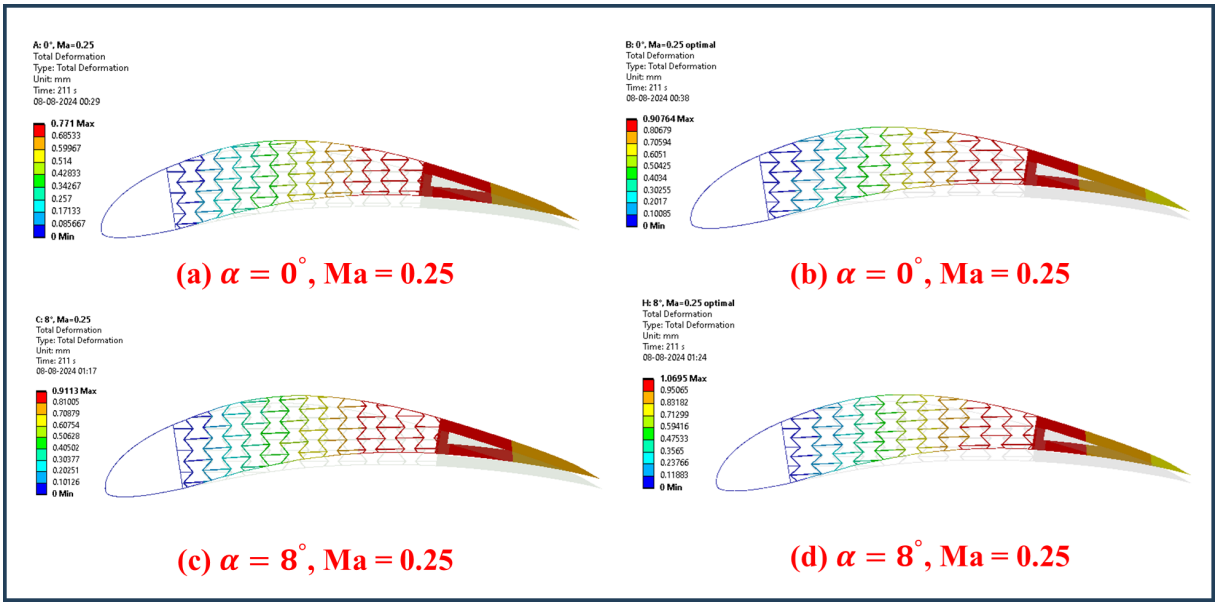

FIGURE 4.21: Resulted airfoil deformations due to pressure loading for free stream Mach no. 0.25 with (a) a standard core at 0° AoA, (b) an optimized core at 0° AoA, (c) a standard core at 8° AoA, and (d) an optimized core at 8° AoA.

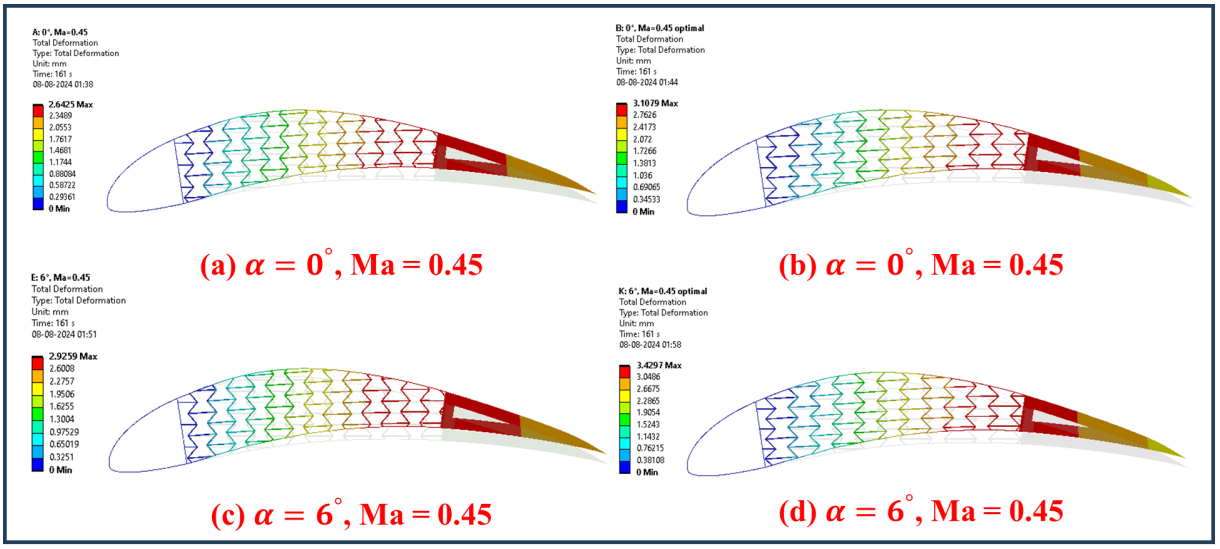

FIGURE 4.22: Resulted airfoil deformations due to pressure loading for free stream Mach no. 0.45 with (a) a standard core at 0° AoA, (b) an optimized core at 0° AoA, (c) a standard core at 6° AoA, and (d) an optimized core at 6° AoA.

distribution derived from CFD analysis was imposed on the airfoil's top and bottom edges of the generated mid-surface, as depicted in Figures 4.19 and 4.20. Figures 4.21 and 4.22 demonstrate the total deformation results of the Eppler 420 airfoil incorporating a reentrant honeycomb with baseline and optimal geometric parameters.

It is observed from the total deformation results that increasing the incoming flow Mach number and increasing the angle of attack increases the trailing edge deflection of the airfoil and, so, the morphing performance. However, the maximum trailing edge deflection for the Eppler 420 airfoil when the airflow conditions were set to 0.25 Mach number was achieved when the airfoil was subjected to an angular rotation of 8°. In contrast, for 0.45 Mach number, the maximum trailing edge deflection was achieved when the airfoil was subjected to an angular rotation of 6°. The morphing performance with respect to attaining better trailing edge deflection increases with the increase of the angle of attack. The primary reason is that the pressure difference between the upper and bottom surfaces increases. The maximum deflection was observed at the angle of attack where the airfoil's pressure distribution produced a high lift-to-drag ratio. A summary of the aerodynamic forces and coefficients obtained for simulated Eppler airfoil at varying angles of attack when airflow conditions are set to 0.25 and 0.45 Mach numbers are detailed in Tables 4.2 and 4.3.

TABLE 4.2: Summarised numerical results for Eppler 420 airfoil at Mach number 0.25.

AoA (°)	**Lift coefficient, c_l**	**Drag coefficient, c_d**	**Lift (N)**	**Drag (N)**	**Airfoil deflection with standard reentrant core (mm)**	**Airfoil deflection with optimal reentrant core (mm)**
0	1.119	0.0148	3535.573	46.700	0.771	0.907
4	1.505	0.0193	4754.062	60.853	0.865	1.0176
8	1.811	0.0275	5717.127	87.004	0.911	1.0695
12	1.897	0.0508	5993.134	160.544	0.842	0.98574
14	1.808	0.0774	5709.825	244.475	0.770	0.903

TABLE 4.3: Summarised numerical results for Eppler 420 airfoil at Mach number 0.45.

AoA (°)	**Lift coefficient, c_l**	**Drag coefficient, c_d**	**Lift (N)**	**Drag (N)**	**Airfoil deflection with standard reentrant core (mm)**	**Airfoil deflection with optimal reentrant core (mm)**
0	1.243	0.0156	12213.431	153.862	2.643	3.108
2	1.458	0.0217	14328.233	214.032	2.852	3.296
4	1.648	0.0271	16204.075	266.660	2.909	3.415
6	1.798	0.0352	17668.673	346.313	2.926	3.429
8	1.847	0.0494	18157.589	485.916	2.787	3.264
10	1.765	0.0750	17343.889	737.289	2.531	2.966
12	1.662	0.1065	16335.702	1046.638	2.347	2.755

Chapter 5

Conclusion and Future Work

5.1 Conclusion

This research work aims to design a singular monolithic structure design capable of replacing the complex assembly of a traditional aircraft wing, including ailerons, flaps, slats, and spoilers. Therefore, this structure must have the capability to endure substantial aerodynamic loads across different flight regimes while minimizing drag losses and overall weight, thereby reducing emissions and manufacturing costs.

The literature review revealed that cellular auxetic metamaterials or meta-structures are identified for their superior mechanical properties and multifunctional capabilities, making them ideal for advanced structural component designs. This research explored the impacts of different cellular structures on the trailing edge deflections and their added advantage in integration for wing morphing applications. In this regard, the 3D Eppler 420 airfoil model featuring three different auxetic core configurations, chiral honeycomb, hexagonal honeycomb, and reentrant honeycomb configurations, was analyzed to determine the one with the best morphing performance. Several investigations were conducted in this regard, and their final findings are detailed below.

- A parametric study was performed utilizing formulated mathematical expressions elucidated by Hedayati et al. to understand the effect of geometric parameters of reentrant honeycomb configurations on the mechanical elastic properties such as elastic moduli and Poisson's ratio. The analysis revealed that the angle between the struts of the structure majorly induces auxetic behavior.

- To design a novel optimal reentrant honeycomb configuration with maximum elastic moduli and negative Poisson's ratio, a multi-objective optimization maximizing two objective functions (E_x and ν_{xy}) was performed using the gamultiobj toolbox in MATLAB. The optimized parameters resulted in an approximate 54.65% increase in Poisson's ratio and a 37.5% augmentation in the relative elastic modulus, as determined analytically.

- FEA analysis conducted on the Eppler 420 airfoil model with reentrant honeycomb configurations demonstrated the highest morphing performance, followed by the chiral honeycomb configuration, with the hexagonal honeycomb configuration exhibiting the lowest performance. Furthermore, for the same aerostatic load, employing an optimized reentrant honeycomb core with optimized geometrical parameters led to a significant augmentation of 21% compared to using a standard reentrant core.

- Decoupled fluid structural analysis on the Eppler 420 airfoil, incorporating both standard and optimized reentrant honeycomb configurations with a weak coupling approach, indicated that the airfoil exhibits maximum morphing at an 8° angle of attack with an airflow of Mach 0.25. At a Mach number of 0.45, the optimal performance is achieved at a 6° angle of attack. Additionally, decoupled fluid structural analysis revealed that the integration of optimized reentrant honeycomb configuration further improves morphing or deflection of the trailing edge by 17.3% compared to a standard reentrant honeycomb core.

5.2 Future Works

In the future, the methodology developed for the current research work can be modified and refined to develop different cellular auxetic configurations for their utilization in wing morphing applications. One can particularly focus on completing the tasks in the near future, which are detailed as follows.

- Current research utilizes 2-dimensional chiral honeycomb, hexagonal honeycomb, and reentrant honeycomb configurations to assess the morphing performance. Future research can be extended to include the exploration of other 2D auxetic configurations and the investigation of 3D topologies of these auxetic structures.

- Current CFD investigation primarily involves 2D studies to understand the fluid behavior over the Eppler 420 airfoil edges. The CFD analysis can be extended to simulate a 3D full-scale wing model incorporating cellular structures utilizing a strong form of coupling (2-way coupling) FSI approach to predict real-life wing morphing performance precisely.

References

[1] J. C. Gomez and E. Garcia, "Morphing unmanned aerial vehicles," *Smart Materials and Structures*, vol. 20, no. 10, p. 103001, 2011.

[2] T. A. Weisshaar, "Morphing aircraft systems: historical perspectives and future challenges," *Journal of aircraft*, vol. 50, no. 2, pp. 337–353, 2013.

[3] P. Henningsson and A. Hedenström, "Aerodynamics of gliding flight in common swifts," *Journal of experimental biology*, vol. 214, no. 3, pp. 382–393, 2011.

[4] B. Ponitz, A. Schmitz, D. Fischer, H. Bleckmann, and C. Brücker, "Diving-flight aerodynamics of a peregrine falcon (falco peregrinus)," *PLoS One*, vol. 9, no. 2, p. e86506, 2014.

[5] J. A. Cheney, J. P. Stevenson, N. E. Durston, M. Maeda, J. Song, D. A. Megson-Smith, S. P. Windsor, J. R. Usherwood, and R. J. Bomphrey, "Raptor wing morphing with flight speed," *Journal of The Royal Society Interface*, vol. 18, no. 180, p. 20210349, 2021.

[6] J. Zhu, J. Yang, W. Zhang, X. Gu, and H. Zhou, "Design and applications of morphing aircraft and their structures," *Frontiers of Mechanical Engineering*, vol. 18, no. 3, p. 34, 2023.

[7] L. Wiggins, M. Stubbs, C. Johnston, H. Robertshaw, C. Reinholtz, and D. Inman, "A design and analysis of a morphing hyper-elliptic cambered span (hecs) wing," in *45th AIAA/ASME/ASCE/AHS/ASC Structures, Structural Dynamics & Materials Conference*, p. 1885, 2004.

[8] R. M. Ajaj, C. S. Beaverstock, and M. I. Friswell, "Morphing aircraft: The need for a new design philosophy," *Aerospace Science and Technology*, vol. 49, pp. 154–166, 2016.

[9] A. K. Jha and J. N. Kudva, "Morphing aircraft concepts, classifications, and challenges," in *Smart structures and materials 2004: industrial and commercial applications of smart structures technologies*, vol. 5388, pp. 213–224, SPIE, 2004.

[10] C. Thill, J. Etches, I. Bond, K. Potter, and P. Weaver, "Morphing skins," *The aeronautical journal*, vol. 112, no. 1129, pp. 117–139, 2008.

[11] A.-M. R. McGowan, D. E. Cox, B. S. Lazos, M. R. Waszak, D. L. Raney, E. J. Siochi, and S. P. Pao, "Biologically inspired technologies in nasa's morphing project," in *Smart Structures and Materials 2003: Electroactive Polymer Actuators and Devices (EAPAD)*, vol. 5051, pp. 1–13, SPIE, 2003.

[12] A. Spadoni and M. Ruzzene, "Numerical and experimental analysis of the static compliance of chiral truss-core airfoils," *Journal of Mechanics of Materials and Structures*, vol. 2, no. 5, pp. 965–981, 2007.

[13] P. Budarapu, S. S. YB, and R. Natarajan, "Design concepts of an aircraft wing: composite and morphing airfoil with auxetic structures," *Frontiers of Structural and Civil Engineering*, vol. 10, pp. 394–408, 2016.

[14] A. Rodriguez, "Morphing aircraft technology survey," in *45th AIAA aerospace sciences meeting and exhibit*, p. 1258, 2007.

[15] E. Krause, "The reissner canard: The first all-metal airplane 100 years ago," *Progress in Aerospace Sciences*, vol. 54, pp. 59–64, 2012.

[16] S. Barbarino, O. Bilgen, R. M. Ajaj, M. I. Friswell, and D. J. Inman, "A review of morphing aircraft," *Journal of intelligent material systems and structures*, vol. 22, no. 9, pp. 823–877, 2011.

[17] J. Valasek, K. Kirkpatrick, and A. Lampton, "Morphing unmanned air vehicle intelligent shape and flight control," *Morphing Aerospace Vehicles and Structures*, pp. 55–86, 2012.

[18] E. Stanewsky, "Adaptive wing and flow control technology," *Progress in Aerospace Sciences*, vol. 37, no. 7, pp. 583–667, 2001.

[19] R. M. Ajaj, M. S. Parancheerivilakkathil, M. Amoozgar, M. I. Friswell, and W. J. Cantwell, "Recent developments in the aeroelasticity of morphing aircraft," *Progress in Aerospace Sciences*, vol. 120, p. 100682, 2021.

[20] G. Sachs, B. Grüter, and H. Hong, "Wing sweep effects on the maximum speed performance in high-speed dynamic soaring," in *AIAA Scitech 2021 Forum*, p. 0641, 2021.

[21] N. TSUSHIMA and M. TAMAYAMA, "Recent researches on morphing aircraft technologies in japan and other countries," *Mechanical Engineering Reviews*, vol. 6, no. 2, pp. 19–00197, 2019.

[22] W. A. Chapkin, P. Walgren, G. J. Frank, D. R. Seifert, D. J. Hartl, and J. W. Baur, "Design and optimization of high-strain, cylindrical composite skins for morphing fuselages," *Materials & Design*, vol. 187, p. 108395, 2020.

[23] J. Abras and R. Narducci, "Analysis of cfd modeling techniques over the mv-22 tiltrotor," in *American Helicopter Society 66th Annual Forum*, pp. 11–13, 2010.

[24] S. Ameduri and A. Concilio, "Morphing wings review: Aims, challenges, and current open issues of a technology," *Proceedings of the Institution of Mechanical Engineers, Part C: Journal of Mechanical Engineering Science*, vol. 237, no. 18, pp. 4112–4130, 2023.

[25] R. C. Smith, *Smart material systems: model development*. SIAM, 2005.

[26] A. E. Washburn, "Nasa micro-aero-adaptive control," in *Smart Structures and Materials 2001: Industrial and Commercial Applications of Smart Structures Technologies*, vol. 4332, pp. 326–344, SPIE, 2001.

[27] J. Sun, Q. Guan, Y. Liu, and J. Leng, "Morphing aircraft based on smart materials and structures: A state-of-the-art review," *Journal of Intelligent material systems and structures*, vol. 27, no. 17, pp. 2289–2312, 2016.

[28] A. Abbas, J. De Vicente, and E. Valero, "Aerodynamic technologies to improve aircraft performance," *Aerospace science and technology*, vol. 28, no. 1, pp. 100–132, 2013.

[29] S. Anders, W. Sellers III, and A. Washburn, "Active flow control activities at nasa langley," in *2nd AIAA Flow Control Conference*, p. 2623, 2004.

[30] J. A. Seidel, A. K. Sehra, and R. O. Colantonio, "Nasa aeropropulsion research: looking forward," in *Fifteenth International Symposium on Airbreathing Engines*, no. E-12922, 2001.

[31] R. Rajamani, *Electric Flight Technology: The Unfolding of a New Future*. SAE International, 2018.

[32] D. Chandler, "Mit and nasa engineers demonstrate a new kind of airplane wing," 2019.

[33] R. Siddall and M. Kovac, "Bioinspired aerial robots," in *Encyclopedia of Robotics*, pp. 1–12, Springer Berlin, 2020.

[34] R. Ajaj, M. Friswell, E. Saavedra Flores, O. Little, and A. Isikveren, "Span morphing: a conceptual design study," in *53rd AIAA/ASME/ASCE/AHS/ASC structures, structural dynamics and materials conference 20th AIAA/ASME/AHS adaptive structures conference 14th AIAA*, p. 1510, 2012.

[35] J. H. Fincham, C. S. Beaverstock, A. B. Coles, L. L. Parsons, M. I. Friswell, and R. M. Ajaj, "Aerodynamic forces on morphing wings during span extension," *Advanced aero concepts, design, and operations*, 2014.

[36] A. Tarabi, S. Ghasemloo, and M. Mani, "Experimental investigation of a variable-span morphing wing model for an unmanned aerial vehicle," *Journal of the Brazilian Society of Mechanical Sciences and Engineering*, vol. 38, pp. 1833–1841, 2016.

[37] R. Huang and Z. Qiu, "Transient aeroelastic responses and flutter analysis of a variable-span wing during the morphing process," *Chinese Journal of aeronautics*, vol. 26, no. 6, pp. 1430–1438, 2013.

[38] F. Moens, "Augmented aircraft performance with the use of morphing technology for a turboprop regional aircraft wing," *Biomimetics*, vol. 4, no. 3, p. 64, 2019.

[39] "Wikimedia commons. grumman f-14 tomcat sdasm. 2014, available at wikimedia website."

[40] Y. Lei, D. Zhang, Y. Zhang, and G. Su, "Numerical study on aerodynamic characteristics of variable-sweep morphing aircraft at transonic speeds," in *IOP Conference Series: Materials Science and Engineering*, vol. 751, p. 012001, IOP Publishing, 2020.

[41] "Wikimedia commons. tornado variable sweep wing manching. 2006, available at wikimedia website."

[42] "Wikimedia commons. aircraft engine mig-23 sweep wing mechanism. 2006, available at wikimedia website."

[43] T. Ma, Y. Fan, N. Chang, J. Yang, Z. Yu, and X. Zhou, "Design of a variable-sweep wing structure with flexible shear skin," *Aerospace Systems*, vol. 5, no. 1, pp. 37–46, 2022.

[44] "Wikimedia commons. north american xb-70a valkyrie in flight (cropped). 2006, available at wikimedia website."

[45] "Air force research laboratory. flight tests conclude for shape changing aircraft flap. 2015, available at wpafb website."

[46] "Flexsys. aviation partners-flexsys goes public with morphing wing technology demonstrator. 2017, available at flexsys website."

[47] T. Majid and B. W. Jo, "Status and challenges on design and implementation of camber morphing mechanisms," *International Journal of Aerospace Engineering*, vol. 2021, no. 1, p. 6399937, 2021.

[48] S. La, W. Y. Joe, M. Akbar, and B. Alsaidi, "Surveys on skin design for morphing wing aircraft: status and challenges," in *2018 AIAA aerospace sciences meeting*, p. 0315, 2018.

[49] A. Zhao, H. Zou, H. Jin, and D. Wen, "Structural design and verification of an innovative whole adaptive variable camber wing," *Aerospace Science and Technology*, vol. 89, pp. 11–18, 2019.

[50] T. Yokozeki, A. Sugiura, and Y. Hirano, "Development of variable camber morphing airfoil using corrugated structure," *Journal of Aircraft*, vol. 51, no. 3, pp. 1023–1029, 2014.

[51] H. Takahashi, T. Yokozeki, and Y. Hirano, "Development of variable camber wing with morphing leading and trailing sections using corrugated structures," *Journal of Intelligent Material Systems and Structures*, vol. 27, no. 20, pp. 2827–2836, 2016.

[52] M. Maki, "Experimental study of a morphing wing configuration with multi-slotted variable-camber mechanism," in *AIAA Atmospheric Flight Mechanics Conference*, p. 3849, 2016.

[53] Y. Kuya, R. Ito, M. Maki, and K. Sawada, "Numerical study of flowfield around a multislotted high-lift wing," *Journal of Aircraft*, vol. 58, no. 2, pp. 383–389, 2021.

[54] U. Fasel, D. Keidel, L. Baumann, G. Cavolina, M. Eichenhofer, and P. Ermanni, "Composite additive manufacturing of morphing aerospace structures," *Manufacturing Letters*, vol. 23, pp. 85–88, 2020.

[55] Y. Zhang, W. Ge, Z. Zhang, X. Mo, and Y. Zhang, "Design of compliant mechanism-based variable camber morphing wing with nonlinear large deformation," *International Journal of Advanced Robotic Systems*, vol. 16, no. 6, p. 1729881419886740, 2019.

[56] R. Wu, C. Soutis, S. Zhong, and A. Filippone, "A morphing aerofoil with highly controllable aerodynamic performance," *The Aeronautical Journal*, vol. 121, no. 1235, pp. 54–72, 2017.

[57] G. Molinari, A. F. Arrieta, and P. Ermanni, "Aero-structural optimization of three-dimensional adaptive wings with embedded smart actuators," *AIAA journal*, vol. 52, no. 9, pp. 1940–1951, 2014.

[58] B. K. S. Woods and M. I. Friswell, "Preliminary investigation of a fishbone active camber concept," in *Smart materials, adaptive structures and intelligent systems*, vol. 45103, pp. 555–563, American Society of Mechanical Engineers, 2012.

[59] B. K. Woods, O. Bilgen, and M. I. Friswell, "Wind tunnel testing of the fish bone active camber morphing concept," *Journal of Intelligent Material Systems and Structures*, vol. 25, no. 7, pp. 772–785, 2014.

[60] W. Tao and M. C. Leu, "Design of lattice structure for additive manufacturing," in *2016 International Symposium on Flexible Automation (ISFA)*, pp. 325–332, IEEE, 2016.

[61] Q. Li, X. Zhi, and F. Fan, "Quasi-static compressive behaviour of 3d-printed origami-inspired cellular structure: experimental, numerical and theoretical studies," *Virtual and Physical Prototyping*, vol. 17, no. 1, pp. 69–91, 2022.

[62] T. Li, J. Sun, J. Leng, and Y. Liu, "Quasi-static compressive behavior and energy absorption of novel cellular structures with varying cross-section dimension," *Composite Structures*, vol. 306, p. 116582, 2023.

[63] P. Köhnen, C. Haase, J. Bültmann, S. Ziegler, J. H. Schleifenbaum, and W. Bleck, "Mechanical properties and deformation behavior of additively manufactured lattice structures of stainless steel," *Materials & Design*, vol. 145, pp. 205–217, 2018.

[64] R. D. Vocke III, C. S. Kothera, B. K. Woods, and N. M. Wereley, "Development and testing of a span-extending morphing wing," *Journal of Intelligent Material Systems and Structures*, vol. 22, no. 9, pp. 879–890, 2011.

[65] J. Martin, J.-J. Heyder-Bruckner, C. Remillat, F. Scarpa, K. Potter, and M. Ruzzene, "The hexachiral prismatic wingbox concept," *physica status solidi (b)*, vol. 245, no. 3, pp. 570–577, 2008.

[66] D. Bornengo, F. Scarpa, and C. Remillat, "Evaluation of hexagonal chiral structure for morphing airfoil concept," *Proceedings of the Institution of Mechanical Engineers, Part G: Journal of Aerospace Engineering*, vol. 219, no. 3, pp. 185–192, 2005.

[67] P. Bettini, A. Airoldi, G. Sala, L. Di Landro, M. Ruzzene, and A. Spadoni, "Composite chiral structures for morphing airfoils: Numerical analyses and development of a manufacturing process," *Composites Part B: Engineering*, vol. 41, no. 2, pp. 133–147, 2010.

[68] "Whitwam r. nasa, mit design hollow morphing airplane wing. 2019, available at extremetech website."

[69] Z. G. Nicolaou and A. E. Motter, "Mechanical metamaterials with negative compressibility transitions," *Nature materials*, vol. 11, no. 7, pp. 608–613, 2012.

[70] J. N. Grima and R. Caruana-Gauci, "Materials that push back," *Nature materials*, vol. 11, no. 7, pp. 565–566, 2012.

[71] A. A. Zadpoor, "Mechanical meta-materials," *Materials Horizons*, vol. 3, no. 5, pp. 371–381, 2016.

[72] W. Cai, U. K. Chettiar, A. V. Kildishev, and V. M. Shalaev, "Optical cloaking with metamaterials," *Nature photonics*, vol. 1, no. 4, pp. 224–227, 2007.

[73] V. M. Shalaev, "Optical negative-index metamaterials," *Nature photonics*, vol. 1, no. 1, pp. 41–48, 2007.

[74] K. E. Evans, M. Nkansah, I. Hutchinson, and S. Rogers, "Molecular network design," *Nature*, vol. 353, no. 6340, pp. 124–124, 1991.

[75] S. Burns, "Negative poisson's ratio materials," *Science*, vol. 238, no. 4826, pp. 551–551, 1987.

[76] J. L. Williams and J. L. Lewis, "Anisotropic model of cancellous bone.," *American Society of Mechanical Engineers, Applied Mechanics Division, AMD*, vol. 32, pp. 181–182, 1979.

[77] X. Hou and V. V. Silberschmidt, "Metamaterials with negative poisson's ratio: A review of mechanical properties and deformation mechanisms," *Mechanics of Advanced Materials: Analysis of Properties and Performance*, pp. 155–179, 2015.

[78] M. Sanami, N. Ravirala, K. Alderson, and A. Alderson, "Auxetic materials for sports applications," *Procedia Engineering*, vol. 72, pp. 453–458, 2014.

[79] I. Masters and K. Evans, "Models for the elastic deformation of honeycombs," *Composite structures*, vol. 35, no. 4, pp. 403–422, 1996.

[80] H. M. Kolken and A. Zadpoor, "Auxetic mechanical metamaterials," *RSC advances*, vol. 7, no. 9, pp. 5111–5129, 2017.

[81] F. Scarpa and P. Tomlin, "On the transverse shear modulus of negative poisson's ratio honeycomb structures," *Fatigue & Fracture of Engineering Materials & Structures*, vol. 23, no. 8, pp. 717–720, 2000.

[82] U. D. Larsen, O. Signund, and S. Bouwsta, "Design and fabrication of compliant micromechanisms and structures with negative poisson's ratio," *Journal of microelectromechanical systems*, vol. 6, no. 2, pp. 99–106, 1997.

[83] N. Gaspar, X. Ren, C. W. Smith, J. Grima, and K. E. Evans, "Novel honeycombs with auxetic behaviour," *Acta Materialia*, vol. 53, no. 8, pp. 2439–2445, 2005.

[84] J. N. Grima, R. Gatt, A. Alderson, and K. Evans, "On the potential of connected stars as auxetic systems," *Molecular Simulation*, vol. 31, no. 13, pp. 925–935, 2005.

[85] R. Lakes, "Deformation mechanisms in negative poisson's ratio materials: structural aspects," *Journal of materials science*, vol. 26, pp. 2287–2292, 1991.

[86] J. N. Grima, R. Gatt, and P.-S. Farrugia, "On the properties of auxetic meta-tetrachiral structures," *physica status solidi (b)*, vol. 245, no. 3, pp. 511–520, 2008.

[87] A. Alderson, K. L. Alderson, D. Attard, K. E. Evans, R. Gatt, J. N. Grima, W. Miller, N. Ravirala, C. Smith, and K. Zied, "Elastic constants of 3-, 4-and 6-connected chiral and anti-chiral honeycombs subject to uniaxial in-plane loading," *Composites Science and Technology*, vol. 70, no. 7, pp. 1042–1048, 2010.

[88] D. Prall and R. Lakes, "Properties of a chiral honeycomb with a poisson's ratio of—1," *International Journal of Mechanical Sciences*, vol. 39, no. 3, pp. 305–314, 1997.

[89] C. S. Ha, M. E. Plesha, and R. S. Lakes, "Chiral three-dimensional lattices with tunable poisson's ratio," *Smart Materials and Structures*, vol. 25, no. 5, p. 054005, 2016.

[90] J. N. Grima and K. E. Evans, "Auxetic behavior from rotating squares," *Journal of materials science letters*, vol. 19, pp. 1563–1565, 2000.

[91] D. Attard and J. N. Grima, "Auxetic behaviour from rotating rhombi," *physica status solidi (b)*, vol. 245, no. 11, pp. 2395–2404, 2008.

[92] J. N. Grima, A. Alderson, and K. E. Evans, "An alternative explanation for the negative poisson's ratios in auxetic foams," *Journal of the Physical Society of Japan*, vol. 74, no. 4, pp. 1341–1342, 2005.

[93] R. Hedayati, A. Yousefi, M. L. Dezaki, and M. Bodaghi, "Analytical relationships for 2d re-entrant auxetic metamaterials: An application to 3d printing flexible implants," *journal of the mechanical behavior of biomedical materials*, vol. 143, p. 105938, 2023.

[94] A. Konak, D. W. Coit, and A. E. Smith, "Multi-objective optimization using genetic algorithms: A tutorial," *Reliability engineering & system safety*, vol. 91, no. 9, pp. 992–1007, 2006.

[95] J. H. Holland, *Adaptation in natural and artificial systems: an introductory analysis with applications to biology, control, and artificial intelligence*. MIT press, 1992.

[96] C. M. Fonseca and P. J. Fleming, "Multiobjective genetic algorithms," in *IEE colloquium on genetic algorithms for control systems engineering*, pp. 6–1, Iet, 1993.

[97] K. Deb, "Nonlinear goal programming using multi-objective genetic algorithms," *Journal of the Operational Research Society*, vol. 52, no. 3, pp. 291–302, 2001.

[98] "gamultiobj algorithm. performing a multiobjective optimization using the genetic algorithm. available at matlab website."

[99] C. ANSYS, "Meshing user's guide release 13," *ANSYS Inc*, 2010.

[100] K. Almohammadi, "Assessment of several modeling strategies on the prediction of lift-drag coefficients of a naca0012 airfoil at a moderate reynold number," *Alexandria Engineering Journal*, vol. 61, no. 3, pp. 2242–2249, 2022.

[101] S. Gupta, R. K. Tyagi, P. Pratiksha, and A. Gairola, "A review on evolution of airfoils and their characteristics in last three centuries. part-1: Evolution of flights and shapes of wing sections before 1930 and naca series," in *AIP Conference Proceedings*, vol. 2597, AIP Publishing, 2022.

[102] H. Heo, J. Ju, and D.-M. Kim, "Compliant cellular structures: application to a passive morphing airfoil," *Composite Structures*, vol. 106, pp. 560–569, 2013.

[103] A. Subramanian, S. A. Yogesh, H. Sivanandan, A. Giri, M. Vasudevan, V. Mugundhan, and R. K. Velamati, "Effect of airfoil and solidity on performance of small scale vertical axis wind turbine using three dimensional cfd model," *Energy*, vol. 133, pp. 179–190, 2017.

[104] J. Winslow, H. Otsuka, B. Govindarajan, and I. Chopra, "Basic understanding of airfoil characteristics at low reynolds numbers (10 4–10 5)," *Journal of aircraft*, vol. 55, no. 3, pp. 1050–1061, 2018.

[105] A. Whan, H. Singh, N. Malik, R. Mallick, A. Sharma, and M. Sahni, "Optimizing the design of auxetic core airfoil for wing morphing applications," vol. 4, 2024.

[106] C. L. Ladson, *Effects of independent variation of Mach and Reynolds numbers on the low-speed aerodynamic characteristics of the NACA 0012 airfoil section*, vol. 4074. National Aeronautics and Space Administration, Scientific and Technical . . . , 1988.

[107] H. Seetharam, E. Rodgers, and W. Wentz Jr, "Experimental studies of flow separation of the naca 2412 airfoil at low speeds," tech. rep., 1997.

20240816_v02_Aman_MTech_THESIS.pdf

ORIGINALITY REPORT

16%	11%	13%	5%
SIMILARITY INDEX	INTERNET SOURCES	PUBLICATIONS	STUDENT PAPERS

PRIMARY SOURCES

1	Reza Hedayati, Armin Yousefi, Mohammadreza Lalegani Dezaki, Mahdi Bodaghi. "Analytical relationships for 2D Re-entrant auxetic metamaterials: An application to 3D printing flexible implants", Journal of the Mechanical Behavior of Biomedical Materials, 2023 Publication	2%
2	journal.hep.com.cn Internet Source	1%
3	citeseerx.ist.psu.edu Internet Source	1%
4	pubs.rsc.org Internet Source	1%
5	www.ncbi.nlm.nih.gov Internet Source	1%